Acute Preclinical Evaluation of Compliance-Matched and TGFβ2 Eluting Vascular Grafts

by

Kenneth John Furdella Jr.

Biomedical Engineering, Drexel University, Philadelphia PA, 2012

Master of Science in Biomedical Engineering, University of Arizona, Tucson AZ, 2016

Submitted to the Graduate Faculty of

the Swanson School of Engineering in partial fulfillment

of the requirements for the degree of

Doctor of Philosophy

University of Pittsburgh

2021

UNIVERSITY OF PITTSBURGH

SWANSON SCHOOL OF ENGINEERING

This dissertation was presented

by

Kenneth John Furdella Jr.

It was defended on

July 22, 2021

and approved by

Jonathan Vande Geest, Ph.D., Professor, Department of Bioengineering

Kang Kim, Ph.D., Associate Professor, Department of Bioengineering, and Department of Medicine

Russell S. Witte, Ph.D., Professor, Department of Medical Imaging, University of Arizona

Morgan Fedorchak, Ph.D., Assistant Professor, Department of Ophthalmology, Bioengineering and Clinical & Translational Sciences

Dissertation Director: Jonathan Vande Geest, Ph.D., Professor, Department of Bioengineering

Acute Preclinical Evaluation of Compliance-Matched and TGFβ2 Eluting Vascular Grafts

Kenneth John Furdella Jr., PhD

University of Pittsburgh, 2021

In the western world, coronary heart disease (CHD) from atherosclerosis kills over 365,000 people annually and is the leading cause of death worldwide. Atherosclerosis can also act on the blood vessels in the arms or legs causing peripheral arterial disease(PAD), which affects over 6.5 million people over the age of 40. A standard intervention for CAD/PAD is a bypass surgery using a vascular graft. Commercially available synthetic grafts are a distant second option for CAD treatment due to their limited efficacy in smaller diameter vessels. Synthetic grafts or tissue engineered grafts (TEVG) often fail due to a compliance mismatch between the native vascular and the graft and an inability to remodel in vivo into a functional vessel. The ideal bypass graft for treatment of CAD/PAD would be an off-the-shelf graft that remains patent, compliance-matched, and remodels into a fully functional vessel. The goal of this dissertation is to use a rat interpositional aortic implantation model to evaluate the effect of compliance-matching on cellular infiltration in vivo, use transforming growth factor beta 2 (TGFβ2) to promote a desired in-vivo remodeling response, and develop a new method to evaluate graft drug delivery and degradation.

The compliance of the TEVGs was tuned to either match or be twice as stiff as rat aorta. These constructs were subsequently implanted into the abdominal aorta of Sprague Dawley rats and evaluated in-vivo using ultrasound and at a one-month explantation timepoint. The compliance-matched TEVGs remained compliant over the time course of the study and showed desired signs of remodeling with increased ratios of CD163/CD68 macrophages, increased smooth muscle cells, and increased collagen deposition when compared to the hypocompliant grafts ($p<0.05$). TGFβ2 was then added to the TEVG to evaluate cellular infilatration over an acute 5-day period. The low concentrations of TGFβ2 in the compliance-matched TEVG were found to increase SMC proliferation while the higher concentrations decreased the SMC population and promoted collagen deposition ($p<0.05$). The hypocom-

pliant construct had no differences between all groups and concentrations. Finally, a new noninvasive method was developed to evaluate TEVG graft design, degradation, and drug delivery using photoacoustic imaging.

Table of Contents

Preface . . . xvii

1.0 Introduction . . . 1

1.1 Overview . . . 1

1.2 Coronary Heart Disease and Peripheral Arterial Disease Statistics . . . 1

1.3 Surgical Treatment of CHD and PAD . . . 2

1.4 Anatomy of the Blood Vessel . . . 3

1.5 Atherosclerosis . . . 4

1.6 Tissue Engineered Vascular Graft and Design . . . 5

1.7 Preclinical Analysis of TEVGs . . . 6

1.8 Hypotheses and Specific Aims . . . 7

2.0 In-vivo assessment of a tissue engineered vascular graft computationally optimized for target vessel compliance . . . 9

2.1 Introduction . . . 9

2.2 Methods . . . 9

2.2.1 **TEVG Characterization and Fabrication** . . . 9

2.2.1.1 **Preparation of Rat Aorta** . . . 9

2.2.1.2 **Compliance Testing** . . . 10

2.2.1.3 **Compliance Matching and Computational Optimization Routine** . . . 10

2.2.1.4 **Electrospinning Materials and fabrication** . . . 11

2.2.1.5 **Suture Retention** . . . 13

2.2.1.6 **Burst Pressure** . . . 13

2.2.1.7 **Cytotoxicity** . . . 14

2.2.2 **Rat Implantation** . . . 14

2.2.2.1 **Rat Interpositional Abdominal Aorta Surgery** . . . 14

2.2.3 **Graft Measurements and Quantification** . . . 15

2.2.3.1 **In-vivo Ultrasound** . . . 15
2.2.3.2 **Preparation, Immunohistochemistry, and Fluorescent Imaging** . . . 17
2.2.3.3 **Multiphoton Imaging** . . . 18
2.2.3.4 **Image Processing** . . . 19
2.2.3.5 **Statistical Analysis** . . . 20
2.3 Results . . . 20
2.3.1 **Construct Characterization** . . . 20
2.3.2 **Rat in-vivo Ultrasound** . . . 22
2.3.3 **Multiphoton Imaging** . . . 22
2.3.4 **Quantitative Immunohistochemistry** . . . 23
2.4 Discussion . . . 28
2.5 Conclusion . . . 34
3.0 Modulating TGFβ2 Elution Alters the Acute Remodeling of a Compliance-Matched Tissue Engineered Vascular Graft . . . 36
3.1 Introduction . . . 36
3.2 Methods . . . 37
3.2.1 **Optimization Routine for TEVG Formulation** . . . 37
3.2.2 **Graft Material and Fabrication** . . . 39
3.2.3 **Rat Aortic Implantation** . . . 40
3.2.4 **Measurements and Quantification of Outcomes** . . . 41
3.2.4.1 **In Vivo Ultrasound** . . . 41
3.2.4.2 **Immunohistochemistry and Fluorescent Imaging** . . . 42
3.2.4.3 **Multiphoton Imaging** . . . 43
3.2.4.4 **Image Processing** . . . 44
3.3 Results . . . 44

3.3.1 **Construct Characterization** . . . 44
3.3.2 **Ultrasound** . . . 45
3.3.3 **Multiphoton Imaging** . . . 45
3.3.4 **Immunohistochemistry** . . . 48
3.4 Discussion . . . 51
3.5 Conclusion . . . 55
4.0 Tracking Delivery of a Drug Surrogate in the Porcine Coronary Artery Using Photoacoustic Imaging and Spectroscopy . . . 57
4.1 Introduction . . . 57
4.2 Methods . . . 59
4.2.1 **PAIS Setup and Dye** . . . 59
4.2.2 **Image Processing and PA Signal Decomposition (Unmixing)** 61
4.2.3 **Photoacoustic Imaging Experiments** . . . 61
4.3 Results . . . 63
4.3.1 **Validation and Calibration in Excised Myocardium** . . . 63
4.4 Discussion . . . 65
4.5 Conclusion . . . 70
5.0 Conclusion . . . 71
5.1 Overview . . . 71
5.2 Summary of Results . . . 71
5.2.1 Chapter 2: In-vivo assessment of a tissue engineered vascular graft computationally optimized for target vessel compliance . . . 71
5.2.2 Chapter 3: Modulating TGFβ2 Elution Alters the Acute Remodeling of a Compliance-Matched Tissue Engineered Vascular Graft . . . 72
5.2.3 Chapter 4: Tracking delivery of a drug surrogate in the porcine coronary artery using photoacoustic imaging and spectroscopy . . . 73
5.3 Future Work and Limitations . . . 73
5.4 Conclusions . . . 77
6.0 Appendix . . . 79
Bibliography . . . 82

List of Tables

1 Polymeric formulations, layer thickness, and crosslinking concentrations for the $HYPO_{pcl}$, CM_{gel}, and $HYPO_{gen}$ graft formulations. 13

2 Polymeric formulations, layer thickness, crosslinking concentrations, and TGFβ2 concentration (ng/mg). 41

List of Figures

1 A) Atheroslcerotic vessel - showing plaque that is narrowing the lumen of the vessel; B) balloon angioplasty - inflated balloon, which is compressing the plaque on the vessel wall; C) stent deployment in an atherosclerotic vessel that has restored blood flow; D) coronary artery bypass - vascular graft from the aorta to coronary to bypass the narrowed artery in the heart. 3

2 Anatomy of the blood vessel showing the three layers (inside to outside): tunica intima, tunica media, and tunica adventitia. The tunica intima is composed of a single layer of endothelial cells and acts as a barrier to prevent thrombosis. The tunica media is composed of elastin and SMCs, which are responsible for dilation and constriction of the vessel. The tunica adventitia is composed of connective tissue that helps to anchor the vessel in place. 4

3 A) Overview of the optimization routine that demonstrates how mechanical testing of the vascular grafts lead to a computational optimizational scheme to calculate graft formulation; B) Electrospinning setup, demonstrating the two-nozzle setup of the device; C) Implantation of a CM_{gel} TEVG in the abdominal rat aorta. 16

4 Pre-implantation images, compliance, thickness, inner radius, suture retention, burst pressure, and cytotoxicity of the $HYPO_{pcl}$, CM_{gel}, and $HYPO_{gen}$ TEVGs. The scale bar is 50 μm. The compliance of the CM_{gel} constructs matched rat aorta, while the HYPO grafts were over twice as stiff. $HYPO_{gen}$ TEVGs were found to be slightly thicker than the CM_{gel}. All constructs had a similar inner radius, around 550 μm. The suture retention and burst pressure of the $HYPO_{pcl}$ was greatly increased compared to the CM_{gel}, and $HYPO_{gen}$ TEVGs. The CM_{gel} and $HYPO_{gen}$ TEVGs had a slight reduction of cell number at 48 hours and no differences at 96, while the $HYPO_{pcl}$ had no differences at both time points. $*$, $p<0.05$ 21

5 In vivo ultrasound measurements of compliance, average inner diameter, and velocity in the $HYPO_{pcl}$, CM_{gel}, and $HYPO_{gen}$ TEVGs. The CM_{gel} constructs matched native rat aorta compliance over time, while the HYPO grafts were generally less compliant. The average diameter stayed relatively consist over the one-month time point except for the $HYPO_{gen}$ TEVGs that had two graft dilations. The average velocity for the CM_{gel} and $HYPO_{gen}$ TEVGs tended to decrease over the implantation period and the $HYPO_{pcl}$ TEVGs stayed consistently below native rat aorta velocity. $*$, $p<0.05$, $**$, $p<0.01$ 23

6 Top) Cross-sectional multiphoton implant images of $HYPO_{pcl}$, CM_{gel}, and $HYPO_{gen}$ TEVGs; Green, blue, and red represent the implant, cell nuclei, collagen, respectively; The scale bar is 50 μm. Bottom) Differences in the amount of construct remaining, cells inside our TEVGs, and luminal thickness. The $HYPO_{pcl}$ TEVGs had less construct degradation and cellular infiltration than compared to CM_{gel} and $HYPO_{gen}$ TEVGs. The average luminal thickness was found to be similar between all implants. $*$, $p<0.05$ 24

7 Representative middle cross-sectional immunofluorescence images. Green, blue, and red represent the implant, cell nuclei, and marker, respectively. The scale bar is 50 μm. 25

8 Representative proximal longitudinal immunofluorescence images (top). Immunohistochemistry quantification of signal in the lumen, graft, and abluminal regions for SMCs, Ki67 cells, pan macrophages (CD68), M2 (CD163), M1 (CD86), M2/Total (CD163/CD68), collagen, and elastin (bottom). SMC markers, MHC and Calponin, were relatively increased in the CM_{gel} compared to the HYPO groups. The Ki67 signal was elevated in the graft region of the CM_{gel} to the $HYPO_{gel}$. The collagen produced was increased in the lumen region of the $HYPO_{pcl}$ compared to CM_{gel} group. $*$ = $p<0.05$; $**$ = $p<0.01$; Y axis = Pixels of Interest/Total Pixels; Scale bar is 100 μm 26

9 Representative middle cross-sectional immunofluorescence images (top). Immunohistochemistry quantification of signal in the lumen, graft, and abluminal regions for SMCs, Ki67 cells, pan macrophages (CD68), M2 (CD163), M1 (CD86), M2/Total (CD163/68), collagen, and elastin (bottom). The αSMC in the CM_{gel} and $HYPO_{gen}$ TEVGs was increased compared to the $HYPO_{pcl}$ TEVGs. The Ki67, CD163, and elastin signal was elevated in the $HYPO_{gen}$ compared to $HYPO_{pcl}$ TEVG. There was a luminal increased in CD163 and elastin signal in the CM_{gel} to $HYPO_{pcl}$ groups. CD68 signal was only evaluated in the abluminal region of the $HYPO_{gen}$ compared to CM_{gel}. The total and abluminal CD86 signal in the CM_{gel} was increased compared to the $HYPO_{gen}$ and the $HYPO_{pcl}$ in the lumen was increased compared to the $HYPO_{gen}$. The ratio of CD163/CD68 was increased in the CM_{gel} compared to the HYPO group. The collagen content in the lumen and graft of the CM_{gel} were higher than the $HYPO_{pcl}$. $*$ = p<0.05; $**$ = p<0.01; Y axis = Pixels of Interest/Total Pixels; Scale bar is 100 μm 27

10 Overview of TGFβ2 study. 1. Compliance-matched and hypocompliant constructs were fabricated using a biaxial electrospun method that incorporated TGFβ2 concentrations at 0, 10, 100 ng/mg. 2. Constructs were crosslinked in 0.5% w/v genipin for 24 hrs at 37°C. 3. The TEVGs (n=3 for each group) were implanted in the abdominal aorta of a Sprague Dawley rat for 5 days. 4. Before surgery and 5 days after implantation the TEVG was imaged using ultrasound. 5. Histological markers were used to evaluate host response. . . . 38

11 Compliance, diameter, and maximum velocity of 0, 10, 100 ng/mg of constructs. Orange and blue bars indicate compliance-matched and hypocompliant TEVG implants, respectively. The red dashed lines represent rat aorta. The compliance matched constructs became less compliant as the concentration of TGFβ2 increase, while the hypocompliant construct remained stiff over all concentration. The diameter and maximum velocity remained similar to rat aorta for all groups. $**$ = p<0.01 and # = p<0.0001 in reference to rat aorta 46

12 Compliance, diameter, and maximum velocity of 0, 10, 100 ng/mg of constructs. Orange and blue bar graphs indicate compliance-matched and hypocompliant TEVG implants, respectively. All hypocompliant grafts had a similar implant thickness and cells inside & outside the TEVGs. The increase of TGFβ2 in the CM constructs reduced the amount of cells in the construct, but increased the abluminal cells in the 100 ng/mg group. Scale bar is 100 μm. The compliant-match 100 ng/mg group was also found to be slightly thinner than the 10 ng/mg group. n=3 for each group; $*$ = p<0.05 and $**$ = p<0.01 compared to rat aorta. 47

13 Compliance-matched proximal immunofluorescence images and immunohistochemistry results. The TEVG, nuclei, and each marker are green, blue, and red respectively. Immunohistochemistry quantification of the signal from MHC, pan macrophages (CD68), collagen, αSMC, calponin, Ki67, M1 (CD86), M2 (CD163), and elastin. Increasing the concentration of TGFβ2 decreased MHC signal and increased CD68 & collagen deposition in the 100 ng/mg group. $*$ = p<0.05; $**$ = p<0.01; X axis = TGFβ2 concentration (ng/mg); Y axis = Pixels of Interest/Total Pixels; Scale bar is 50 μm 49

14 Compliance-matched midgraft immunofluorescence images and IHC results. Construct is green, cell nuclei is blue, and maker is red. Immunohistochemistry quantification of the signal form αSMC, MHC, M2 (CD163), calponin, Ki67, pan macrophage (CD68), M1 (CD86), elastin, and collagen. The 10 ng/mg compliance-matched construct had significantly more MHC signal than the 0 and 100 ng/mg groups. No differences were found in any other markers. $*$ = p<0.05; $***$ = p<0.001; Y axis = Pixels of Interest/Total Pixels; X axis = TGFβ2 concentration (ng/mg); Scale bar is 50 μm 50

15 **Photoacoustic Imaging setup and Optical Properties of DiI.** A) Nd: YAG laser was tripled to 355 nm to pump an optical parametric oscillator (OPO) and produce tunable 5 nsec pulses between 410 nm – 670 nm. Laser light was coupled into a 1.6 mm diameter multimode glass fiber. The fiber connected to a PA flashlight adapter, including an optical assembly with a cylindrical lens to produce a line pattern on the heart [20]. The adapter also contained a water-filled cavity for acoustic coupling and an acoustic reflector, which ensures co-alignment of the light with the plane of ultrasound detection. A clinical ultrasound scanner (ZoneUltra, Zonare Medical Systems) and 7 MHz linear array (L10-5) recorded the raw acoustic signals (phase and amplitude) for ultrasound and PA imaging. The frame data were transferred to a PC for beamforming, post processing and analysis in MATLAB™. B) Optical absorption spectrum of DiI as measured with a photospectrometer (Ocean Optics, USB4000). 60

16 **Ultrasound and photoacoustic imaging of porcine myocardial samples stained with DiI.** Each row represents a sample stained with a different concentration of DiI (0 μg/ml, 38.4 μg/ml, 76.8 μg/ml, and 120 μg/ml). Column A) Cross sectional PE ultrasound images of samples embedded in Agarose™. Samples are outlined in green. Column B) Corresponding PA signal at 550 nm (near peak of DiI absorption). Column C) PA signal at 660 nm (low DiI absorption). Column D) Relative concentration of DiI after spectral decomposition. Green scale bar represents 2 mm. 64

17 **PA Calibration Curve for DiI.** The pixel values over the ROI were averaged and plotted against the prepared concentration of DiI for each sample. The equation for the best fit line (dashed red) and R2 value are also indicated. All concentration values are in μg/ml. Based on the PA signal without DiI (blue dashed line), the sensitivity of PA for detecting the dye in the samples was approximately 2 μg/ml. 65

18 **Increase in PA Signal near LADCA during DiI Perfusion.** (A) Cross sectional PE image of an ex vivo porcine heart. (B) Co-registered PA image at 550 nm during infusion of 2.4 μg/ml DiI. Vessel pressure was maintained at 70 mm Hg. C) Average PA signal over time inside dashed green box during infusion of DiI. The PA signal increase is observed in myocardial tissue adjacent to the coronary (CA) vessel. The scale bar denotes 2 mm. 66

19 **Estimation of DiI diffusion in the heart near the LADCA.** (A) Cross sectional PE ultrasound image over LADCA. (B) Co-registered PA image at 550 nm with a dynamic range of 40 dB. The PA spectra over regions of interest marked with "X" are displayed in (C). Brown and blue regions are similar to the known absorption spectra of the myocardium and DiI, respectively. (D) Co-registered PE (gray) and unmixed PA signal for 60 μg/ml DiI concentration (following flush). Green box identifies the ROI for cumulative diffusion analysis. E) PA images over ROI (green box) for DiI concentration of 0 μg/ml (100% water), 2.4 μg/ml, 12 μg/ml, and 60 μg/ml. f) Diffusion area for each concentration based on PA signal over background. Scale bar is 2 mm. . . . 67

20 **Diffusion distance from LADCA.** (A) Cross sectional ultrasound image of the LADCA in the porcine heart. (B) Overlay of PE ultrasound (gray) and PA (hot) images Scale bar = 2 mm. (C) Calculation of diffusion distance from LADCA based on signal above threshold noise inside dashed box in (B). Diffusion distance for this example ranged from 0.6 to 1.5 mm. Scale bar = 1 mm. 68

21 **Pulse Echo and Photoacoustic Imaging of DiI-Coated Cardiovascular Stent.** (A) Zoomed-in photograph of sinusoidal pattern of stent; (B) Top view PE ultrasound image of stent at 7.1 MHz. (C) Top view photograph of stent with DiI/PCL + PDMS coating on top half. (D)-(E) Co-registered PE ultrasound (gray) and PA (hot) at 550nm image (D = long view, E = cross view) of stent in water with coating on top half. (F) Co-registered ultrasound and unmixed PA signal of stent implanted in the brachiocephalic trunk. Scale bar 2 mm. Green box highlights the stent in the blood vessel. 69

22 The HYPO$_{pcl}$ TEVG (blue) implanted into the sheep carotid. The graft was 9 cm in length and had a wall thickness of 400 μm. 76
1 Hypocompliant cross sectional immunohistochemistry quantification of αSMA, Calponin, MHC, Ki67, CD68 (pan macrophage), CD86 (M1), CD163 (M2), elastin, and collagen signal 79
2 Hypocompliant longitudinal immunohistochemistry quantification of αSMA, Calponin, MHC, Ki67, CD68 (pan macrophage), CD86 (M1), CD163 (M2), elastin, and collagen signal 80
3 Hypocompliant cross sectional immunohistochemistry quantification of αSMA, Calponin, MHC, Ki67, CD68 (pan macrophage), CD86 (M1), CD163 (M2), elastin, and collagen signal 81

Preface

I want to personally thank the guidance of my professors, colleagues, friends, and my family. This long journey would not have been possible without you. I would like to thank all those who have supported me through my research and study. I am especially grateful to my graduate committee consisting of Drs. Jonathan Vande Geest, Russell Witte, Kang Kim, and Morgan Fedorchak. I want to personally thank my research advisor Dr. Jonathan Vande for his advice, guidance, patience, encouragement, and making me move across the country twice. This journey would not have been possible without his guidance and his help has gone beyond just my research work. Whenever I had a problem with my research or my writing I could always count on him for support and rewrites. Also I would like to thank Dr. Witte for forcing me to finally learn how to program. I thought it may never happen and it us such a useful tool!

I would like to thank all the staff and coworkers I have worked with at the University of Arizona and University of Pittsburgh. I want to extend my thanks to all of the past coworkers from the Soft Tissue and Biomehanics Laboratory specifically Ehab Tamimi, Shinichi Higuchi, Reza Behkam, Hirut Kollech, Jr Jiun Liou, Ali Behrangzade, Catalina Ardila, Corina MacIsaac, and the countless army of unnamed undergraduate students. A special thanks to Dr. Higuchi for all of his help on the rat surgeries and always being available, if only all doctors could be as available as you.

I dedicate this dissertation to:

My parents, Ken and Jean Furdella that raised me, supported me, taught me, frustrated me, fixed my houses, and helped me.

1.0 Introduction

1.1 Overview

The primary goal of this section is to further describe the basic concepts and methods covered throughout this dissertation. First, the impact of coronary heart disease (CHD) and peripheral arterial disease (PAD) will be put into perspective. Next, the basic anatomy of the blood vessel and the progression of atherosclerosis will be described. The following section will cover the current treatmentment methods and success rates for CHD/PAD procedures. Lastly, an in-depth analysis of the tissue engineered vascular graft as an intervention for CHD/PAD with a discussion of the graft's fabrication, implantation, and in vivo animal testing.

1.2 Coronary Heart Disease and Peripheral Arterial Disease Statistics

CHD is caused by the buildup of fatty plaque on the vessel wall (atherosclerosis) that limits the blood flow to the coronary vasculature, **Figure 1-A**. This limited blood flow can result in a heart attack and ultimately lead to death. CHD affects over 18.2 million people in the United States with over 365,000 deaths annually [1, 2]. This disease is so prevalent that a heart attack occurs every 40 seconds [1].

PAD is also cause by atheroslcerosis but it acts on the peripheral arteries in the leg or upper body rather than the coronaries. This disease often goes overlooked as the symptoms can go unnoticed or be as mild as leg cramping. Severe cases of PAD can manifest into amputation of the limb or spread throughout the body and to lead to CHD or stroke [3, 4]. In the U.S., PAD is estimated to affect more than 6.5 million people over the age of 40 [5].

As alluded to throughout this section, atherosclerosis is a dangerous and harmful condition that can affect multiple sections of the body. Finding an improved treatment to combat this disease is ideal for saving thousands of lives each year.

1.3 Surgical Treatment of CHD and PAD

The two main surgical procedures for treating CHD and PAD are bypass surgery or percutaneous transluminal angioplasty, **Figure 1**. These procedures help to restore flow to the disease vessel by either dilating the vessel, compressing the plaque, or diverting flow. Before going into detail about these procedures, that other methods to treat CHD/PAD such as atherectomy (removal of plaque), treatment through medication, and diet/exercise, but these are outside the scope of this dissertation.

The percutaneous route offers a wide array of clinically approved interventions. The first and oldest intervention is the balloon angioplasty, **Figure 1-B**, which threads a balloon catheter through the vasculature to the diseased site and inflates a balloon to compress the plaque. The initial effects of this procedure are encouraging as flow is immediately restore, but shortly after the vessel would restenosis or renarrow [6]. The next major breakthrough was the incorporation of a stent or metal mesh work on top of the balloon catheter to prop over the vessel, **Figure 1-C**. This permanent implant has improved upon the balloon angioplasty procedure and prolonged patency, but still has led to a significant degree of restenosis [7]. Researchers have added drugs like paclitaxel or rapamycin to the stent to prevent restenosis. These drugs have helped reduced the restenosis rate, but have lead to thrombosis at later time points from the lack of cellular infiltration [8, 7]. Ongoing research is continuing to evaluate the ideal drug delivery rate and stent design [7].

The second major surgical option to treat CHD/PAD and the primary focus of this dissertation is bypass surgery which diverts flow around the diseased location to restore blood flow, **Figure 1-D**. This procedure is more invasive than the percutaneous route, but is often required due to the advanced degree of atherosclerosis or widespread disease. The autologous vessel is the current gold standard for the bypass surgery, but is often unavailable due to widespread vascular disease [9]. The patency of the autologous vessel after bypass surgery is often less than 50% at 9 years [10]. In order to improve upon this, the focus of this dissertation will be to evaluate alternative vascular graft options.

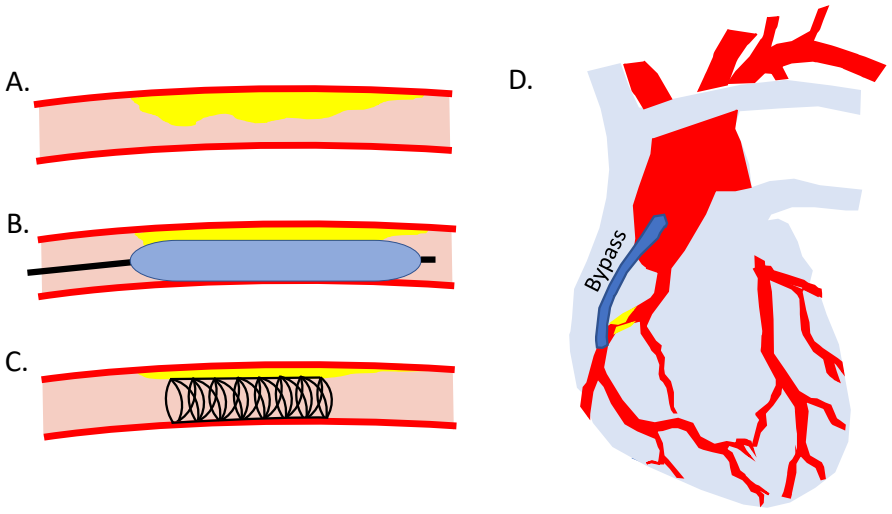

Figure 1: A) Atheroslcerotic vessel - showing plaque that is narrowing the lumen of the vessel; B) balloon angioplasty - inflated balloon, which is compressing the plaque on the vessel wall; C) stent deployment in an atherosclerotic vessel that has restored blood flow; D) coronary artery bypass - vascular graft from the aorta to coronary to bypass the narrowed artery in the heart.

1.4 Anatomy of the Blood Vessel

In order to create an autologous graft alternative, it is important to understand the blood vessel anatomy. The blood vessel is broken up into three main parts the tunica intima, tunica media, and tunica adventitia, **Figure 2**. The tunica intima is the inner most layer of the blood vessel that primarily interacts with the blood and acts as a barrier to prevent thrombosis. This layer is the thinnest of the three and is composed of a single layer of endothelial cells. Moving to the middle part of the vessel, the tunica media is the muscular and structural region that is responsible for dilation and constriction. This region is made up of SMCs, connective tissue, and elastin. Vascular tone is modified by the SMC response to various local or global stimuli. The outer most layer of the blood vessel, the tunica adventitia, acts as a structural support and helps keep its shape. This portion of the vessel is composed of connective tissue with cells such as macrophages and fibroblast.

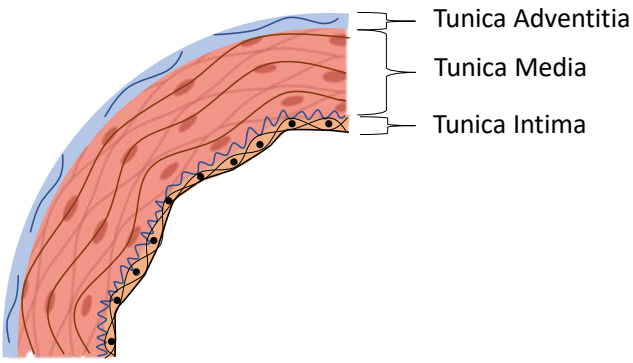

Figure 2: Anatomy of the blood vessel showing the three layers (inside to outside): tunica intima, tunica media, and tunica adventitia. The tunica intima is composed of a single layer of endothelial cells and acts as a barrier to prevent thrombosis. The tunica media is composed of elastin and SMCs, which are responsible for dilation and constriction of the vessel. The tunica adventitia is composed of connective tissue that helps to anchor the vessel in place.

1.5 Atherosclerosis

Over time, the healthy blood vessel starts to age and disease can creep in. The most common vascular disease is atherosclerosis or the deposition of fatty plaques on the vessel wall, **Figure 1-A**. This disease can start in the first or second decade of life and progresses throughout the lifespan of the person [11]. This disease starts from chronic damage to the endothelial cells from hypertension, hyperlipidemia, smoking, and many other factors [12]. Continued damage to the endothelium results in endothelial dysfunction that increases the permeability of the vessel and promote cellular adhesion. Luminal cells and SMCs from the medial layer migrate to the intima layer and engulf the local lipids. These cells start to form a fibrous lesion with a lipid core and over time these lesions or plaques become more complex with calcification and ulcerated luminal surface. Eventually these lesions can become so long and diffuse that blood flow in the vessel is limited or nonexistent which in turn could result in a heart or stroke. These narrowed lesions are also at a high risk of clotting or thrombosis. Hence, there is a need to treat these vessels and restore blood flow.

1.6 Tissue Engineered Vascular Graft and Design

The tissue engineered vascular graft (TEVG) is an artificial blood vessel that can be used to bypass the obstructed or narrowed blood vessel for CHD and PAD. The ideal TEVG will be an acellular off-the-shelf implant that will remodel into a fully functional vessel over time. The goal of the implant is to remain patent, promote cellular infiltration, and encourage positive remodeling of the TEVG. Some key advantages of a TEVG are that it can be tailored to the host in terms of mechanics and composition, allow drug delivery, and not require a secondary surgical site, which is true for autologous vessel bypass grafting [13, 14]. Achieving the ideal TEVG for small diameter (< 5 mm) applications has not yet been achieved, likely due to graft design parameters including but not limited to material choice, implantability, compliance, and antithrombogenicity [15, 16]. The need for a TEVG still remains, however, as native vasculature, current gold standard, is often unavailable due to widespread disease and in clinical applications where autologous grafts are not currently in use (ateriovenous shunting).

The selection of materials in TEVG design plays a vital role in the success of the graft. Native and synthetic polymers have often been the go-to choice for TEVG researchers due to their mechanical properties, biocompatibility, degradability, and chemical versatility [17, 18, 19]. Early on, synthetic vascular grafts (DACRON or PTFE) gained traction in the treatment of peripheral arterial disease but, these grafts have generally acted as a mechanically strong inert material for blood to flow through rather than a medium that promotes vessel remodeling. Other synthetic materials such as polycaprolactone (PCL) also have a high mechanical strength, but can also degrade over time to allow for remodeling. While a high concentration of PCL in the TEVG can be detrimental [20], balancing this polymer with a natural biopolymer (e.g., gelatin). To make this PCL:gelatin TEVG implantable, the graft must also include a cross-linking agent to prevent gelatin degradation. Specifically, a cross-linking agent (e.g., UV light, glutaraldehyde, genipin) typically interacts with free amine groups in the gelatin. Recently, genipin (extract from the gardenia fruit) has become a preferred replacement for other cross-linking agents (glutaraldehyde [21]) as it has been shown to reduce in vivo calcification, cytotoxicity, and increase the strength of

the gelatin fibers [22, 23, 24, 25, 26]. Modulating gelatin degradation is also vital to drug delivery from the TEVG. Previous work has demonstrated that increasing the gelatin concentration in TEVGs leads to an increased in vitro drug delivery of TGFβ2 release [27]. By varying amount of gelatin and concentration of drug, one can potentially modulate cellular and extracellular activity around/inside the implant. Incorporation of all of these factors into a TEVG could improve the functional performance of the graft in small diameter applications. This work will look to further evaluate the affects of compliance and drug delivery from an implanted TEVG.

1.7 Preclinical Analysis of TEVGs

Before moving to in vivo work, the researcher should perform some preliminary experiments on the TEVG. These tests can consist of the following: suture retention, burst pressure, mechanics, platelet adhesion, compliance, cytotoxicity, degradation, release profile, in silico testing, and many more [13]. This work will help to elucidate how the construct will perform in vivo and help the researcher narrow down their constrains. For this work, the majority of the preliminary experiments were performed by Tamimi et al. and Ardila et al [28, 29]. These studies demonstrated how compliance and TGFβ2 can be tuned in a TEVG and this dissertation will further evaluate these concepts in an in vivo model.

Once preliminary work is complete, preclinical testing is the next step and is generally performed in a small animal model, mouse or rat. These small animals provide a high throughput model for initial formulation studies and can provide a large sample size [30]. For TEVG research, the rat model tends to be the animal of choice due to its slightly larger vessel size and was selected for this dissertation [30]. The TEVG is most often implanted into the rat abdominal aorta in line with blood flow with patency and cellular infiltration as the assessed outcomes. Initial cellular infiltration into the scaffold can occur within days, while full cellularization can take months depending on the scaffold design. The patency of the graft is an indicator of success, but due to the differences in the clotting cascade of the rat this model is limited and requires the use of a larger animal [31].

Large animal models are often the next step after a successful small animal study. For example, the new TEVG X showed excellent patency, positive graft remodeling (ECM disposition) and, cellular infiltration in the rat model. This data would suggest that a larger animal model is warranted. The large animal model for the TEVG tends to the sheep or porcine carotid or coronary due to similarities in clotting mechanisms, long length of implant, and similarity to humans [30]. In this dissertation, we will look at future work using a pig coronary to assess drug delivery using photoacoustic imaging and implant a sheep carotid with a TEVG to evaluate the initial patency.

1.8 Hypotheses and Specific Aims

This dissertation has sought to further highlight the the affect TGFβ2 and compliance has on TEVG design. The objective of this work was to quantify cell infiltration, cell type, and extracellular matrix production while using ultrasound, photoacoustic imaging, multiphoton microscopy, and histology. This research will lead to a better understanding of how compliance positively affects TEVG remodeling, TGFβ2 affect on cells in vivo, and promote noninvasive imaging in small animals. The objective above will be testing in the following aims:

Hypothesis 1: Compliance-matched TEVGs will promote SMC infiltration and positive remodeling of the TEVG compared to a hypocompliant graft in a rat aortic interpositional implantation model.

Specific Aim 1: Determine the in vivo compliance, patency, cellular infiltration, and extracellular matrix production of hypocompliant and compliance-matched TEVGs when implanted in the aorta of Sprague Dawley rats (n=7) for 28 days. Rationale: Compliance mismatch is known to be a cause for TEVG failure and our laboratory has the unique ability to modify these properties. Therefore, we will leverage this capability to quantify how compliance alters the cellular infiltration of our TEVG.

Hypothesis 2: Release of transforming growth factor β2 (TGFβ2) from a TEVG promotes acute cellular ingrowth in a rat aortic interpositional model.

Specific Aim 2: Use immunofluorescence and second harmonic imaging to assess cell infiltration and ECM remodeling of a TGFβ2 (0, 10, and 100 ng/mg) eluting hypocompliant and compliance-match TEVG in the aorta of Sprague Dawley rat (n=3) following five days of implantation. Immunofluoresence and two photon imaging will be used to evaluate the cellular content, collagen, and elastin production in the explants. Rationale: Our preliminary data suggests that modulation of TGFβ2 can promote the migration and proliferation of vascular smooth muscle cells (SMC) into a TEVG. We therefore believe that the addition of TGFβ2 will promote cellullar ingrowth.

Hypothesis 3: Photoacoustic Imaging (PA) and spectroscopy can noninvasively quantify the release of fluorescent molecules from vascular implants.

Specific Aim 3: Develop a Photoacoustic Imaging (PA) approach to quantify drug surrogate concentrations in cardiovascular applications. PA imaging with spectral decomposition will be used to differentiate drug surrogate concentration from porcine heart tissue to quantify the delivery of a drug surrogate. Rationale: Imaging modalities with increased depth of penetration will open new avenues of investigation for tracking the release of fluorescently labelled drugs and cytokines in animal models. This may be useful for future in vivo or in situ assessment of the biodegradation and cytokine elution from our vascular graft.

2.0 In-vivo assessment of a tissue engineered vascular graft computationally optimized for target vessel compliance

For this aim, the effect of compliance on TEVG design was evaluated between two hypocompliant and a compliance-matched grafts implanted in the abdominal aorta of a Sprague Dawley rat. The compliance-matched constructs were modified by our laboratory's custom computational/experiential approach that varies composition. The two hypocompliant grafts' compliance were modified by either composition or increased crosslinking agent. Cellular infiltration and extracellular component were evaluated at 28-days [32].

2.1 Introduction

Compliance mismatch is a common cause of TEVG failure and often overlooked in preclinical design. [33, 34, 35]. The majority of TEVG tend to be hypocompliant or less compliant than the target native vasculature [36, 37, 38, 39, 40, 41]. These hypocompliant TEVG cause hemodynamic environmental changes or non-homeostatic mechanical strains that result in the development of intimal hyperplasia, thrombus formation, and ultimately graft failure [42, 43, 44, 34]. In this aim, we have developed a method to modify TEVG compliance by composition and crosslinking concentration. The compliance of the TEVG will be modified and evaluated using in vivo ultrasound and histology to demonstrate the effects of compliance on vascular graft design.

2.2 Methods

2.2.1 TEVG Characterization and Fabrication

2.2.1.1 Preparation of Rat Aorta

All protocols were approved by the University of Pittsburgh Institutional Animal Care and Use Committee. The infrarenal abdominal aorta of 13 male Sprague Dawley rats (175-

225g) were extracted and any adventitial connective tissue was removed gently with forceps. The aorta, 1.5 cm in length, was then placed in phosphate-buffered saline (PBS) pH 7.4 (Thermo Fisher Scientific, Waltham, MA) with 1% (v/v) Gibco Penicillin-Streptomycin 10,000 U/mL (Thermo Fisher) and 1% Gibco Amphotercin B (Thermo Fisher) for 24-48 hours post mortem at 4°C before beginning of compliance testing to prevent contamination of the tissue.

2.2.1.2 Compliance Testing

The compliance of rat aorta was tested using our custom microbiaxial optomechanical device (MOD) [45, 46, 47, 48, 49, 50, 51]. This device has been extensively used in our laboratory to mechanically characterize tubular and planar vascular tissues and biomaterials. Briefly, each sample was cannulated on opposing ends using a 1 mm outer diameter (OD) glass capillary, tied with suture, and sealed using super glue (Loctite). The cannulated sample was then mounted inline within the MOD bath that was filled with saline, kept at 37°C. The arteries were preconditioned circumferentially (0 to 120 mmHg) and axially stretched (15% strain) seven times prior to the collection of final diameter and pressure. The outer diameter (OD) of each sample was measured using a digital camera as intraluminal pressure was slowly increased from 0 to 120 mmHg. Compliance was quantified as

$$Compliance = \frac{(OD_{120} - OD_{70})/OD_{70}}{50\text{mmHg}}. \tag{2.1}$$

2.2.1.3 Compliance Matching and Computational Optimization Routine

Specific construct formulations were determined using our developed computational optimization routine [28, 52]. Previously, our research group has developed a finite element optimization scheme (**Figure 3A**) to predict the thickness and Gelatin:PCL (G:P) ratio of an alternating layered construct that matches the compliance and geometry of rat aorta [28, 52]. Briefly, tubular TEVGs consisting of either 20G:80P, 50G:50P, and 80G:20P were fabricated and tested using the MOD device. Each construct was pressurized from 0 to 120 mmHg at 0, 5, 10, and 15% axial strain. From this testing, the material constants were collected from a Fung-type constitutive model and assign to gelatin and PCL, in silico.

Next, a computational optimization scheme was used to determine the TEVG's formulation to match a specified compliance (hypocompliant or compliance-matched). For this study, each construct consisted of 12 total layers with two alternating polymeric formulations. The optimization scheme uses Matlab (MathWorks Inc, USA) to generate an input file for the ABAQUS finite element solver (Dassault Systemes Simulia, France) which consisted of a four-node, reduced-integration, axisymmetric finite element model that simulated the compliance of the construct from 0 to 120 mmHg. For computational optimization, the constrained parameters were the construct's inner diameter, number of layers, and total thickness. The open design parameters were the G:P ratio and the thickness of each of the paired layers. The optimization function modified the open design parameters until the ABAQUS simulation matched the specified target compliance to within 1%.

2.2.1.4 Electrospinning Materials and fabrication

All TEVGs were fabricated using an electrospinning process, crosslinked in genipin, and tested for compliance. Polycaprolactone with a molecular weight 80,000 (Sigma-Aldrich, St. Louis, MO) and gelatin extracted from porcine skin (Sigma-Aldrich) were dissolved in 1,1,1,3,3,3-hexafluoro-2-propanol (HFP) (Sigma-Aldrich) to create a 10% w/v solution. All constructs were electrospun using IME technologies electrospinning device (Waalre, Netherlands). Briefly, electrospinning solutions were loaded into 5 ml BD syringes (BD Franklin Lakes, NJ), placed in a computer-controlled syringe pump, and connected to 1mm PTFE tubing. This setup was connected to a translating stage, 300 mm/s, and was expelled through a 0.6 mm ID stainless steel tip at a working distance of 10 cm with a climate-controlled chamber at 25°C and 30% humidity. The polymeric solutions were dispensed at a rate of 50 μL/min onto a 1.1 mm diameter steel rod rotated at 300 rpm with a 15-kV voltage difference. The two polymer formulations were sequentially dispensed horizontally and vertically (**Figure 3B**) from the IME electrospinning device which allowed for a multi-layer composition. During the electrospinning process, the syringe with the higher gelatin formulation was spun from the vertical nozzle. It should also be noted that during the electrospinning process, the user waited 4 minutes before starting the next layer. This waiting period allowed the inline pressure to dissipate and extrude all the material. Once completed, HYPO_{pcl} and

CM_{gel} were crosslinked in 0.5% (w/v) concentration of genipin (Wako Chemicals USA Inc, USA) in 200 proof ethanol for 24 hours at 37°C and shaken [28].

After crosslinking, half of the construct (1.5 cm) was compliance tested in our MOD device to confirm the construct met the desired compliance. Details regarding compliance testing are found in **Section 2.2.1.2**. Once confirmed, this half of the sample was embedded in O.C.T. Compound (Thermo Fisher Scientific, USA), frozen, cross-sectioned (10 μm) with Microm HM550 cryostat microtome (Thermo Fisher Scientific, USA), and imaged using bright field microscopy. Three locations along the length of the sample were averaged to determine the construct area, inner radius, and thickness using a Nikon 90i Eclipse fluorescence microscope (Nikon USA, USA). If the tested sample met the desired compliance, the other half of the sample (not tested) was implanted into the abdominal aorta of a Sprague Dawley rat. The implant sample's physical dimensions matched the test sample.

The formulations of the compliance-matched and hypocompliant (stiff) grafts were determined using the optimization scheme detailed in **Section 2.2.1.3**. The compliance-matched (CM_{gel}) construct was compliance-matched to rat aorta with a high gelatin content (layers composed of approximately 75G:25P and 50G:50P). The hypocompliant formation ($HYPO_{pcl}$) was composed of a high amount of PCL (layers composed of approximately 20G:80P and 35G:65P) and was targeted to 50% of the compliance value of the CM_{gel} grafts. This hypocompliant graft had a compliance similar to Dacron or ePTFE [53]. Both CM_{gel} and $HYPO_{pcl}$ grafts were crosslinked using 24 hours of 0.5% genipin. To further isolate the effect of compliance in grafts with larger gelatin percentages, a third group was added to the study - $HYPO_{gen}$. For this formulation we initially tested the CM_{gel} graft formulation in 0.5%, 1%, and 10% w/v genipin concentrations crosslinked for 24 hours at 37°C and found that the CM_{gel} formulation had a compliance similar to $HYPO_{pcl}$ when crosslinked in 10% w/v genipin. The hypocompliant construct was called $HYPO_{gen}$ and acted as another control group with a hypocompliant mechanical response, but with a gelatin content similar to the CM_{gel} group. The detailed construct formulations are provided in **Table 1**. Layers 1 and 2 (L1 and L2) are the repeating units of the grafts which total the 12 layers.

Table 1: Polymeric formulations, layer thickness, and crosslinking concentrations for the $HYPO_{pcl}$, CM_{gel}, and $HYPO_{gen}$ graft formulations.

Experimental Group	Layer 1 Ratio G:PCL	Layer 2 Ratio G:PCL	Individual Layer Thickness (μm)				Genipin Conc. (w/v)
			L1	L2	Repeats (L1+L2)	Total	
HYPO$_{pcl}$	20:80	35:65	8	5	6	78	0.5%
CM$_{gel}$	75:25	50:50	8	5	6	78	0.5%
HYPO$_{gen}$	75:25	50:50	8	5	6	78	10%

2.2.1.5 Suture Retention

The suture retention of each scaffold was determined using an in house custom made uniaxial device. Electrospun tubular constructs (n=6) around 1 cm in length were clamped distally in our uniaxial setup. A single 10-0 nylon (AROSurgical) suture was used to create a single loop approximately 2 mm away from the scaffold's proximal end. The free ends of the suture were secured to the upper clamp and any excess slack removed from the suture. The sample was then pulled at a rate of 2 mm/min until the suture tore out of the sample. The load displacement curve was used to determine the maximum force each sample held. Differences between groups were compared using a Kruskal-Wallis test.

2.2.1.6 Burst Pressure

Burst pressure of each scaffold (n=5) was quantified by increasing intraluminal pressure until catastrophic rupture occurred. For each test, the construct was cannulated on both sides with one end connected to a syringe pump (Harvard Apparatus, Holliston, MA) and the other clamped to form a closed loop. Saline was injected into the construct at 50 mL/min until failure. The maximum pressure (Weiss gauge, 0-60 psi) was recorded before failure and taken to be the burst pressure. Statistical differences between groups were first check for normality, transformed using a Box Cox, and compared using Kruskal-Wallis ANOVA with a Tukey post hoc.

2.2.1.7 Cytotoxicity

Each scaffold's degradation product was evaluated for cytotoxicity using rat aorta smooth muscle cells (RSMC (Lonza)) following closely the methods of Guan et al [54]. Cells were seeded at a density of 4.0 x 10^4 onto a 24-well tissue culture plate. Eluent from each construct (n=5, 8 mm in length) soaked in PBS for 24 hours was added to each well at 1:10 ratio (eluent:media). The positive control was sterile PBS:media (no degradation products). Cell viability was measured with an MTS assay (Promega) at 48 and 96 hours with media changes occurring ever 48 hours. For the MTS assay, 20μL of MTS solution was added per 100 μL media to each well, incubated for 2.5 hours, and the absorbance at 490 nm was recorded to determine cell viability. Results were compared to the control using a two way ANOVA and normalized.

2.2.2 Rat Implantation

2.2.2.1 Rat Interpositional Abdominal Aorta Surgery

TEVGs were implanted into the abdominal aorta of 8-week-old male and female Sprague Dawley rats (total M and F 11 and 10, respectively) and weighed on average (203±37 g) with n=7 for each group. Male and female rats were chosen in order to present results more broadly applicable to the rat population. For each surgery, the rat was anesthetized with isoflurane (3% for induction and 1% for maintenance). An abdominal medial incision (3-4 cm) was made using No. 10 scalpel. The small intestine and the cecum were extracted from the abdominal cavity, retracted to right upper quadrant, and covered with wet gauze. The abdominal aorta was dissected, isolated (1 cm portion above the aortic bifurcation), and generally 1-2 branches of the aorta were ligated and transected. About 1 ml of heparin was administered on the small intestine and into the abdominal cavity to prevent clotting. Two 30 g clips were applied at the iliolumbar artery and the bifurcation to prevent blood flow. The aorta was transected at the center and each lumen was irrigated by saline. For the anastomosis, it was initiated on the proximal vessel with stay sutures, 10-0 nylon, placed at the 3 and 9 o'clock positions. After placing 3-4 stitches on the anterior wall, the vessel was rotated 180^o clockwise to expose the posterior wall and 3-4 stitches were placed on the

posterior wall. This same procedure was performed on the distal location. Before the last suture was tied the lumen was irrigated and then the clips were removed. If oozing occurred, pressure was applied gently on the suture line which generally allowed for hemostasis. On some occasions an extra stitch was added when blood leakage was unable to be stopped. Each anastomosis had between 7-10 stitches per end with the average implant length consisting of 5.7±1.1 mm which is shown is **Figure 3C**. Blood flow was assessed by performing a patency test. Once complete, the small intestine and cecum were returned into the abdominal cavity. The rectus abdominis was closed with an interrupted 4-0 absorbable polyfilament suture, the skin was closed with buried 5-0 nylon suture, and the skin was stapled (to prevent the animals from chewing out their stitches). The average surgery time was around 1.75 hours with the anastomoses taking about 50 minutes. One animal in the CM_{gel} group was excluded from the study due to an unrelated death within the first three days. All other animals survived the duration of the study with little to no discomfort.

In days 1 to 3 post operatively, each rat received 0.5 mg/kg buprenorphine and 10 mg/kg cefuroxime intramuscularly twice a day to minimize pain and prevent bacterial infections, respectively. Carprofen (5 mg/kg) was also given at 24 and 48 hours post operatively to minimize inflammation. For solid medications, aspirin (pain reliever) and dipyridamole (blood thinner), were ground up with a mortar and pestle and mixed with jelly inside a miniature ice cream cone which also acts as another enrichment object for the animal. For the first week aspirin and dipyridamole were given to the rat at a concentration of 200 mg/kg and 250 mg/kg and decreased at weeks 2-4 to 100 mg/kg and 100 mg/kg, respectively. After 4 weeks, the rats were euthanized with carbon dioxide inhalation and cervical dislocation, the explant was recovered and place in 4% paraformaldehyde solution in PBS (Thermo Fisher Scientific, Waltham, MA), and later sectioned.

2.2.3 Graft Measurements and Quantification

2.2.3.1 In-vivo Ultrasound

High frequency Doppler ultrasound was used to evaluate graft patency, diameter, compliance, and velocity in-vivo. All longitudinal ultrasound data was collected using the VEVO

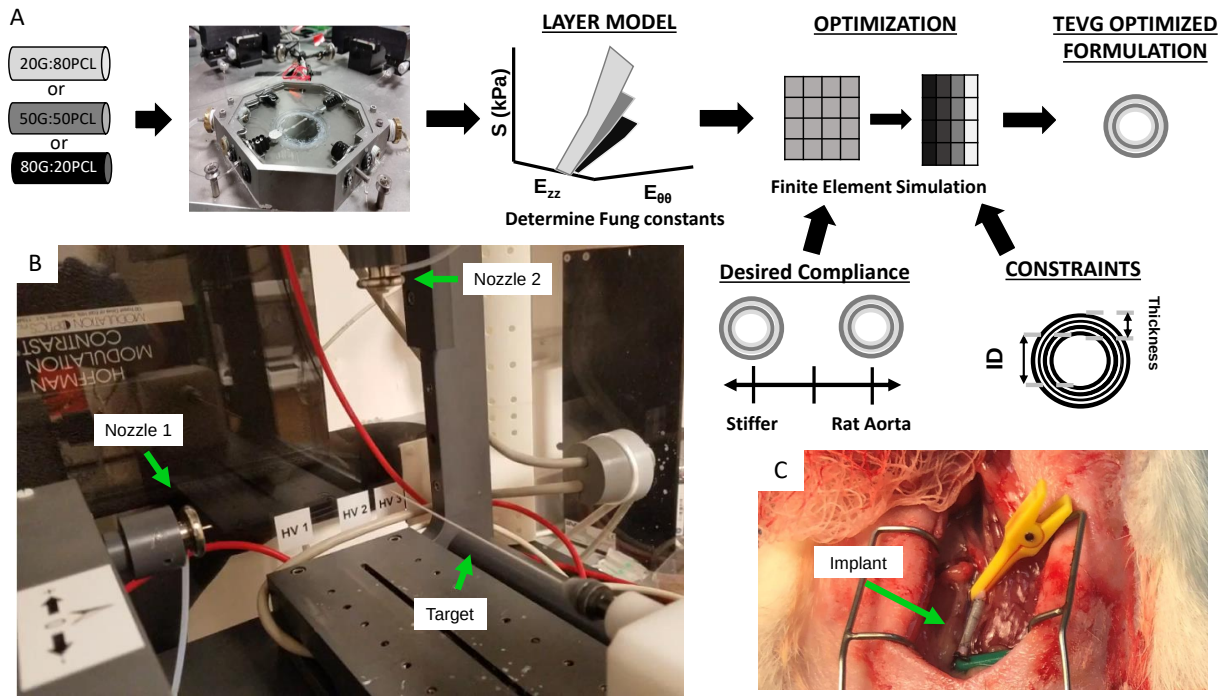

Figure 3: A) Overview of the optimization routine that demonstrates how mechanical testing of the vascular grafts lead to a computational optimizational scheme to calculate graft formulation; B) Electrospinning setup, demonstrating the two-nozzle setup of the device; C) Implantation of a CM_{gel} TEVG in the abdominal rat aorta.

2100 (FUJIFILM VisualSonics Inc, Canada) with a 30 MHz probe. In-vivo measurements were taken for each animal up to a week before surgery and at one, two, and four weeks post-implantation. It should be noted, that the VEVO 2100 was located in another facility which prevented immediate imaging post implantation. To collect the ultrasound data, the rat was anesthetized with isoflurane (3% for induction and 1% for maintenance), abdominal fur was removed using Nair Hair removal (Church & Dwight), applied ultrasound gel, and imaged. Cross-sectional in-vivo imaging was used to determine the aorta's location. Once located, the implant was imaged longitudinally. Patency was defined as an observable blood

flow under ultrasound imaging. Any nonpatent vessel was excluded from subsequent statistical analysis. At each time point, the maximum and minimum diameter of the implant was recorded over one cardiac cycle to determine the implant's average inner diameter and compliance using **Equation 2.1**. The average maximum velocity inside the implant was recorded using Doppler ultrasound and all measurements were taken inside the implant. All collected data was processed using the Vevo Lab software version 1.7.1 and adjusted for the probe angle using the approach described in Park et al. [55].

2.2.3.2 Preparation, Immunohistochemistry, and Fluorescent Imaging

The proximal and middle locations of each TEVG was evaluated for cell infiltration using immunohistochemistry. Each fixed sample was cut in the middle and separated into proximal and middle sections, frozen in O.C.T. medium, and kept at -80°C. All samples were sectioned at 10 μm using a Microm HM550 cryostat microtome. The middle samples were cut cross-sectionally while the proximal sections were cut longitudinally.

For immunohistochemistry, samples were rehydrated in PBS and soaked in 1% sodium dodecyl sulfate (Sigma-Aldrich, St. Louis, MO) in PBS for 15 minutes. The samples were next permeabilized in 0.3% triton X-100 (Sigma-Aldrich) for 15 minutes and blocked with 0.5% bovine serum albumin (Sigma-Aldrich), 0.3M glycine (Thermo Fisher Scientific), and 20% goat serum (Thermo Fisher Scientific) for one hour. Following blocking, all samples were incubated with a primary antibody over night at 4°C. α-Smooth muscle actin (αSMA, 1:100, Abcam), calponin (CAL, 1:100, Abcam) and smooth muscle myosin heavy chain (MHC, 1:100, Abcam) were used to detect smooth muscle cells. Ki67 was used to detect highly proliferative cells, thus acting as a surrogate for increased risk of intimal hyperplasia. Endothelial cells were detected using CD31 (1:100, Abcam) and macrophages using CD68 (1:100, Abcam), CD86 (1:100, abcam), and CD163 (1:100, Abcam), for inflammatory response, M1, and M2 macrophage phenotype, respectively. Elastin in the implant was detected using elastin Alexa Fluor antibody (Santa Cruz Biotechnology, Inc) which did not require a secondary antibody. After incubation and washing, the samples were incubated for 1 hour at room temperature with Alexa Fluor 488 Goat Anti-Rabbit IgG (Abcam, 1:1000) except for αSMA which was incubated with Alexa Fluor 488 Donkey anti-goat IgG (Abcam,

1:1000). Each sample was then washed and counterstained with DAPI mounting medium (Abcam).

Each marker was imaged using the Nikon 90i Eclipse fluorescence microscope. Briefly, full mosaic images of each entire sample were taken in the DAPI (excitation at 359 nm; emission at 461), FITC (excitation at 495 nm; emission at 519 nm), and Cy5 (excitation at 647; emission at 665) emission channels using a Nikon Plan Apo 10x/0.45 objective. The DAPI channel was used to identify cell nuclei, Cy5 was autofluorescence from the genipin crosslinking/implant, and FITC was the marker of interest. It should be noted that the FITC channel exposure time was consistent between each marker so that quantitative analysis could be performed.

2.2.3.3 Multiphoton Imaging

Multiphoton microscopy was performed on the Pitt Advanced Intravital Microscope at the University of Pittsburgh and used to evaluate collagen deposition within the implant (cross-sectionally and longitudinally). In this setup an Olympus BX51 upright scanning microscope (Olympus, Tokyo, Japan) was coupled into a 120-fs tunable pulsed laser (INSIGHT DS+DUAL, Newport, Irving CA) and Olympus XLUMPLFL 20x water emersion objective (NA 0.9). The second harmonic generation (SHG) signal of fibrillar collagen was imaged using an excitation of 780 nm and a collection of 377/50 nm. DAPI and autofluorescence was also imaged at 780 nm with a power of 25-31 mW and collected with 525/50 nm and 620/60 nm bandpass filter, respectively. The signal was collected over multiple 499 x 499 μm fields of view with a 5 μm z-step-size through the thickness of the sample. Montage slices of each channel (377, 525, and 620 nm) were converted into maximum intensity projection and used for image quantification.

The percent construct remaining, cells signal inside the construct, and collagen throughout the construct were quantified from each image. Bright field images before implantation (see **Section 2.2.1.4**) and multiphoton images of the explant were used to calculate the percent construct remaining: $((TEVG_{original} - TEVG_{explanted})/TEVG_{original}) * 100$. For cells inside the construct, ImageJ (Fiji) was used to isolate the cells inside the construct which were counted using the analysis particle function. The percent collagen throughout

the construct was determined similarly to antibody image processing and is described in **Section 3.2.4.4**.

2.2.3.4 Image Processing

Cellular and extracellular markers were evaluated using Matlab image processing to determine differences between groups. It should be noted that the FITC channel was changed to red and the Cy5 to green color. Following faux coloring, all data sets had 3 channels which were as follows: cell nuclei channel (blue), implant channel (green), and antibody or collagen channel (red). Each antibody channel was sampled and then binarized to identify the signal of interest and remove noise. The implant channel was used to separate antibody signal into three regions: lumen, graft, and abluminal. The lumen region was designated as the section from the inner boundary of the implant to the lumen. The graft and abluminal regions were composed of the inside or outside the implant, respectively. The area of the abluminal region was limited to a 25% increase of the exterior diameter of the implant. To calculate the amount of signal per antibody in a certain region, the total number of antibody pixels was divided by the total number of the section's pixels (lumen, graft, or abluminal). For the cross-sectional samples, the whole implant was used for each sample and averaged among all rats in the specific group. The ratio of CD163 to CD68 signal was also evaluated during this process to help identify differences in macrophage phenotype. The cross-sectional samples were also used to calculate the percent endothelialization and luminal thickness. For percent endothelialization, the CD31 signal length was divided by the lumen circumference and multiplied by 100. For luminal thickness, each sample was measured at 4 locations and evaluated for significant differences using a Box Cox transformation and a mixed effect model.

In the longitudinal sections, the first proximal 150 μm (lumen, graft, or abluminal) was processed as described in the paragraph above. The 150 μm portion was selected as this was the shortest segment of the longitudinal samples that were imaged for all groups. The sample size for the longitudinal samples was n=4 due to initial processing. Luminal thickness was measured three times along the length of the image and averaged.

2.2.3.5 Statistical Analysis

Sex differences were assessed using a paired t-test, however no differences were found and as such gender was not carried through subsequent statistical analysis. After processing, the samples were checked for normality and nonnormal data was transformed using a Box Cox transformation. A linear mixed effect model with a Tukey post hoc was used to statistically analyze how each outcome was influenced by graft type at a specific region in the proximal or middle location. The random effect was the sample and the fixed effects were graft type and region (lumen, graft, and abluminal). The total implant results were evaluated using an ANOVA or Krustal Wallis with a Tukey or Dunn post hoc depending on the normality of the sample.

Preliminary work using αSMA marker was used to determine the sample size for each group in the study. Specifically, a power analysis was calculated using an alpha of 0.05 and a power of 80%.

2.3 Results

2.3.1 Construct Characterization

Pre-implantation compliance, thickness, and inner diameter using bright field microscopy are shown in **Figure 4**. The $HYPO_{gen}$ and $HYPO_{pcl}$ constructs pre-implantation were found to be stiffer than those in the CM_{gel} ($p<0.05$) group and there was no gross delamination between electrospun layers in any construct. The average thickness of each construct was 104.2 ± 15.9, 88.35 ± 11.1, and 114.4 ± 10.1 μm for the $HYPO_{pcl}$, CM_{gel}, and $HYPO_{gen}$ groups, respectively. The $HYPO_{gen}$ group was thicker than CM_{gel},($p = 0.03$) suggesting that genipin was the cause of the increase. The inner radius of the construct was not found to be statistically different across groups. The results of this testing confirmed the desired compliance of our constructs.

The suture retention for $HYPO_{pcl}$, CM_{gel}, and $HYPO_{gen}$ groups was 43.47, 10.83, and 13.22 g, respectively. The burst pressure for $HYPO_{pcl}$, CM_{gel}, and $HYPO_{gen}$ groups were 1435, 504, and 497 mmHg, respectively. The suture retention and burst pressure for the

HYPO$_{pcl}$ group was greatly increased compared to CM$_{gel}$ and HYPO$_{gen}$ with only HYPO$_{gen}$ to HYPO$_{pcl}$ burst pressure not found to be significant, p<0.05.

The cytotoxicity from genipin in each construct was tested by evaluating the degradation products at 24 hours. The CM$_{gel}$ and HYPO$_{gen}$ showed a slight reduction in cell number at 48 hours and no differences occured between the experimental groups and the positive control and 96 hours.

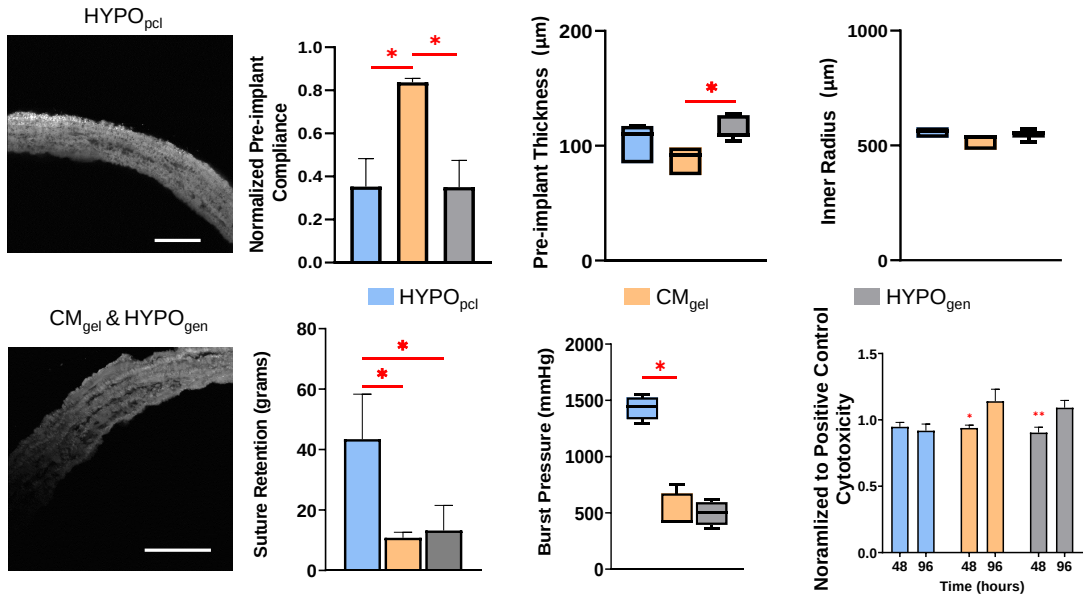

Figure 4: Pre-implantation images, compliance, thickness, inner radius, suture retention, burst pressure, and cytotoxicity of the HYPO$_{pcl}$, CM$_{gel}$, and HYPO$_{gen}$ TEVGs. The scale bar is 50 μm. The compliance of the CM$_{gel}$ constructs matched rat aorta, while the HYPO grafts were over twice as stiff. HYPO$_{gen}$ TEVGs were found to be slightly thicker than the CM$_{gel}$. All constructs had a similar inner radius, around 550 μm. The suture retention and burst pressure of the HYPO$_{pcl}$ was greatly increased compared to the CM$_{gel}$, and HYPO$_{gen}$ TEVGs. The CM$_{gel}$ and HYPO$_{gen}$ TEVGs had a slight reduction of cell number at 48 hours and no differences at 96, while the HYPO$_{pcl}$ had no differences at both time points. $*$, p<0.05

2.3.2 Rat in-vivo Ultrasound

The in vivo ultrasound results demonstrated that $HYPO_{pcl}$, CM_{gel}, and $HYPO_{gel}$ grafts had a patency rate of 6/7, 5/7, and 6/7, respectively. These results were subsequently confirmed by histological analysis. The ultrasound sample size for each group was at least n=3 for each time point with an exception of the CM_{gel} group having an n=2 at the 2 and 4 weeks. The CM_{gel} group had a similar compliance to rat aorta throughout the study. In-vivo compliance measurements demonstrated that our mechanically optimized graft (CM_{gel}) remained compliance-matched throughout the implant period, while one or both of the HYPO (stiffer) grafts demonstrated significant reductions in compliance compared to CM_{gel} at 2 and $HYPO_{gel}$ 4 weeks (**Figure 5**). Ex-vivo analysis of compliance was unable to be conducted due to the limited amount of sample remaining from IHC. The average diameter of the implants stayed relatively constant and similar to rat aorta throughout the study. The only notable difference in diameter between groups occurred at the 4-week time point where two $HYPO_{gen}$ grafts showed an increase in construct diameter, however this result was not statistically significant.

The average maximum velocities of the HYPO grafts at two weeks was different that rat aorta, $p<0.05$ **Figure 5**. There was also was a decrease in blood velocity for $HYPO_{gen}$ grafts from 1 week to 2 and 4 weeks ($p<0.05$). We attributed the decrease in velocity in the $HYPO_{gen}$ grafts to 2 graft dilations.

2.3.3 Multiphoton Imaging

The results of construct degradation, cellular infiltration, and luminal thickness using multiphoton imaging are shown in **Figure 6**. More degradation ($\sim$70%) occurred in the CM_{gel} and $HYPO_{gen}$ compared to the $HYPO_{pcl}$ constructs ($\sim$30%). This high degradation rate led to an increase in cellular infiltration with more cells in the $HYPO_{gen}$ vs. $HYPO_{pcl}$, $p<0.05$. Luminal thickness was not statistically different between all grafts in the proximal and middle locations.

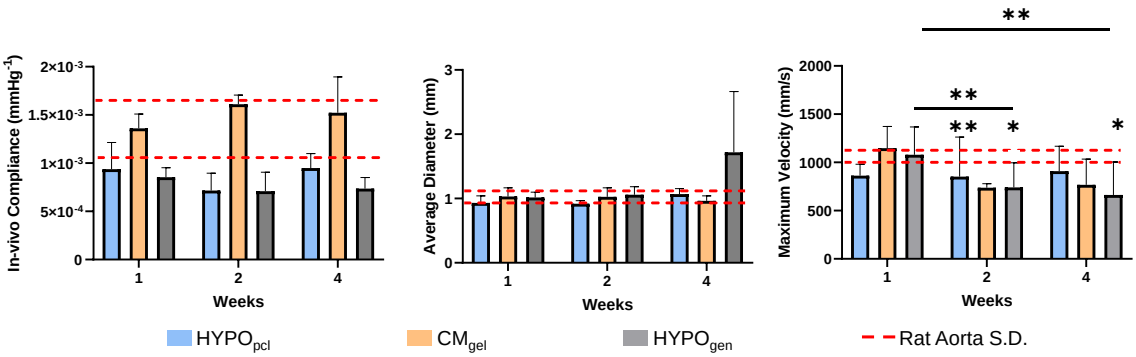

Figure 5: In vivo ultrasound measurements of compliance, average inner diameter, and velocity in the HYPO$_{pcl}$, CM$_{gel}$, and HYPO$_{gen}$ TEVGs. The CM$_{gel}$ constructs matched native rat aorta compliance over time, while the HYPO grafts were generally less compliant. The average diameter stayed relatively consist over the one-month time point except for the HYPO$_{gen}$ TEVGs that had two graft dilations. The average velocity for the CM$_{gel}$ and HYPO$_{gen}$ TEVGs tended to decrease over the implantation period and the HYPO$_{pcl}$ TEVGs stayed consistently below native rat aorta velocity. $*$, $p<0.05$, $**$, $p<0.01$

2.3.4 Quantitative Immunohistochemistry

Representative fluorescent images of both the cross-sectional middle and longitudinal proximal locations of our TEVG are shown in **Figure 7**, **Figure 8** and **Figure 9**, respectively. The green and blue regions in these images represent the construct and cell nuclei, respectively. **Figure 7** shows representative cross-sectional images of the image with the specific marker in red (αSMA, CAL, MHC, Ki67, CD68, CD163, CD86, and elastin). These markers were quantitatively assessed using image processing in Matlab and the results are shown in **Figure 8**, and **Figure 9**.

In the middle location, all regions (lumen, graft, and abluminal) and the total αSMA signal were found to be higher in the HYPO$_{gen}$ & CM$_{gel}$ vs. HYPO$_{pcl}$ groups ($p<0.05$). For the proximal location (**Figure 8**), there were no αSMA signal differences between the grafts regions or throughout the total implant.

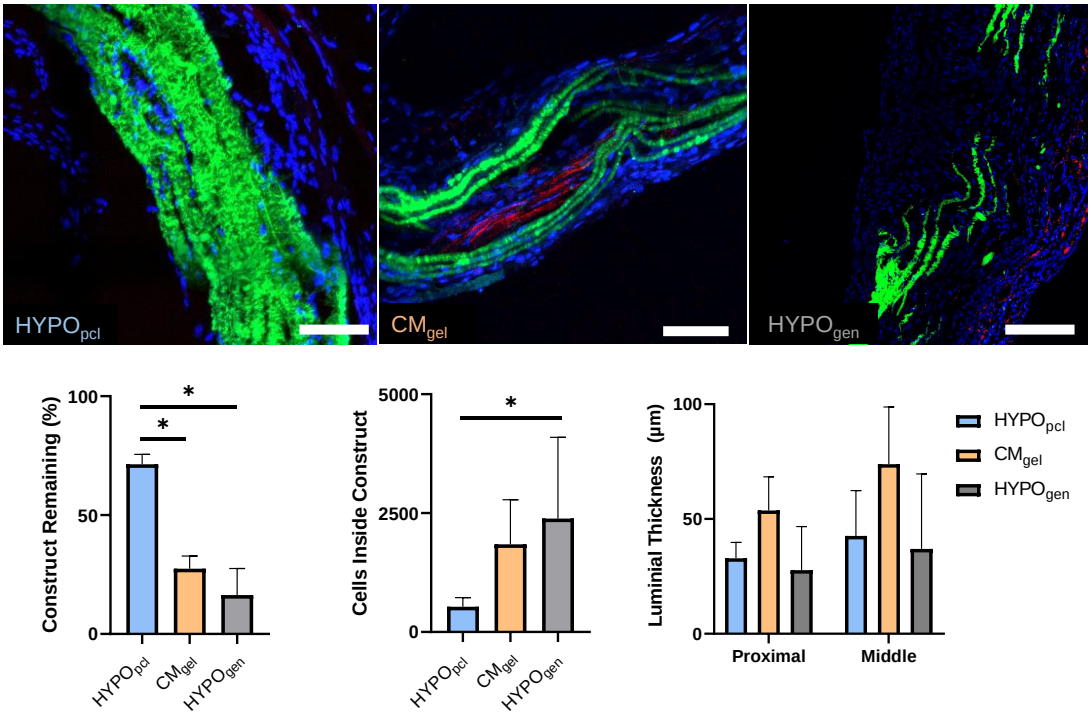

Figure 6: Top) Cross-sectional multiphoton implant images of $HYPO_{pcl}$, CM_{gel}, and $HYPO_{gen}$ TEVGs; Green, blue, and red represent the implant, cell nuclei, collagen, respectively; The scale bar is 50 μm. Bottom) Differences in the amount of construct remaining, cells inside our TEVGs, and luminal thickness. The $HYPO_{pcl}$ TEVGs had less construct degradation and cellular infiltration than compared to CM_{gel} and $HYPO_{gen}$ TEVGs. The average luminal thickness was found to be similar between all implants. $*$, $p<0.05$

The proximal location of the implants displayed an increase in the more phenotypic SMC markers CAL & MHC for compliance-matched TEVGs compared to either of the HYPO constructs (**Figure 8**). In particular, we observed an elevation in total CAL signal in the CM_{gel} constructs compared to either of the HYPO formulations. This elevation was similar to an increase in MHC in our compliance-matched TEVGs compared to both HYPO grafts when quantifying signal within the graft itself. These phenotypic SMC differences between graft type were not observed in the middle location of our TEVGs (**Figure 9**).

The total Ki67 signal in the middle location of all grafts was increased in $HYPO_{gen}$ vs. $HYPO_{pcl}$ TEVGs, $p<0.01$. Throughout the regions in the middle location, Ki67 was also

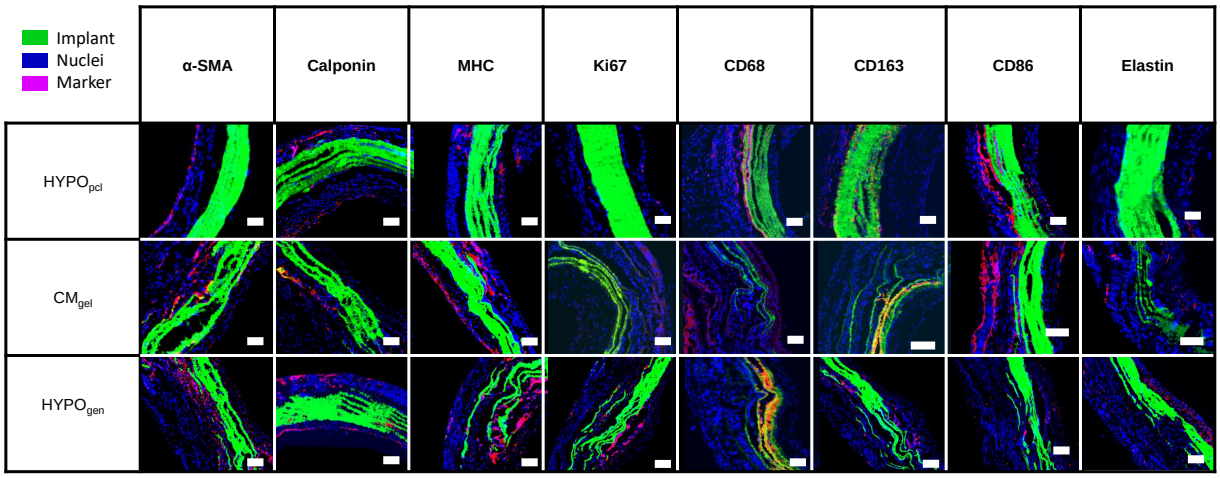

Figure 7: Representative middle cross-sectional immunofluorescence images. Green, blue, and red represent the implant, cell nuclei, and marker, respectively. The scale bar is 50 μm.

increased for HYPO$_{gen}$ vs. HYPO$_{pcl}$ in the lumen and abluminal regions, p<0.05. In the proximal location, there was increased Ki67 in the graft region for CM$_{gel}$ vs. HYPO$_{gen}$, p<0.05. The middle location of all TEVGs displayed the only statistically significant differences in macrophage content between graft type (**Figure 9**). There was an elevation in the total CD163 signal in the CM$_{gel}$ and HYPO$_{gen}$ groups vs. HYPO$_{pcl}$ group (p<0.05 for CM$_{gel}$ vs. HYPO$_{pcl}$ comparison). These results generated an increase in the total ratio of pro-remodeling macrophages to pan (CD163/CD68) in the CM$_{gel}$ and HYPO$_{gen}$ TEVGs (p<0.05). The CD86 signal was generally decreased in the HYPO$_{gen}$ with differences when compared to lumen HYPO$_{pcl}$, abluminal CM$_{gel}$, and total CM$_{gel}$ in the middle location.

Endothelialization of the constructs were evaluated using marker CD31 and only at the middle location of the construct. The percent endothelialization was found to be 48±30%, 15±10%, and 34±24% for the HYPO$_{pcl}$, CM$_{gel}$, and the HYPO$_{gen}$ TEVGs, respectively. The total collagen content had no significant differences occurring in either location however there were regional differences. The lumen and graft regions in the middle location of CM$_{gel}$ grafts had a significantly increased amount of collagen than either hypocompliant grafts, **Figure 9**. The lumen region of HYPO$_{pcl}$ grafts had more collagen than the HYPO$_{gen}$ TEVGs in the

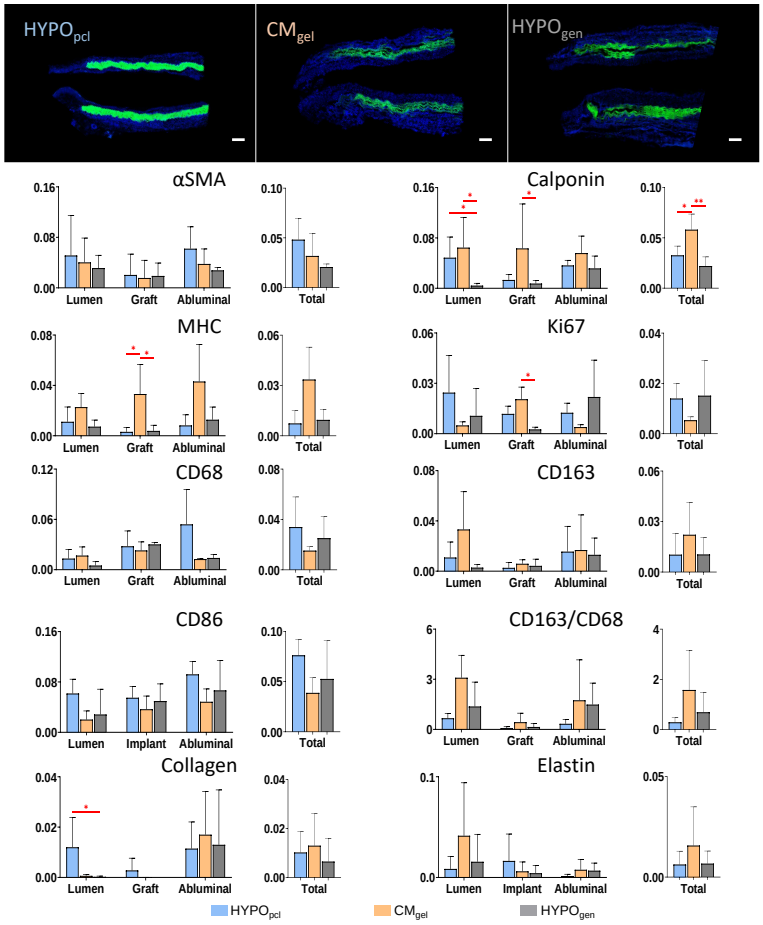

Figure 8: Representative proximal longitudinal immunofluorescence images (top). Immunohistochemistry quantification of signal in the lumen, graft, and abluminal regions for SMCs, Ki67 cells, pan macrophages (CD68), M2 (CD163), M1 (CD86), M2/Total (CD163/CD68), collagen, and elastin (bottom). SMC markers, MHC and Calponin, were relatively increased in the CM$_{gel}$ compared to the HYPO groups. The Ki67 signal was elevated in the graft region of the CM$_{gel}$ to the HYPO$_{gel}$. The collagen produced was increased in the lumen region of the HYPO$_{pcl}$ compared to CM$_{gel}$ group. $*$ = p<0.05; $**$ = p<0.01; Y axis = Pixels of Interest/Total Pixels; Scale bar is 100 μm

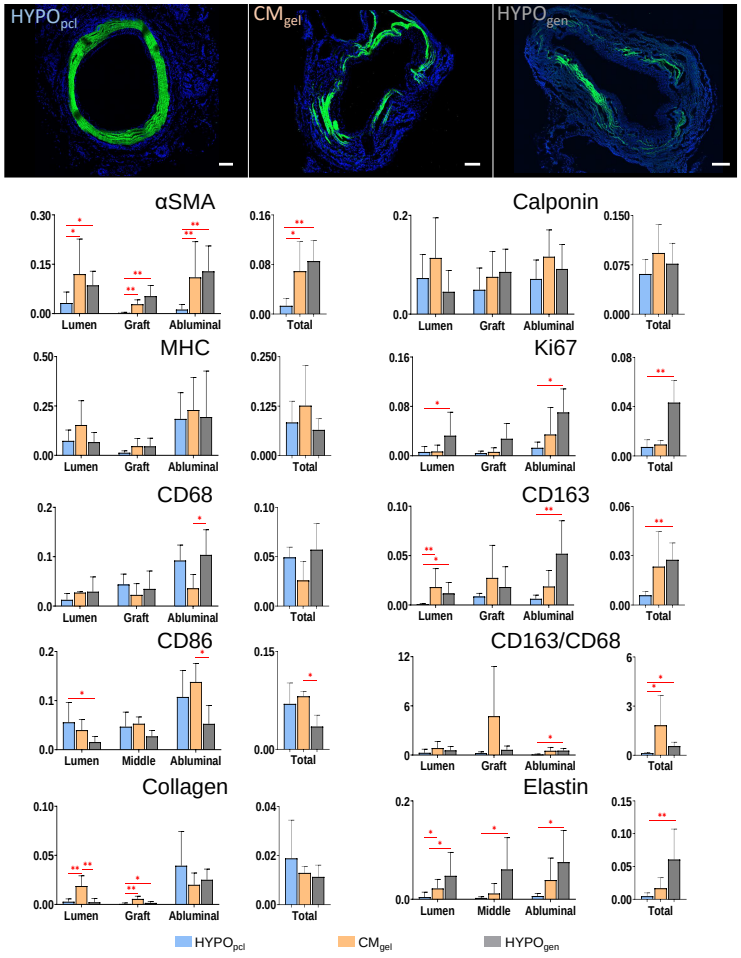

Figure 9: Representative middle cross-sectional immunofluorescence images (top). Immunohistochemistry quantification of signal in the lumen, graft, and abluminal regions for SMCs, Ki67 cells, pan macrophages (CD68), M2 (CD163), M1 (CD86), M2/Total (CD163/68), collagen, and elastin (bottom). The αSMC in the CM$_{gel}$ and HYPO$_{gen}$ TEVGs was increased compared to the HYPO$_{pcl}$ TEVGs. The Ki67, CD163, and elastin signal was elevated in the HYPO$_{gen}$ compared to HYPO$_{pcl}$ TEVG. There was a luminal increased in CD163 and elastin signal in the CM$_{gel}$ to HYPO$_{pcl}$ groups. CD68 signal was only evaluated in the abluminal region of the HYPO$_{gen}$ compared to CM$_{gel}$. The total and abluminal CD86 signal in the CM$_{gel}$ was increased compared to the HYPO$_{gen}$ and the HYPO$_{pcl}$ in the lumen was increased compared to the HYPO$_{gen}$. The ratio of CD163/CD68 was increased in the CM$_{gel}$ compared to the HYPO group. The collagen content in the lumen and graft of the CM$_{gel}$ were higher than the HYPO$_{pcl}$. $*$ = p<0.05; $**$ = p<0.01; Y axis = Pixels of Interest/Total Pixels; Scale bar is 100 μm

proximal location. The middle location generally was found to have more elastin in the high gelatin groups (CM_{gel} and $HYPO_{gen}$) with differences occurring in the $HYPO_{gen}$ to $HYPO_{pcl}$ in all regions/total and CM_{gel} to $HYPO_{pcl}$.

2.4 Discussion

Our results suggest that a TEVG computationally optimized for compliance matching displays improved acute (28 day) in-vivo graft remodeling. Overall, the high gelatin groups ($HYPO_{gen}$ & CM_{gel}) degraded more quickly in-vivo thus allowing an increased cell infiltration into the constructs. Compliance matching the TEVG lead to quicker and more mature phenotypic SMCs in the proximal location. The mechanical stimulus provided by the compliance-matched constructs also demonstrated a more favorable cellular environment with increased collagen production in the middle location in the lumen and graft regions. Hypocompliant TEVGs promote an elevated CD68 and CD163 response compared to compliance-matched grafts, suggesting a more pro-inflammatory environment. These results along with desirable improvements in SMC phenotype demonstrate that tuning the compliance of a tissue engineered vascular graft improves the in-vivo remodeling of a layered TEVG over an acute 1-month implantation period.

From our immunohistochemistry results and the literature, compliance has consistently been shown to affect SMC phenotype [56, 57]. In this study, there were increases in CAL (mid-differentiated) and elevated trends in MHC signal (late differentiated) in the proximal location of our compliance-matched grafts. This suggests that the mechanical environment provided by compliance-matched grafts encourages SMCs to move towards a more contractile phenotype earlier. Past in-vitro work by Bingcheng et al. is in agreement with our work as they showed similar changes in SMC phenotype as the compliance of their electrospun grafts increased [57]. Additional time points and explant functional testing (e.g., vasoreactivity) will be necessary to determine if the observed results here continue to promote a more functional vessel as our TEVG continues to be replaced by native host cells and extracellular matrix.

Likely due to our limited implantation time point, the middle of our graft showed slower cell infiltration and a less differentiated SMC phenotype. This is consistent with the presence of an increased number of αSMA positive cells in this region [58]. These results suggest that gelatin is ideal for fast degradation and cellular infiltration which is similar to what other groups have shown in-vitro [59, 60]. For the rat model, a higher gelatin content graft appears to be ideal for promoting increased cell infiltration and migration, but as you move to other animals there may be a need to balance this aspect. Generally, other animal models may require varying lengths of time for cellularization and therefore may need a slower degrading graft. Finding the ideal balance between the degradation of the scaffold and cellular infiltration will be vital for a particular animal model. For example, a longer implant in a sheep model will take more time to cellularize than a rat implant and this should be taken into account. It should be noted that increasing the gelatin content beyond what was used in this manuscript (a hypercompliant group) led to an even lower suture retention than $HYPO_{gen}$ & CM_{gel}, **Figure 4**, and an inability to implant the resulting graft. The $HYPO_{gen}$ and CM_{gel} were found to be slightly more challenging to implant than the $HYPO_{pcl}$ grafts as a result of the lower suture strength.

SMC phenotype and functional behavior is also influenced by the local mechanical environment and composition of the extracellular matrix surrounding these cells. Several groups have shown that SMCs tend to migrate faster on surface coatings with stiffer substrates [61, 62]. Substrate stiffness has also been cited as being able to change SMCs from a contractile to a more proliferative phenotype[63]. We initially attributed our SMC results in the $HYPO_{gen}$ group in the middle location to substrate stiffness. However, the $HYPO_{gen}$ group had more highly proliferative cells (Ki67) in the total region than both low genipin concentration groups ($HYPO_{pcl}$ & CM_{gel}, p=0.09), suggesting that increased genipin concentration may be the cause rather than compliance. This increase in highly proliferative cells suggests that the 20x fold increase (22 to 440mM) of genipin between groups could be potentially disruptive in-vivo. Genipin has been cited as a less cytotoxic agent than glutaraldehyde in the literature, however elevated genipin media concentration (>10mM) can prevent cell proliferation and promote cell death [64, 65].

While our TEVGs were fabricated with genipin concentrations near or exceeding these

levels, our preliminary data suggests that the degradation products of our graft have little to no affect on RSMC growth, **Figure 4**. This is likely due to the fact that our grafts were thoroughly washed prior to implantation and as such do not expose the cells to these higher concentrations of genipin. It also should be noted that we did see an increase of Ki67 signal in the proximal graft region for the CM_{gel} grafts compared to $HYPO_{gen}$, however the specific cause is unclear and will require future investigation.

General SMC alignment and distribution at either location was not able to be evaluated due to the acute nature of the study, however our histological images show a grouping of SMCs which is encouraging. We would expect to see increased TEVG remodeling and SMC alignment at longer implantation time points and hope to evaluate this in the future studies [66, 67, 68].

Macrophage infiltration and proliferation in the TEVG are vital to healthy graft remodeling and this varied in the proximal and middle location. Again, we saw signs suggesting early cellular infiltration in the proximal anastomosis and generalized macrophage infiltration occurring in the middle location. Specifically, there was a decrease in CD68 macrophages in the abluminal region for compliance-matched constructs compared to $HYPO_{gen}$. For the higher gelatin grafts ($HYPO_{gen}$ & CM_{gel}) there was an increasing trend of total CD163 which may suggest that the presence of gelatin leads to a more pro-ECM maintenance and healing response. This M2 response is generally correlated with extracellular matrix formation and collagen production, which we found to be significantly higher in the compliance-matched group in the middle location of in the lumen and graft regions (**Figure 9**). On the other hand, the stiff constructs generally showed a decreased trend in CD163/CD68 compared to compliance-matched grafts suggesting local mechanical response could be vital to tissue regeneration. This also demonstrated that matching compliance of the vessel can provide a favorable environment for extracellular matrix formation. Looking more specifically at M1 macrophage markers (CD86), the $HYPO_{gen}$ group showed a general reduction in signal compared to $HYPO_{pcl}$ and CM_{gel}. These results suggest that higher genipin concentrations could have an effect on reducing the M1 macrophage population. Genipin, specifically, has been shown to reduce M1 macrophages in liver crosslinked samples when compared to glutaraldehyde [69]. For CD68, it was generally increased in grafts with high PCL concen-

trations (similar to our $HYPO_{pcl}$ group) [40, 70]. Here we demonstrate that similar levels of CD68 and CD163 are elicited in grafts with half as much PCL, suggesting that the local biomechanical environment may also contribute to this response.

Another important factor in the formation of a functional TEVG is the replacement of our graft materials with the production of extracellular matrix, in particular collagen and elastin. For collagen at the one month time point, the CM_{gel} grafts generally had an elevated signal in the middle location of the lumen and graft regions compared to the HYPO grafts. These results suggest that compliance matching a graft can promote constructive in-vivo remodeling. One unexpected result was the increase in collagen in the lumen of the proximal location of the $HYPO_{pcl}$ grafts. The cause and implications of this result, along with the general elevation of M1 macrophages in that area seems to suggest the start of intimal hyperplasia [71, 72] but, this results will need to be studied in more depth at longer time points to confirm. For elastin, CM_{gel} and $HYPO_{gen}$ both had elevated signal in the middle location of our grafts. These results suggest that higher gelatin content is more favorable for elastin formation than PCL. Finding the right balance between the production of collagen and elastin as our graft degrades will be important in maintaining the compliance of our graft as it continues to degrade over longer time points. Future research will be needed to determine the optimal rates.

An interesting trend from our study was the endothelialization of our grafts. We found that both stiff grafts had an increased percentage of endothelialization compared to the compliance-matched graft. This indicates that endothelial cells migrated more quickly onto our hypocompliant grafts [58], which is consistent with literature indicating cells migrate further and faster on stiffer substrates [73, 74]. This finding is contrary to our initial hypothesis (that compliance matching may promote endothelialization), however this result can be leveraged in future graft designs. For example, a graft with a very thin but stiff inner layer could help promote early endothelialization while still maintaining optimal compliance. In general, percent endothelialization in our study was similar to the literature at one month, as complete coverage of grafts in the literature typically occurs around 3 months post implantation [75, 68, 70, 76].

The primary goal of this study was to evaluate the influence of compliance and remod-

eling on TEVG design. Our ultrasound data (**Figure 5**) showed that the CM_{gel} constructs stayed compliance-matched throughout the time course of the study. Maintaining compliance demonstrated that the mechanical stimulus provided by the environment on cellular infiltration was maintained and this has not been previously shown using a rat model. Most TEVGs tend to be hypocompliant before implantation and maintain their compliance in-vivo, however some groups have shown that compliance can vary over the course of remodeling. Wu and Allen have demonstrated that a stiff or hypocompliant graft can remodel in-vivo to increase compliance by 3 months and maintain compliance over time but still showed a decreased stiffness trend compared to rat aorta [77, 66]. Another group also demonstrated that a Poly(l-lactide-co-ϵ-caprolactone) TEVG increased in compliance for up to 12 months [36]. From the quantification of cellular markers and extracellular matrix formation, these previous studies demonstrate that graft degradation/remodeling can occur and transition a degrading graft towards a functional vessel. In this study, the gelatin grafts ($HYPO_{gen}$ & CM_{gel}) also had a high percent of degradation and evidence of remodeling (collagen content), however a unique feature of our graphs was their ability to maintain compliance throughout the study and increase cellular infiltration in the gelatin groups. Looking more specifically at degradation and cellular infiltration, our group has demonstrated that cellular infiltration and degradation can be varied depending on composition/cross-linking and this is useful for translating the results into larger animal models where varied cellular infiltration rates will be necessary.

The patency rate of our $HYPO_{pcl}$, CM_{gel}, and $HYPO_{gen}$ grafts were 6/7, 5/7, and 6/7, respectively, leading to an overall patency rate of 81%. This is similar to several studies in the literature [39, 75, 78, 79, 80]. For example, Wu et al. has shown a similar patency rate in their acellular TEVG with 17/21 remaining patent out to 3 months [77]. Nieponice et al. showed lower patency rates for poly-(ester urethane) thermally-induced phase separation scaffolds with 53% at 8 weeks and Pektok showed 100% patency through 24 weeks using a PCL electrospun scaffold [81, 82]. While these results are encouraging, patency of our graft could be further improved in the future with the incorporation of cells and/or surface coating to reduce thrombogenicity [83].

The blood velocity results of our TEVGs were found to be relatively consistent with the

current literature values, around 900 mm/s [78]. There were some graft dilations in $HYPO_{gen}$ group at 2 and 4 weeks,(**Figure 5**), and these increases could be the onset of graft failure or aneurysm in future time points. An unexpected result was the lack of a decrease in blood velocity when comparing the HYPO to CM_{gel} groups. This may be attributed to the short implant period and the dilations seen in the a few of the $HYPO_{gen}$ grafts.

There are several limitations in this study. Rat aortic interpositional implantations offer significant advantages including their use as a relatively high throughput model. However, this model is limited as it has major differences in the hemodynamics, regenerative ability, and physiology in comparison to target vessels in most human vascular diseases. In order to minimize some of these limitations, other groups have used the rat carotid which has more clinically relevant flow and a smaller diameter, but may still suffer from some physiological differences [40]. Future implantations should consider utilization of an animal model with a hemodynamic flow environment more similar to that in the target human vessel. The second major limitation of this study was the acute one-month implantation period which restricts the conclusions that can be made on long-term cellular infiltration and vessel functionality. The earlier time point used here did however serve to identify differences in the acute remodeling of our grafts. Our group is currently planning to investigate how the results and conclusions presented here are altered in longer (3 to 12 months) implantation periods. Another limitation was the range of materials selected to tune the compliance and thickness of our graft to that of a rat aorta. These constraints limited the ability to increase suture retention and burst pressure, as seen in the CM_{gel} and $HYPO_{pcl}$ groups. Selecting different materials or increasing the thickness of the implant could help prevent these problems in the future. Finally, it should be noted that while compliance was controlled by manipulating both graft composition and genipin concentration, this approach does present a confounding factor within each group comparison. The authors of this manuscript want to emphasize that conclusions made about compliance should only be made when both HYPO groups have similar results and the compliance-matched group, CM_{gel}, differs significantly from these groups. If the reader is only comparing the CM_{gel} and $HYPO_{pcl}$ groups this illuminates the effect of not only compliance but also gelatin concentration. Similarly, the effect of compliance on differences between the CM_{gel} group and $HYPO_{gen}$ groups is confounded by

genipin concentration. Future studies will need to address and mitigate these confounding factors to help further elucidate the role compliance has in TEVG design.

In this study, the approach used to modify compliance was the composition and crosslinking of the TEVG, however there are alternative approaches to accomplish this same goal. Increasing crosslinking concentration is a common method to decrease graft compliance as demonstrated in our study and by that of the Abbott et al. group who altered the concentrations of glutaraldehyde [33] during crosslinking. Our group has used a similar approach in the past [45], however have since moved away from this approach due to the cytotoxic potential of glutaraldehyde in-vivo [21, 84, 85]. Other groups have shifted towards manipulating graft compositional changes to vary compliance [41, 86]. Nezarati el al. created synthetic polymer grafts with varying thickness, tortuosity, and fiber fusions that were able to exceed the compliance of the human saphenous vein [41]. Another group modified the outer PCL sheath thickness which created a TEVG with tunable compliance [86]. While several researchers have successfully tuned the compliance of TEVGs, none have been able to match the thickness and compliance of the target vessel simultaneously. In general, most of the afore mentioned TEVGs and other researchers in the literature are at least several hundreds of microns thicker than that of rat aorta (approx. 80 μm) which could limit cellular infiltration, transport, and cellular migration. Soletti et al. showed promise with their graft thickness, however, their grafts were significantly less compliant than rat aorta [81]. Our unique method allowed us to create a compliance-matched TEVG that has a similar thickness to rat aorta with a unique and biomimetic multi-layer design which can be modified to more closely resemble the native vessel. This multi-layer approach could also be tuned to include naturally occurring biopolymers such as elastin and collagen.

2.5 Conclusion

This study is the first to assess the functional performance of a multi-layered TEVG that has been compliance-matched using a computational optimization approach. The mechanically optimized graft is acutely remodeled to remain compliance-matched in-vivo over

a 1-month period. The CM_{gel} grafts also demonstrated an increase in collagen production within the implant that may emanate from a more desirable macrophage and SMC response. These results need to be further explored in future studies that thoroughly assess graft vasoreactivity, graft degradation, and ECM production in graft explants at longer term explant periods [87]. We believe the results of this study demonstrate the importance of careful control of graft design and how it may influence the in-vivo remodeling and functional performance of biodegradable TEVGs.

The results of this study support the hypothesis that the compliance of a vascular implant effect the remodeling of a TEVG and demonstrates its importance. Specifically, compliance matching a vascular graft increases cellular infiltration and positive cellular remodeling of the TEVG. In the future, vascular graft designers may use this knowledge as a stepping stone to help design a better TEVG.

3.0 Modulating TGFβ2 Elution Alters the Acute Remodeling of a Compliance-Matched Tissue Engineered Vascular Graft

The goal of this aim was to alter the concentration of TGFβ2 (0 ng/mg, 10 ng/mg, and 100 ng/mg) eluting TEVGs which were either compliance-matched or hypocompliant and were used to assess cellular infiltration, migration, and proliferation over an acute 5-day period. The TEVG was either tuned to be either compliance-matched (CM_{gel}) or hypocompliant ($HYPO_{pcl}$) to rat aorta using our integrated computation/experimental approach, loaded with TGFβ2, crosslinked with genipin [28], and then implanted into the aorta of Sprague Dawley rats for 5 days. Preliminary cellular infiltration was assessed using ultrasound and the host response was quantified from explant histology.

3.1 Introduction

Designing a functional TEVG requires several key factors including matching the compliance of the graft to the native vasculature (aim 1), the recruitment of smooth muscle cells (SMC) into the implant, desirable scaffold composition for cellular infiltration, and drug delivery for cellular recruitment and phenotypic control. The compliance of the vascular graft has been shown to have an effect on vascular smooth muscle cell phenotype, inflammatory response, and overall patency of the TEVG, aim 1 [32, 57, 33]. Moreover, stiff (hypocompliant) grafts change the hemodynamic environment of the vessel that can result in loss of patency a characteristic often overlooked in TEVG design [42, 43, 44, 34]. SMCs are the major muscular component of the vessel responsible for extracellular matrix (ECM) production and the regulation of vascular tone. Controlling the composition of the TEVG also offers the unique ability to encourage SMC manipulation through the integration of biomolecules into the scaffold. One factor of particular interest is transforming growth factor beta 2 (TGFβ2), which has been shown to deferentially modulate SMC phenotype as a function of concentration in vitro [29]. This growth factor is a pleiotropic cytokine that regulates cell

cycle, cell differentiation, cell growth, cell death, and ECM deposition/ organization [88, 89]. On a macroscopic scale, TGFβ2 has also been shown to have a role in ECM remodeling in vascular, cardiac, and embryonic development [90, 91, 92]. Focusing more on vascular disease, the TGFβ family has been shown to be atheroprotective and atherogenic depending on concentration [29, 93]. In our laboratory we have shown that SMCs can be recruited by eluting a low TGFβ2 concentration (0.1 ng/mg) to promote cellular migration, while higher concentrations can arrest cellular proliferation/migration and promote collagen production [29]. This low TGFβ2 concentration in vitro has also shown the ability to promote SMC proliferation/migration on a TEVG scaffold after 5 days of incubation [27]. Thus, incorporating TGFβ2 into a TEVG could promote earlier SMC proliferation/migration in the graft in vivo. In this aim, the effects of TGFβ2 concentration on TEVG will be evaluated and discussed.

3.2 Methods

3.2.1 Optimization Routine for TEVG Formulation

An overview of the study is provided in **Figure 10**. compliance-matched and hypocompliant TEVGs were formulated using our integrated computational/experimental approach that predicts alternating layer thickness and gelatin:PCL (G:P) ratio of our graft [52, 28]. Briefly, the material constants were collected for a Fung-type constitutive model based on biaxial mechanical testing of 20G:80P, 50G:50P, and 80G:20P tubular constructs using our microbiaxial optomechanical device (MOD) [45, 46, 47, 48, 49, 50, 51]. These properties were used in a four-node, reduced-integration, axisymmetric finite element model in Abaqus (Dassault Systemes Simulia, France) in combination with an optimization scheme in Matlab (MathWorks Inc, USA). The model's open design parameters were G:P ratio and the thickness of each of the paired layers. The constrained parameters for each construct were inner diameter, number of paired layers, and total thickness. The output of this approach created an alternating bilayered construct consisting of 12 total layers that was compliance-

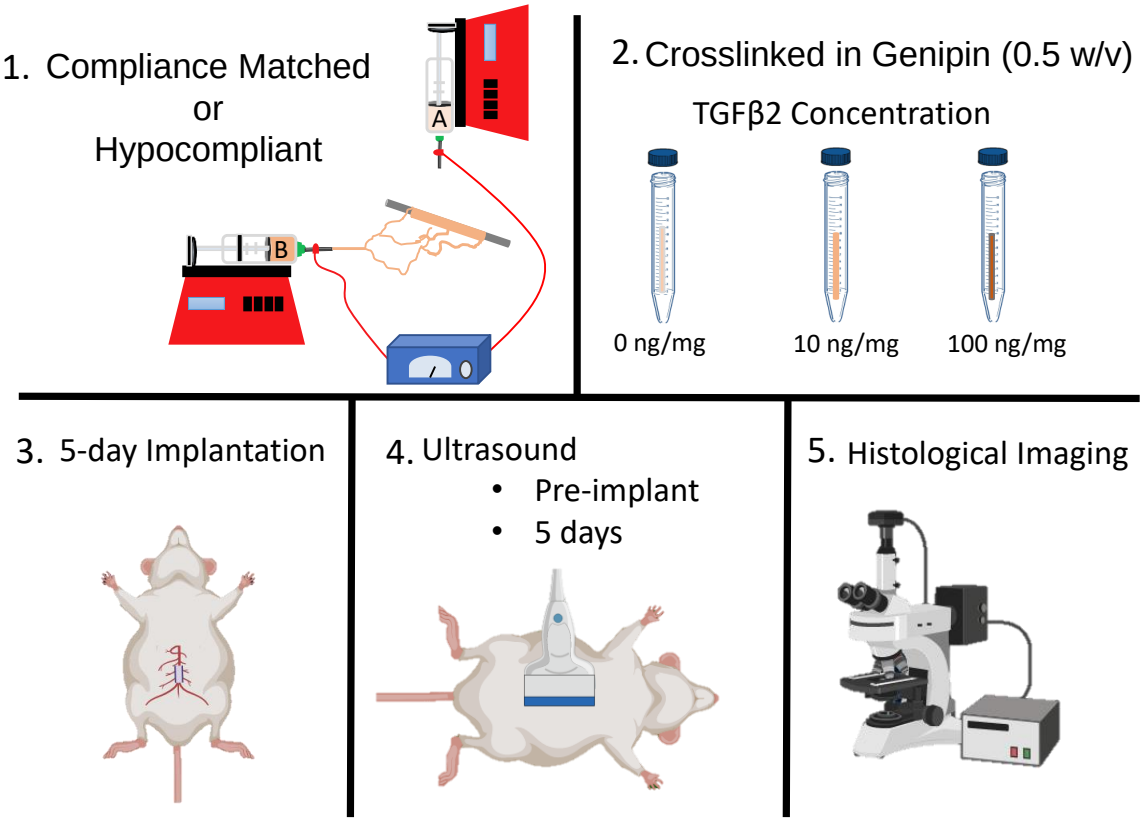

Figure 10: Overview of TGFβ2 study. 1. Compliance-matched and hypocompliant constructs were fabricated using a biaxial electrospun method that incorporated TGFβ2 concentrations at 0, 10, 100 ng/mg. 2. Constructs were crosslinked in 0.5% w/v genipin for 24 hrs at 37°C. 3. The TEVGs (n=3 for each group) were implanted in the abdominal aorta of a Sprague Dawley rat for 5 days. 4. Before surgery and 5 days after implantation the TEVG was imaged using ultrasound. 5. Histological markers were used to evaluate host response.

matched and hypocompliant to rat aortic values with approximately sixty-five and thirty percent gelatin, respectively. The TEVG formulations are found in **Table 2**.

3.2.2 Graft Material and Fabrication

The constructs were fabricated using an biaxail syringe setup with IME electrospinning device that included a climate-controlled chamber and gas shield to prevent buildup (Waalre, Netherlands). For this process, gelatin extracted from porcine skin (Sigma-Aldrich) and PCL with a molecular weight 80,000 (Sigma-Aldrich, St. Louis, MO) were dissolved in 1,1,1,3,3,3-hexafluoro-2-propanol (HFP) (Sigma-Aldrich) to create a 10% w/v solution. The polymeric formulations for biaxial electrospinning were 75:25 & 50:50 G:P and 20:80 & 35:65 G:P for the compliance-matched (CM_{gel}) and hypocompliant constructs ($HYPO_{pcl}$), respectively. The polymeric solutions were loaded into 5ml BD syringes (BD Franklin Lakes, NJ) and lyophilized recombinant human TGFβ2 (R&D systems) was reconstituted with 4mM HCL containing 1mg/ml bovine serum albumin (BSA) (SigmaAldrich, USA). TGFβ2 was added to each syringe based on the ratio of total gelatin percentage of the two formulations. For example, one construct layer had a syringe filled with a 75% and the other a 50% gelatin concentration, thus this ratio of 3:2 was used as the amount of TGFβ2 mass to assign to each syringe. The polymer blends and TGFβ2 were mixed to create a final TGFβ2 mass of 0, 10, or 100 ng per mg of scaffold [29].

Once mixed for 24 hours, the electrospinning solutions were both loaded onto separate computer-controlled syringe pumps and connected to IME electrospinning device through 1 mm PTFE tubing. The electrospinning parameters were as follows: working distance of 10 cm, dispense rate of 50 μL/min (both syringes), and 15-kV voltage. Constructs were spun onto a 1.1 mm diameter steel rod rotating at 300 mm/s with a tip translation of 300 m/s. The climate and humidity were set to 25°C and 30%, respectively. Before creating the construct, each syringe pump was primed and checked for solution extrusion. The higher gelatin formulation was spun from the vertical nozzle to help prevent buildup on the tip. Each layer was extruded sequentially which took about 4 minutes per layer to allow dissipation of the line pressure. Following the completion of the electronspinning process, the constructs were soaked and shaken in 0.5% (w/v) genipin (Wako Chemicals USA Inc, USA) in 200 proof ethanol for 24 hrs at 37°C to crosslink gelatin [28]. Following crosslinking, the constructs were then rinsed with 200 proof ethanol and implanted within 24 hours.

3.2.3 Rat Aortic Implantation

The TEVGs were implanted into the abdominal aorta of 8-week-old Sprague Dawley rats for 5 days. The compliance-matched and hypocompliant TEVG contained 0, 10, or 100 ng/mg TGFβ2 concentration with n=3 in each group for a total of 18 animals (males and females distributed within each group). The interpositional abdominal aortic surgical procedure followed closely the protocol described by Niepionce [80] and recently used by our group [32]. To begin the surgery, each rat was anesthetized with isoflurane (3% for induction and 1% for maintenance) for the duration of the study. Next, the fur was removed by using Nair^{TM} with a paper towel and a 3-4 cm incision with a No. 10 scalpel was made on the medial abdominal wall. The small intestines and cecum were removed from the abdominal cavity and covered with heparin soaked gauze to prevent dehydration and clotting. The aorta was isolated (1 cm above the bifurcation) from connective tissue, side branches were ligated and transected, and two 30 g clips were applied to the bifurcation and ilolumbar artery to arrest blood flow. The aorta was transected, the lumen of the vessel was irrigated by saline, and the anastomosis was initiated at the proximal region of the vessel with stay sutures using a 10-0 nylon placed at the 3 and 9 o'clock positions. Three or four stitches were added to the anterior wall and then the vessel was rotated 180^o clockwise with a similar amount of stitches added to the posterior wall. A similar procedure was performed on the distal anastomosis. Before the last suture was placed, the lumen of the implant was irrigated with saline. The clips were then removed and the vessel was assessed for patency using a perfusion test. If bleeding occurred, pressure was applied to the suture line until bleeding stopped. On occasion, an extra suture would be placed on a distal suture if bleeding persisted. In general, each anastomosis had around 7-10 stitches per end. After completion of the anastomosis, the small intestines and cecum were returned to the abdominal cavity, the rectus abdominis was closed using an interrupted 4-0 absorbable polyfilament suture, and skin was stapled closed.

Upon completion of the surgery, each rat received two daily intramuscular injections of 0.5mg/kg buprenorphine and 100mg/kg cefuroxime for the first three days to minimize pain and prevent bacterial infections, respectively. All solid medication was pulverized, mixed

Table 2: Polymeric formulations, layer thickness, crosslinking concentrations, and TGFβ2 concentration (ng/mg).

Group	L1 G:PCL	L2 G:PCL	Layer Thickness (μm)				Genipin	Sample Size		
			L1	L2	Repeats	Total	(w/v)	0	10	100
CM	75:25	50:50	8	5	6	78	0.5	3	3	3
Hypo	20:80	35:65	8	5	6	78	0.5	3	3	3

with jelly, put into a small ice cream cone, and fed to the rat. Inflammation was minimized by feeding the rat carprofen (5mg/kg) at 24 and 48 hrs post operatively. Aspirin (pain reliever) and dipyridamole (antiplatelet agent) were also fed to the rat at a concentration of 200 mg/kg and 250 mg/kg for duration of the study. After 5 days, the graft was recovered by euthanizing the rat and fixed in a 4% paraformaldehyde solution in PBS (Thermo Fisher Scientific, Waltham, MA).

3.2.4 Measurements and Quantification of Outcomes

3.2.4.1 In Vivo Ultrasound

Graft patency, diameter, compliance, and maximum blood velocity were collected using high frequency ultrasound (VEVO 2100 FUJIFILM VisualSonics Inc, Canada) with a MS400 30 MHz probe. The rats were imaged for up to one week before surgery and 5 days post implantation. Ultrasound data was collected by anesthetizing the rat with isoflurane (3% for induction and 1% for maintenance), removing the fur with Nair Hair Removal (Church & Dwight), and imaging the abdominal aorta cross-sectionally and longitudinally. In general, cross sectional imaging was used for identifying the aorta and patency, while diameter/compliance measurements and velocity were calculated longitudinally. Patency was determined by using ultrasound to observe flow through the entirety of the implant. All ultrasound measurements and calculations were determined using the Vevo Lab software

version 1.7.1. In vivo rat compliance was calculated from the inner minimum and maximum (reference to human) longitudinal diameters:

$$Compliance = \frac{(ID_{120} - ID_{70})/ID_{70}}{50\text{mmHg}}. \tag{3.1}$$

The 50 mmhg in the denominator of the compliance equation was constant for all animals and represented the difference in theoretical pressure. The inner minimum and maximum diameters were then averaged to determine the diameter of the vessel. Using Doppler ultrasound, the maximum velocity of 3 waveforms per rat was used and adjusted for probe angle [55]. All ultrasound data was checked for normality using a Shapiro–Wilk test and compared to healthy rat aorta using a one-way ANOVA with Tukey post hoc testing. The length of the construct was assessed using a one-way ANOVA with a Tukey post hoc analysis.

3.2.4.2 Immunohistochemistry and Fluorescent Imaging

All TEVGs were evaluated for cellular markers and construct remodeling. Each explant was cut in half, separated into proximal and distal portions, frozen in O.C.T. medium, and cut into 10 μm thick sections using a Microm HM550 cryostat microtome. The proximal portion of the sample was cut longitudinally and the distal part was cut cross-sectionally at the mid-graft location.

For immunohistochemistry, samples were rehydrated in PBS and then soaked in 1% sodium dodecyl sulfate (Sigma-Aldrich, St. Louis, MO) in PBS for 15 minutes. The samples were next permeabilized in 0.3% triton X-100 (Sigma-Aldrich) for 15 minutes and blocked with 0.5% bovine serum albumin (Sigma-Aldrich), 0.3 M glycine (Thermo Fisher Scientific), and 20% goat serum (Thermo Fisher Scientific) for one hour. Following blocking, all samples were incubated with primary antibodies over night at 4°C. α-Smooth muscle actin (αSMA), calponin (CAL), and smooth muscle myosin heavy chain (MHC) were used to detect smooth muscle cells. Highly proliferative cells were labeled with Ki67 and the samples were also labeled for elastin. The inflammatory response was determined using CD68, CD86 and CD163 for pan, M1, and M2 macrophage phenotypes, respectively. All primary antibodies were used at a ratio of 1:100 and purchased from Abcam. After incubation and washing,

the samples were incubated for 1 hour at room temperature with Alexa Fluor 488 Goat Anti-Rabbit IgG (Abcam, 1:1000) except for αSMA which was incubated with Alexa Fluor 488 Donkey anti-goat IgG (Abcam, 1:1000). Each sample was washed and counterstained with DAPI mounting medium (Abcam).

Cellular markers were evaluated using using a Nikon 90i Eclipse fluorescence microscope. Each section was imaged entirely using DAPI (excitation at 359 nm; emission at 461), FITC (excitation at 495 nm; emission at 519 nm), and Cy5 (excitation at 647; emission at 665) emission channels using a Nikon Plan Apo 10x/0.45 objective. Cell nuclei, implant, and marker were identified in DAPI, Cy5 (autofluorescence from genipin), and FITC channel, respectively. The exposure time for the FITC channel was consistent between all samples of the same marker to quantitatively assess difference between samples.

3.2.4.3 Multiphoton Imaging

Collagen was imaged using second harmonic generation using the Pitt Advanced Intravital Microscope at the University of Pittsburgh for the cross-sectionally and longitudinally sectioned samples. For this setup, an Olympus BX51 upright scanning microscope (Olympus, Tokyo, Japan) was coupled into a 120-fs tunable pulsed laser (INSIGHT DS+DUAL, Newport, Irving CA) and Olympus XLUMPLFL 20x water emersion objective (NA 0.9). Collagen fibers were imaged at 780 nm and collected with a bandpass filter 377/50 nm with a power 118-152 mW using second harmonic generation. DAPI and autofluorescence was also imaged at 780 nm with a power of 25-31 mW and collected with 525/50 nm and 620/60 nm bandpass filter, respectively. The signal was collected over multiple 499 x 499 μm fields of view with a 5 μm z-step-size through the entire thickness of the sample. Mosaic images of each channel (377, 525, and 620 nm) were converted into maximum intensity projections and used for image processing.

For processing, the images were used to calculate abluminal number of cells, construct thickness, and total collagen. The construct thickness was measured for each explant and compared using a one-way ANOVA. The cells inside the construct and in the abluminal region were calculated using the ImageJ (Fiji) particle function. Percent collagen in the

samples was calculated the same as the antibody image processing discussed in the section below (**Section 3.2.4.4**).

3.2.4.4 Image Processing

Fluorescent signal was collected using a Nikon 90i Eclipse fluorescence microscope in three channels DAPI, FITC, and Cy5 which were faux colored with blue for cell nuclei channel, green for implant channel (green), and red for the antibody or collagen channel, respectively. All images were processed using Matlab to determine antibody signal differences between each group. FITC signal was binarized to remove background noise and identify the pixels of interest (POI). The amount of signal per sample was calculated by dividing the pixels of interest by the total number of pixels (POI/TP) in a certain area. For collagen specifically, the sample had a high amount of noise which also required the collagen image to be despeckled. All marker calculations were done for the proximal and middle sections. The markers for each group 0, 10, 100 ng/mg were checked for normality and compared using a one-way ANOVA with Tukey posthoc testing.

3.3 Results

3.3.1 Construct Characterization

Previous work quantified the compliance-matched and hypocompliant TEVG burst pressure, suture retention, and compliance which were 504±164 & 1435±107 mmHg , 11±2 & 43.5±15 g, and matched compliance & twice as stiff as rat aorta, respectively [32]. The overall release profile of TGFβ2 from the compliance-matched and hypocompliant construct were evaluated in Ardila et al. with around 1 - 1.5 and 0.05 % of the total growth factor released from each construct by 5 days [27].

For the surgery, no complications or adverse events occurred with all animals surviving the duration of the study. Each surgery generally lasted around one and a half hours with the anastomosis time taking approximately 50 minutes. The average implant length for

the compliance-matched constructs were 0, 10, and 100 ng/mg were 7.7±0.7, 6.9±0.2, and 6.6±0.8 mm, respectively, with no difference between groups. The hypocompliant TEVGs average length for 0, 10, and 100 ng/mg were 6±0.5, 5.7±0.6, and 6.4±0.3 mm, respectively, with no difference between groups. The 100 ng/mg compliance-matched construct thickness was found to be thinner than the 10 ng/mg construct (59±6 vs. 74±4 μm, p = 0.04) with no difference in relation to the 0 ng/mg construct (71±4 μm), **Figure 12**. The thickness of hypocompliant constructs were all similar.

3.3.2 Ultrasound

Ultrasound imaging confirmed patency in all groups throughout the duration of the study. The compliance-matched constructs were found to decrease in compliance as the concentration of TGFβ2 increased. Specifically, the 100 ng/mg group was considerably stiffer than the native rat aorta, 17±2x10^{-4} (0 ng/mg) to 11±1x10^{-4} mmHg^{-1} (100 ng/mg). The diameter and maximum velocity for all compliance-matched groups did not differ from native rat aorta tissue. In general, the average implant diameter and velocity was around 1000 μm and 700 mm/s, respectively. These results can be found in **Figure 11**.

The compliance of the hypocompliant grafts for 0, 10, 100 ng/mg were 8.7±3x10^{-4}, 6.3±1x10^{-4}, 8±2x10^{-4} mmHg^{-1} with each graft being significantly stiffer than native rat aorta, p<0.0001 for all comparisons. The diameter and velocity of the hypocompliant TEVGs were similar to that of native rat aorta (**Figure 11**).

3.3.3 Multiphoton Imaging

Multiphoton images representing the hypocompliant (blue) and compliance (orange) TEVGs for the 0, 10, 100 TGFβ2 ng/mg 5 day explant groups are shown in **Figure 12** with green being the construct and blue cell nuclei. The overall cell count (lumen, implant, and abluminal) for the compliance-matched implant was generally similar between the 0 and 100 ng/mg groups with the least amount of cells in the 10 ng/mg group. Cellular infiltration decreased in the compliance-matched TEVG with increasing concentrations of TGFβ2, 0 vs. 100 ng/mg (3600±1700 vs. 770±300 cells, p<0.05). TGFβ2 had the opposite effect on the

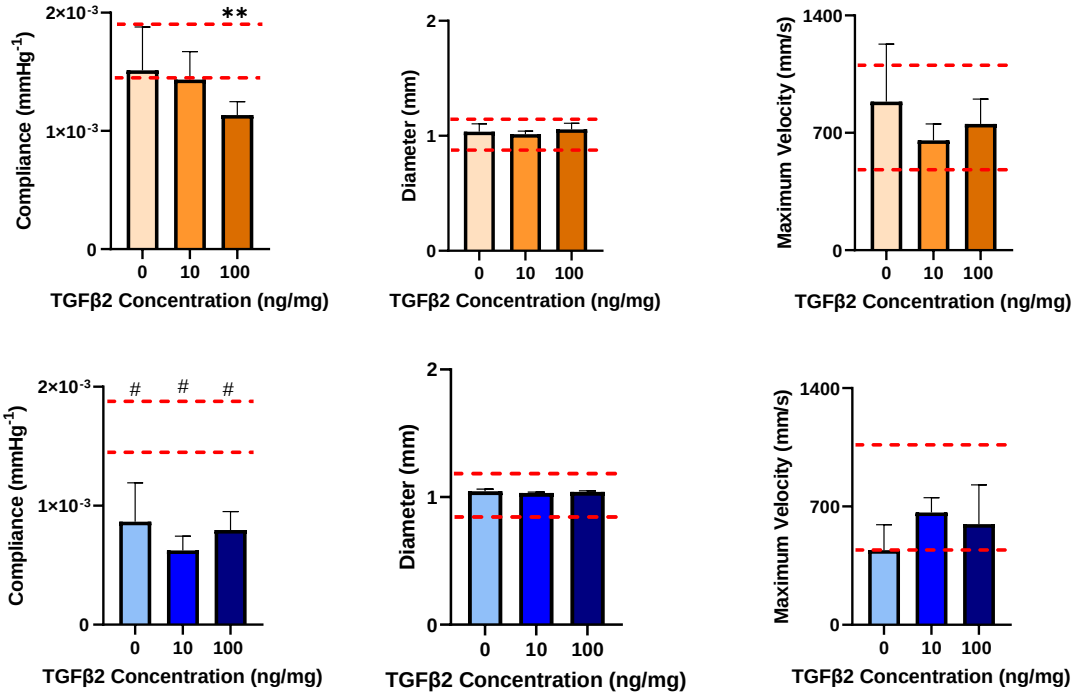

Figure 11: Compliance, diameter, and maximum velocity of 0, 10, 100 ng/mg of constructs. Orange and blue bars indicate compliance-matched and hypocompliant TEVG implants, respectively. The red dashed lines represent rat aorta. The compliance matched constructs became less compliant as the concentration of TGFβ2 increase, while the hypocompliant construct remained stiff over all concentration. The diameter and maximum velocity remained similar to rat aorta for all groups. $**$ = p<0.01 and # = p<0.0001 in reference to rat aorta

abluminal cell count in compliance-matched TEVGs with the 100 ng/mg construct having the most cells compared to the 10 ng/mg construct (6820±1670 vs. 200±140 cells, p<0.05). For the hypocompliant TEVGs, cellular infiltration into the construct and abluminal region were found to be similar between all constructs.

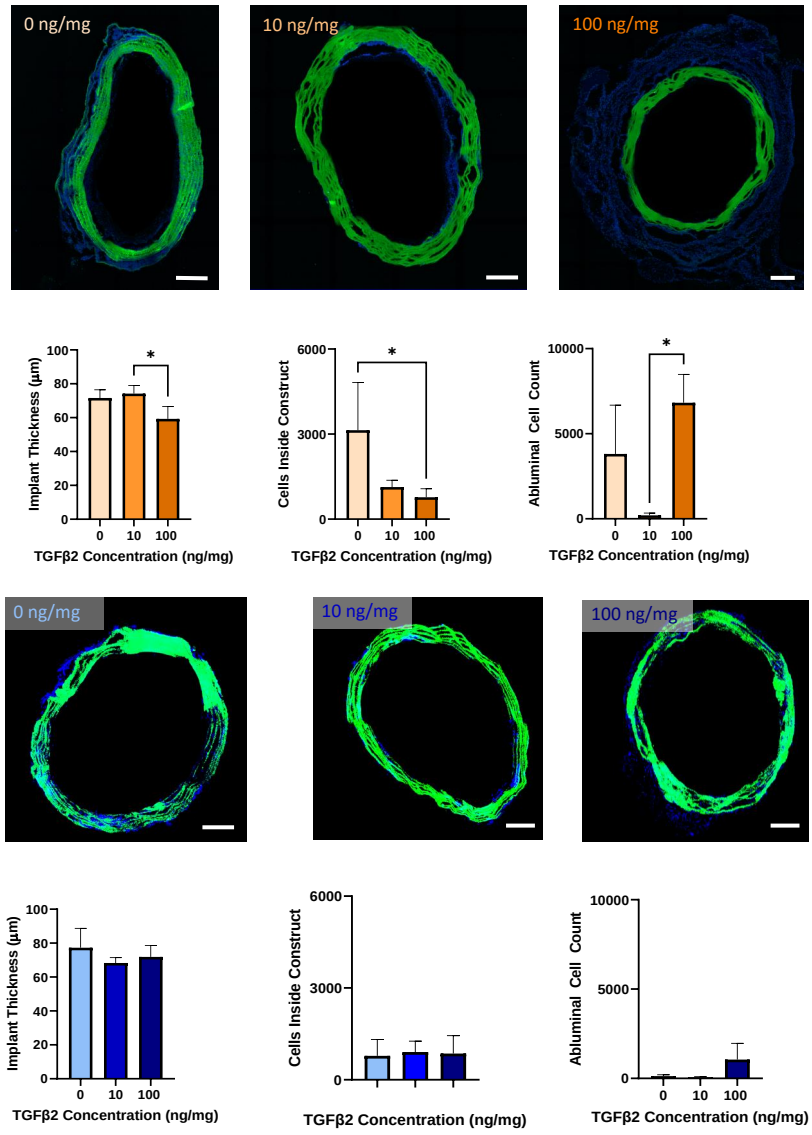

Figure 12: Compliance, diameter, and maximum velocity of 0, 10, 100 ng/mg of constructs. Orange and blue bar graphs indicate compliance-matched and hypocompliant TEVG implants, respectively. All hypocompliant grafts had a similar implant thickness and cells inside & outside the TEVGs. The increase of TGFβ2 in the CM constructs reduced the amount of cells in the construct, but increased the abluminal cells in the 100 ng/mg group. Scale bar is 100 μm. The compliant-match 100 ng/mg group was also found to be slightly thinner than the 10 ng/mg group. n=3 for each group; $*$ = p<0.05 and $**$ = p<0.01 compared to rat aorta.

3.3.4 Immunohistochemistry

Sample longitudinal and cross sectional slices were stained for SMCs, macrophages, and ECM products with the results shown in **Figure 13** and **Figure 14**. The 5 day proximal portion of the compliance-matched explant showed that the 100 ng/mg group had a reduction in SMCs but an increase in CD68 (M1 macrophage) and collagen. There was also a dramatic increase in MHC of the 10 ng/mg compared to 0 and 100 ng/mg in the compliance-matched grafts. On the other hand, the hypocompliant constructs showed no differences in the proximal and middle location of the grafts for all markers and ECM products, **Supplemental Figure 1** and **Supplemental Figure 2**.

For the proximal location of the compliance-matched grafts (**Figure 13**), the SMCs population was measured using αSMA, calponin, and MHC with differences only occurring in the MHC marker. Specifically, there was a decrease in MHC signal in the 100 ng/mg group compared to the 0 and 10 ng/mg (0.0019 ± 0.002 vs. 0.024 ± 0.003 & 0.029 ± 0.013 POI/TP, $p<0.05$). The Ki67 label did not show any differences between the groups. The definitive markers CD86 and CD163 displayed no differences between groups, but the general macrophage marker CD68 was increased in the 100 versus 10 ng/mg (0.055 ± 0.23 vs. 0.015 ± 0.001 POI/T, $p<0.04$). ECM production of collagen increased with increasing concentrations of TGFβ2, 0, 10, and 100 ng/mg (0.002 ± 0.002 to 0.003 ± 0.001 to 0.008 ± 0.002 POI/TP, $p<0.05$ 0 to 100). Overall elastin amounts in the ECM were found to be similar between all groups.

For the middle location of the compliance-matched grafts, MHC again was the only SMC marker to show differences between groups with a drastic increase in signal for 10 ng/mg group compared to the 0 and 100 ng/mg groups (0.03 ± 0.006 vs. 0.005 ± 0.002 & 0.003 ± 0.005 POI/TP). No other differences were found in the macrophage, Ki67, and ECM markers which are further highlighted in **Figure 14**.

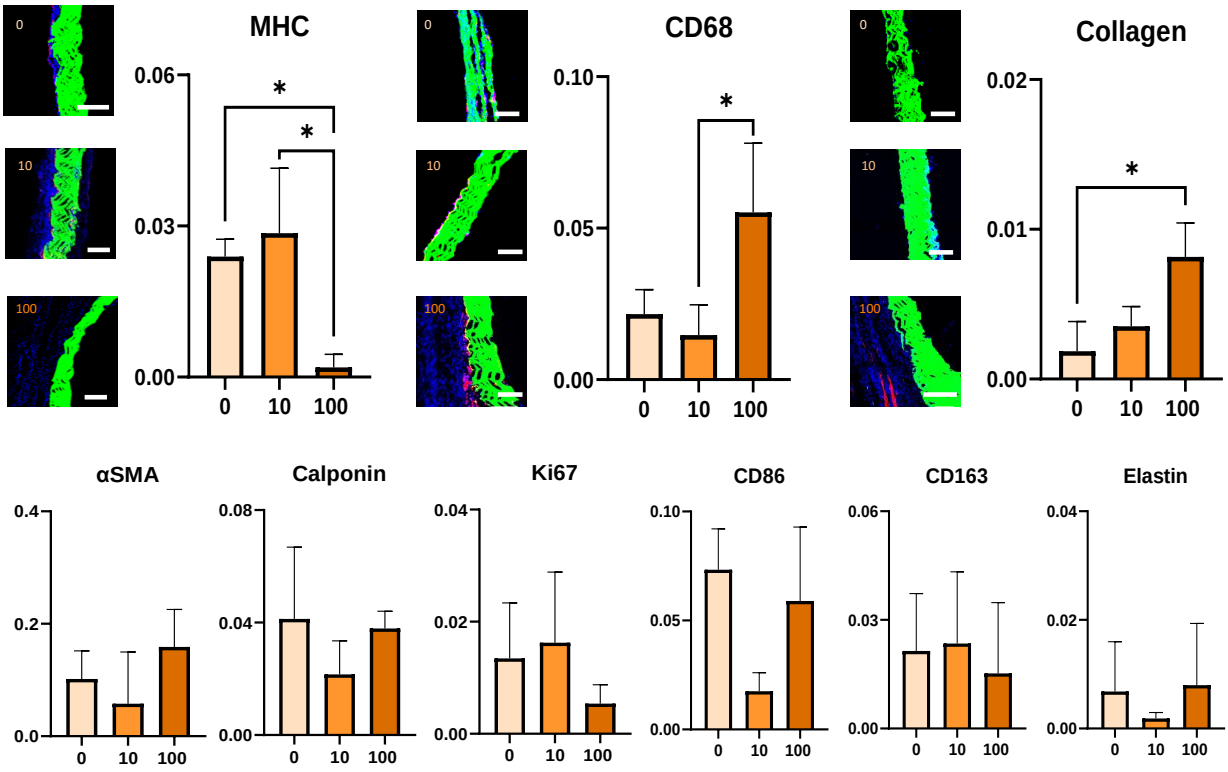

Figure 13: Compliance-matched proximal immunofluorescence images and immunohistochemistry results. The TEVG, nuclei, and each marker are green, blue, and red respectively. Immunohistochemistry quantification of the signal from MHC, pan macrophages (CD68), collagen, αSMC, calponin, Ki67, M1 (CD86), M2 (CD163), and elastin. Increasing the concentration of TGFβ2 decreased MHC signal and increased CD68 & collagen deposition in the 100 ng/mg group. $*$ = p<0.05; $**$ = p<0.01; X axis = TGFβ2 concentration (ng/mg); Y axis = Pixels of Interest/Total Pixels; Scale bar is 50 μm

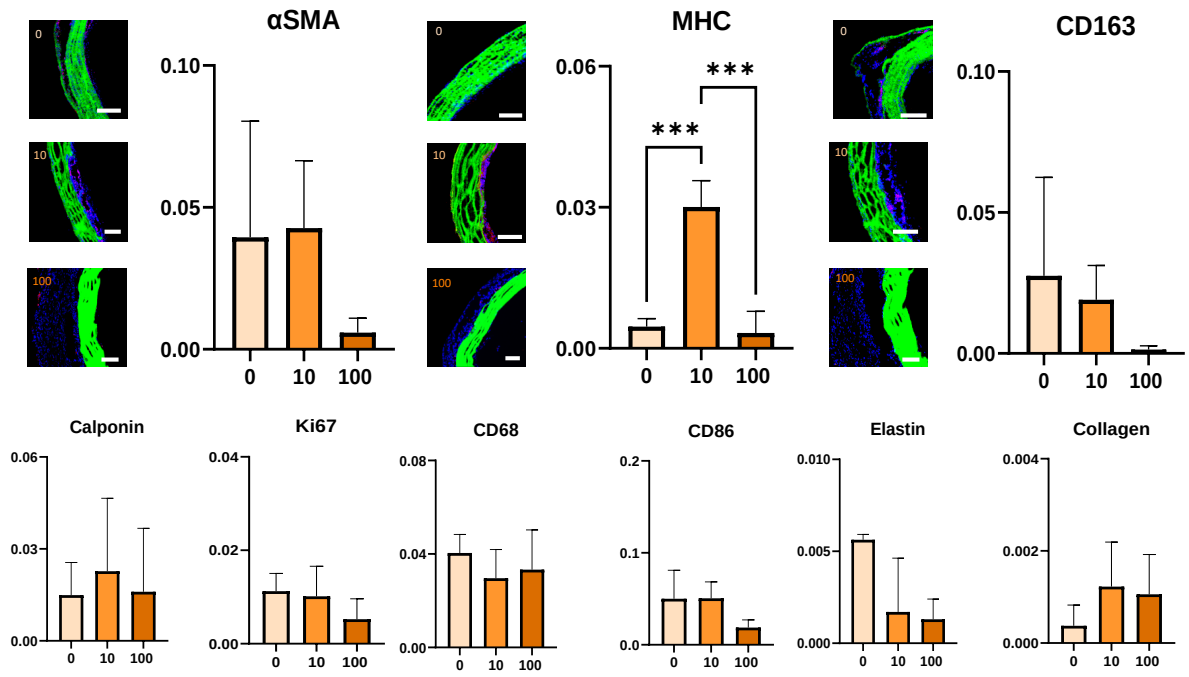

Figure 14: Compliance-matched midgraft immunofluorescence images and IHC results. Construct is green, cell nuclei is blue, and maker is red. Immunohistochemistry quantification of the signal form αSMC, MHC, M2 (CD163), calponin, Ki67, pan macrophage (CD68), M1 (CD86), elastin, and collagen. The 10 ng/mg compliance-matched construct had significantly more MHC signal than the 0 and 100 ng/mg groups. No differences were found in any other markers. $*$ = p<0.05; $***$ = p<0.001; Y axis = Pixels of Interest/Total Pixels; X axis = TGFβ2 concentration (ng/mg); Scale bar is 50 μm

3.4 Discussion

The incorporation of TGFβ2 in compliance-matched TEVGs (faster degrading scaffold) increased SMC infiltration and collagen production over an acute 5-day period. Specifically, low TGFβ2 concentrations (10 ng/mg) caused an increase in the MHC SMC marker at both the proximal and middle locations of the graft. The high concentration of TGFβ2 (100 ng/mg) in the compliance-matched grafts increased collagen production in the proximal region, halted SMC infiltration, and caused the TEVG to stiffen. The hypocompliant TEVGs (slower degrading scaffolds) displayed cellular infiltration and ECM production and were unaffected by any TGFβ2 concentrations. These results demonstrate that the elution of TGFβ2 from a TEVG can promote in vivo SMC recruitment and collagen production even after only an acute 5-day implantation period.

SMCs are vital to TEVG remodeling as they are one of the key cell types for vessel functionality. For example, the contractile phenotype is usually found in a mature vessel where it regulates vascular tone, ECM production, and minimizes cellular migration [94]. In contrast, synthetic SMCs are generally found in more immature vessels which have a higher rate of proliferation and migrate much faster across a substrate [95]. TGFβ2 and the TGFβ family are key signaling molecules that regulate SMC phenotype depending on concentration [29, 96, 97, 98, 99]. At low concentrations, the TGFβ family has been found to increase SMC proliferation through the promotion of platelet derived growth factor (PDGF) which in turn stimulates DNA synthesis [98, 100]. At higher TGFβ concentrations, PDGF expression is limited which arrests SMC proliferation and leads to an increase in ECM production [98]. These results have been confirmed in SMCs exposed to high levels of TGFβ1 that induced collagen synthesis (Kubota el al [101]). In the context of this work and TGFβ2, Ardila et al. demonstrated in vitro that using low (<0.01 ng/ml) and high (>5 ng/ml) exogenous TGFβ2 concentrations in electrospun gelatin:fibrinogen scaffolds promoted SMC proliferation and collagen production, respectively [29]. Our laboratory has taken the next step and implanted TGFβ2-eluting, compliance-matched constructs into a rat model for 5 days showing similar results with increased SMCs (MHC marker) at low concentrations and higher collagen content at 100 ng/mg. Using this knowledge, the elution of TGFβ2 from the

TEVG could be modified to promote SMC infiltration and collagen deposition subsequently. For example, Jhunjhunwala et al. demonstrated that TGFβ1 could be released at low levels for 3 weeks followed by an increased release until around 50 days using microparticle encapsulation [102]. This microparticle release profile could also be transferred to TGFβ2 and is currently being evaluated in our laboratory.

A substantial portion of TEVG research is focused on SMCs, however the immune response to the implant plays an equally important role in the success of the TEVG. Immune responses to the TEVG are broken down into the inflammatory and wound healing response [103, 104]. The inflammatory response which is closely tied to M1 macrophages (CD86) promotes encapsulation of the tissue, destruction of foreign bodies, and impeded growth [104]. While it is necessary to have this inflammatory response early on to increase the cellular population around the implant and protect the body against foreign material, a prolonged or exaggerated immune reaction can be detrimental to the TEVG [105]. Thus, promoting these M1 macrophages to move towards the M2 phenotype (CD163) encourages cellular growth around the implant, ECM production, and neovessel formation [106]. In this study, the results demonstrate the initial response to the implant with only noticeable differences in macrophages shown in the CD68 marker (generalized macrophage marker) of the 100 ng/mg compliance-matched group in the proximal location. These results suggest that increasing TGFβ2 promotes an exaggerated immune response, which has also been shown to occur in other TGFβ-influenced environments [107]. Prior work in our laboratory has also evaluated immune cells at a longer time point. Specifically, the 0 ng/mg compliance-matched implant has been previously implanted in Sprague Dawley rats for one month and compared to a hypocompliant control TEVG. The M2/M1 ratio of macrophages in the 0 ng/mg compliance-matched grafts were found to be higher than in the hypocompliant grafts [32]. Thus, suggesting that the compliance of the implant is more suitable for positive TEVG remodeling. While there are no noticeable differences in M1 and M2 population at 5 days in the compliance-matched construct, we anticipate this M2/M1 ratio may carry over in the 10 and 100 ng/mg groups in future studies. Longer time points and larger sample size will need to occur before there is a clear understanding of the longer term effects of TGFβ2 on TEVG remodeling.

One major difference between the compliance-matched and the hypocompliant grafts were the degradation rate of the scaffold [27]. Previous work has shown that the compliance-matched construct degrades twice as much as the hypocompliant graft in one month [32]. This degradation of the scaffold is vital for the release of TGFβ2. Past in vitro work has shown that in 5 days the compliance-matched TEVG can elute about 20 to 30 times more TGFβ2 than the hypocompliant grafts [27]. Thus, the reduced degradation/elution of hypocompliant constructs is believed to be the reason why there were no differences between any of the hypocompliant groups in this work. This is surprising considering that the 100 ng/mg hypocompliant group has an order of magnitude more TGFβ2 than the 10 ng/mg. Another reason for the lack of TGFβ2 release from both scaffolds may emanate from the genipin crosslinking procedure. Each construct is submerged in 0.5% genipin in 100% ethanol at 37^o and shaken for 24 hrs. During this procedure, any loose or unbound TGFβ2 may be eluted into the genipin solution which would reduce the amount of growth factor available. A potential solution to prevent the loss of TGFβ2 is to explore alternative crosslinking procedures such as using ultraviolet light, vapor, chemical, or plasma treatment [108]. Future testing could incorporate one of these crosslinking methods to prevent the potential loss of TGFβ2 during the fabrication process.

One unexpected result from this work was the decreased compliance in the 100 ng/mg compliance-matched construct compared to rat aorta. Specifically, this graft stiffening comes as even more of a surprise due to the acute nature of the implantation period and the decrease in implant thickness of the 100 ng/mg compliance-matched construct (60 μm) in reference to the 0 and 100 ng/mg groups. This decrease of compliance is related to the increase of cells in the abluminal region of the 100 ng/mg group. All 100 ng/mg compliance-matched samples had large abluminal populations compared to the vastly varying abluminal cellular populations of the 0 and 10 ng/mg TEVGs. To further understand these results, our laboratory has also investigated the 100 ng/mg compliance-matched and hypocompliant grafts at a 4 week implant (**Supplemental Figure 3**) and found that this decrease of compliance also led to an increase in luminal thickness and cellular alignment compared to 0 ng/mg at 4 weeks. As these results and previous literature suggest, TGFβ can be atheroprotective and atherogenic depending on the cellular environment [29, 93]. The increase in alignment

demonstrates that high TGFβ2 concentrations may promote a contractile SMC phenotype, but could also encourage intimal hyperplasia. This increase of intimal hyperplasia could be related to the endothelial-to-mesenchymal transition of endothelial cells in the TEVG. From previous work, high TGFβ concentrations in mouse endothelial cells cause cells to become more leaky, transition to an mesenchymal state, and lead to increased atherosclerotic lesion markers [109, 110]. Controlling the concentration and release of TGFβ2 from compliance-matched TEVGs will be ideal for maintenance of compliance as the graft is remodeled in vivo.

All TEVGs remained patent throughout the time course of this work. These initial results suggest that the inclusion of TGFβ2 does not affect in vivo patency, velocity, or diameter over a 5-day period. This is consistent with our prior work showing that the velocity, diameter, and compliance of 0 ng/mg implanted TEVGs remained similar over a four-week implantation period [32]. The only drawback from our previous study was that both compliance-matched and hypocompliant grafts clotted in 2/7 and 1/7 of the trials, respectively (no significant differences between groups).

A major limitation of this study was the short 5-day implantation period. The motivation for this work and selection of study duration, as stated previously, was to relate to prior work done by Ardila et al [27]. Her in vitro study and this work confirm that low TGFβ2 concentrations promote SMC proliferation and migration in a TEVG over an acute period. Another limitation in the current study was the small sample size, n=3, which was mainly selected to demonstrate the potential of TGFβ2-eluting TEVGs. Further TGFβ2 studies are needed to fine tune in vivo TGFβ2 release such as concentration, elution profile, and timing. Our current working hypothesis of TGFβ2 release is that a low concentration will promote early SMC infiltration and a subsequent higher dose will promote ECM production that will stabilize the compliance of our fully biodegradable TEVG. While these results are promising, other factors will have to be taken into account to find the ideal TGFβ2 release profile for a particular animal species, side effects of TGFβ2, graft composition (as shown in our hypocompliant group), and several other factors. The acute response of the host to TGFβ2 in this study will hopefully spawn additional future research exploring the next generation of TEVGs that elute bioactive factors to improve functional in vivo performance.

While TGFβ and its family of cytokines has been given significant attention in the literature, studies that focus on the exogenous delivery of the TGFβ2 isoform specifically are limited. This is important to note as there may be fundamental differences in the binding between TGFβ 1 & 2 and the actions of TGFβ1 may not always relate directly to TGFβ2 [111, 112]. For example, the RGD (Arg-Gly-Asp) integrin binding region found in the LAP of TGFβ1 and TGFβ3 is lacking in TGFβ2 which suggests that it may have a different method of activation [113]. This may play a role in functional differences during cardiovascular development, as heterozygous TGFβ1 knockout mice function similarly to wild type animals, whereas TGFβ2 mice present with aortic root dissection [114]. In terms of vascular remodeling, TGFβ is again a regulator of cellular migration/proliferation at low concentrations and prevents movement at higher concentrations [93]. This growth factor not only affects SMCs but endothelial cells, macrophages, and lymphocytes. The exact timing and concentration of TGFβ elution are key for success or failure in vivo. For example, high TGFβ concentrations early may prevent endothelial cell migration into the implant [115], thus increasing the likelihood of a possible thrombotic event. In contrast, a higher TGFβ concentration later may promote collagen development in the TEVGs. Elevated TGFβ levels may not be ideal after the initial implantation once the vessel has matured. Specifically, the upregulation of TGFβ can promote an increase in collagen production to stiffen the vessel and lead to calcification [93]. These results have been demonstrated in a rat and a rabbit model with the addition of exogenous TGFβ or after a vascular injury [116, 117]. Thrombotic events may occur more frequently as well as TGFβ1 is less at efficient at clearing thrombosis formation due to an increase in plasminogen activator inhibitor activity [118]. Keeping all of these factors in mind, the delivery of TGFβ will need to be tightly controlled for a desired long term functional outcome.

3.5 Conclusion

To the author's knowledge, this is the first study to assess in vivo TGFβ2 release from a compliance-matched and hypocompliant TEVG over an acute 5-day period. His-

torically, TGFβ2 has been found to be a potent SMC phenotype modulator and this was confirmed through the in vivo work in this study. As TGFβ2 concentrations increased in the compliance-matched constructs the production of collagen was elevated, the SMC population was reduced, the TEVG became less compliant, and caused a larger immune response. On the other hand, the lower concentration of TGFβ2 in the compliance-matched construct increased SMC infiltration and proliferation. The degradation of the scaffold was key to TGFβ2 elution as the slower degrading hypocompliant construct had no affect on the cellular environment or implant. We believe this work demonstrated that TGFβ2 incorporated into a TEVG was beneficial for SMC migration, proliferation, collagen production, and hope this study will inspire new studies in the vascular tissue engineering field.

4.0 Tracking Delivery of a Drug Surrogate in the Porcine Coronary Artery Using Photoacoustic Imaging and Spectroscopy

This aim will focus on an alternative imaging technique to evaluate in vivo drug delivery and degradation from a TEVG or a stent. This technique, photoacoustic imaging, uses a combination of ultrasound and a tunable laser light source to identify known absorbers or dyes in the surrounding medium. The porcine heart, vasculature, and coronary arteries will be exposed to a dye and a method will be developed to determine dye concentration and location. This method could pave the way for future in vivo imaging for the evaluation of drug release from a TEVG (aim 2) or degradation in vascular grafts.

4.1 Introduction

Throughout this dissertation, the primary focus has been on evaluating compliance specific and eluting TEVGs through ultrasonic, histological/fluorescence, and multiphoton imaging. Here we look to expand our standard method of TEVG evaluation with the incorporation of photoacoustic imaging and spectroscopy (PAIS). This technique combines ultrasonic imaging with a non-ionizing tunable laser to provide sub-mm in vivo resolution, millimeters of depth penetration, and the ability to detect wavelength specific absorbers in the tissue. Specifically, this technique is based on the photoacoustic effect, which starts from the tissue absorbing a short pulse of light that causes transient heating leading to thermoelastic expansion that generates a sound wave which is detected by an utlrasonic probe. The sound waves are used to create an ultrasonic image with contrast that is proportional to the absorption of light. The distribution and relative concentration of optically absorbing contrast agents in the implant can also be estimated through the scanning of multiple wavelength and spectral decomposition.

PAIS offers many advantages over other imaging modalities. For example, while magnetic resonance imaging [MRI], computed tomography [CT], and ultrasound [US], are capable of anatomical and functional imaging of the heart and implant, they typically lack

sufficient contrast to identify and track pharmacological compounds in the vasculature and myocardium. Standard techniques to evaluate vascular grafts such as ultrasonic, histological or fluorescence, and multiphoton imaging have some major drawbacks as well. For example, fluorescence microscopy and histology are used to identify specific cells or components but require explantation and destruction of the tissue. Lastly, multiphoton confocal microscopy has the ability to provide in vivo imaging but is limited in depth penetration, <1 mm [119, 120, 121]. PAIS provides high contrast and specificity for detecting and tracking optically-absorbing compounds in the vascular tissue, implant, and myocardium. These attributes are not only favorable for testing and improving the performance of a vascular graft, but the technology is potentially translatable for in vivo imaging in small/large animals and humans.

Another major aspect of this aim is to evaluate another style of vascular graft, stent. As mentioned before, this device is a tubular structure often made of metal that can be deformed to prop open a narrowed or atherosclerotic vessel. Specifically, stent implantation or percutaneous coronary intervention (PCI) is performed in almost 0.5 million cases each year in the U.S. [122]. This procedure often acts as an noninvasive alternative to TEVG implantation as most procedures are performed by insertion of a catheter through the femoral artery. Since the inception of PCI, this procedure has led to major advancements in stent technology, drug eluting stents (DES), through the incorporation of drugs onto the stent. DES restenosis has also been reduced over the years by improving drug retention and transport in the coronary arteries through modification of the drug's chemical structure [123, 124]. These drugs work by targeting the smooth muscle cells in the tunica media to reduce or prevent the migration and proliferation leading to atherosclerosis [125]. Yet there is still concern about failure rates from vessel restenosis with cases occurring in up to 20% of patients [122, 126, 127, 128, 129]. One of the underlying themes in this work was to also monitor or visualize drug delivery to the coronary artery using PAIS. From past work, we have shown that drug transport and mechanical properties of the porcine coronary arteries vary as a function of vessel and location [119, 130, 131]. However, currently, there is no ideal imaging modality to monitor and quantify drug delivery to the coronary artery with sub-mm precision.

In this study, we chose to test the feasibility of using PAIS in an explanted porcine

heart and vasculature. The primary focus of this work was to evaluate transport from a drug surrogate. This method uses an ex vivo model which eliminates the need to keep the tissue alive and focuses on refining the PAIS technique through the calibration and quantification of the photoacoustic signal. In the final aspect of this work, we fabricated a stent, coated with a drug surrogate (also a PA contrast agent), and track its position in the intact porcine brachiocephalic trunk, demonstrating this technique could be used in a large animal carotid model. Overall, we hypothesize that noninvasive imaging of vascular grafts will provide real time feed back about the graft and be able to monitor in vivo drug delivery [119, 123, 130, 131, 132, 133, 134, 135, 136].

4.2 Methods

4.2.1 PAIS Setup and Dye

Optical and Ultrasound Setup (**Figure 15A**): A wavelength-tunable laser (Surelite-II OPO, Continuum, 5 nsec pulses, 20 Hz pulse repetition rate, 20 mJ/pulse) operating between 410nm–670nm was coupled into a 1.6 mm diameter multimode optical fiber (CeramOptec) that connected to a "photoacoustic enabling device" (PED). Specifically, the PED held both the optical components and linear ultrasound array (Zonare L10-5, 7.1 MHz center frequency, 5 MHz bandwidth) for co-registered pulse echo and photoacoustic imaging, which has been previously described [137, 138]. Furthermore, the PED allowed for co-alignment between the optical illumination and plane of ultrasound detection. Briefly, light from the fiber passed through a cylindrical lens to provide line illumination at the surface of the tissue. The backscattered photoacoustic waves were reflected by an inline acoustic reflector before being detected by the linear array and recorded in real-time by a clinical ultrasound scanner (zOneUltra, Zonare Medical Systems). The PED was filled with water for acoustic coupling. Raw frame data (amplitude and phase) were transferred from the scanner to a personal computer running MATLAB^{TM} for sum-delay beamforming and post signal processing. The axial and lateral resolutions of the photoacoustic imaging system were 300 μm and 400 μm, respectively [137]. The slice thickness was approximately 2 mm. The fluence on the surface of

the heart was 10 mJ/cm2 and below the American National Standards Institute safety limit of 20 mJ/cm2 per pulse light at visible wavelengths following American National Standards Institute Z136.1.

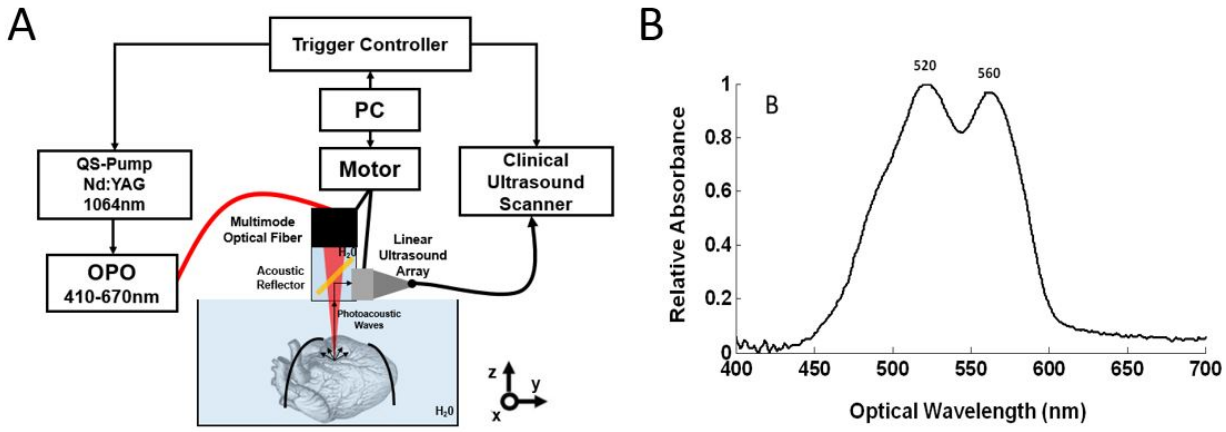

Figure 15: **Photoacoustic Imaging setup and Optical Properties of DiI.** A) Nd: YAG laser was tripled to 355 nm to pump an optical parametric oscillator (OPO) and produce tunable 5 nsec pulses between 410 nm – 670 nm. Laser light was coupled into a 1.6 mm diameter multimode glass fiber. The fiber connected to a PA flashlight adapter, including an optical assembly with a cylindrical lens to produce a line pattern on the heart [20]. The adapter also contained a water-filled cavity for acoustic coupling and an acoustic reflector, which ensures co-alignment of the light with the plane of ultrasound detection. A clinical ultrasound scanner (ZoneUltra, Zonare Medical Systems) and 7 MHz linear array (L10-5) recorded the raw acoustic signals (phase and amplitude) for ultrasound and PA imaging. The frame data were transferred to a PC for beamforming, post processing and analysis in MATLAB^{TM}. B) Optical absorption spectrum of DiI as measured with a photospectrometer (Ocean Optics, USB4000).

Drug Surrogate: 1,1'-Dioctadecyl-3,3,3',3'-Tertramethyllindocarbocyanine Perchlorate (DiI) was selected for PA imaging due to its weight match to rapamycin, hydrophobic nature, cost, and favorable absorbance spectrum at visible wavelengths (**Figure 15B**) [119]. DiI was acquired from Invitrogen (Carlsbad, CA).

4.2.2 Image Processing and PA Signal Decomposition (Unmixing)

The primary optical absorbers at visible wavelengths in this study were the myocardium and DiI, which were separated by spectral decomposition. The PA signal is calculated using the following equation:

$$PA = T * \varphi * \mu. \tag{4.1}$$

where PA is the photoacoustic signal in MPa, T is the dimensionless Grüneisen constant that converts optical energy into acoustic pressure, φ is the laser fluence J/cm2, and μ is the total absorption coefficient in cm-1 [139]. Total tissue absorption equals the sum of the signals obtained, which is described by the following equation:

$$\mu_{total} = \Sigma_{m=1}^{M} c_m * \mu_m. \tag{4.2}$$

where c_m is the concentration of the mth absorber, μ_m is the absorption coefficient of the mth absorber and M is the number of tissue absorbers. The fraction of sample absorbers is written in matrix notation as:

$$A\bar{c} = \bar{b}. \tag{4.3}$$

with A an MxN matrix containing the absorption coefficient of M absorbers at N wavelengths. $\bar{c}$ is a 1xM vector containing a fractional distribution of M agents. $\bar{b}$ is a 1xN vector of a normalized PA signal over each wavelength [132]. The least squares of the residuals is used to solve for $\hat{c}$:

$$\hat{c} = (A^T * A)^{-1} * A^T * \bar{b}. \tag{4.4}$$

$\hat{c}$ is a signal estimation of a specific absorber based on least squares This technique separates DiI from the myocardium and other possible absorbers like hemoglobin.

4.2.3 Photoacoustic Imaging Experiments

Porcine Cardiac Tissue: All tissue obtained in this study was approved through the University of Arizona Institutional Animal Care and Use Committee. Adult porcine hearts

(n=5) were acquired from the University of Arizona Food Products and Safety Laboratory and maintained at 4^oC for up to 24 hours until imaging.

Validation and Calibration in Excised Myocardium: A porcine left ventricle was cut into seven rectangular sections (approximately 1 x 1 x 0.5 cm). Samples were soaked in DiI for 24 hours at different concentrations (0, 2.4, 4.8, 9.6, 38.4, 76.8, and 120 μg/ml) and embedded in agarose gel. Volumetric photoacoustic and ultrasound images were collected by scanning the linear array along the elevational axis with 100 μm increments. The average PA signal was calculated over the region of interest (ROI), which was determined from the co-registered B mode ultrasound image and excluded the tissue boundary. A calibration curve was generated by plotting the average PA signal vs. the DiI concentration.

In Situ Porcine Heart Imaging: Three porcine hearts were cut proximal and distal to the coronary artery, and a cannula was inserted into the Left Anterior Descending Coronary Artery (LADCA), which was initially flushed with water using a syringe pump (KD Scientific KDS230 KDS 230 Multi-Syringe Pump). Standard ultrasound helped identify the vessel location, size, and structure. Cross sectional PA images were taken from 430 nm to 670 nm (10 nm increments). The porcine LADCA was perfused with 2.4 μg/ml and maintained for 20 minutes, followed by imaging, flushing with water, and re-imaging with pulse echo (PE) and PA. The process was repeated at incrementally higher concentrations (i.e., 12 μg/ml and 60 μg/ml). The relative contribution of DiI at each pixel was determined from spectral decomposition. The distribution of DiI was also used to calculate coronary artery diffusion area and distance. Diffusion area was calculated by subtracting the background from the DiI signal and setting a threshold value. The total number of pixels with DiI were multiplied by the pixel size (0.05 mm X 0.05 mm) to determine the diffusion area. The center of the LADCA was determined from the PE ultrasound image, and the diffusion distance was calculated by extending a line from the LADCA center point radially outward. Continuous pixel values along the line greater than background was used to calculate diffusion distance.

Imaging of DiI-coated Stent: A Cobalt chromium stent with a sinusoidal pattern was designed in Solidworks® and fabricated by Proto Labs®. Half of the stent was dipped into DiI/PCL (60 μg/ml DiI and PCL) solution and dried for 20 minutes; this process was repeated three times. A coating of polydimethylsiloxane (PDMS) was also added to prevent

short-term elution. The uncoated region served as a control to compare to the coated region. The stent was initially imaged in water and, later, inserted into the brachiocephalic trunk for both PA and PE imaging.

4.3 Results

4.3.1 Validation and Calibration in Excised Myocardium

Images of four of the seven myocardial samples are displayed in **Figure 16**. Wavelengths of 550 nm and 660 nm represented the local maximum and minimum for DiI absorption in the visible range. Whereas at 550 nm the PA image was dominated by DiI absorption, at 660 nm the image was dominated by the intrinsic absorption of the myocardium. In general, the PA signal intensity increased linearly with concentration. The final column represents the DiI concentration after unmixing the PA signal at all the wavelengths.

These data were used to generate a calibration curve for DiI in the excised myocardium. The average PA signal (over the ROI) was plotted against the prepared DiI concentration (**Figure 17**). The axes are displayed in octaves to match the distribution of prepared DiI concentrations.

Figure 17 indicates a strong linear relationship spanning almost 8 octaves between the DiI sample concentration and the amplitude of the PA signal. In addition, minute concentrations of DiI (<2.4 μg/ml) could be detected at high spatial resolution (<300 μm) deep in tissue (>5 mm). These favorable attributes of PA imaging were extended to study transport in the porcine coronary artery and myocardium.

Imaging of the Porcine Heart (In Situ): DiI at 2.4 μg/ml was perfused into the LADCA for 15 seconds (**Figure 18**). The PA signal at 550 nm near branching vessels increased linearly during the perfusion, demonstrating real-time capabilities of PA imaging for tracking drug transport and diffusion.

Estimates of DiI diffusion in the porcine heart is presented in **Figure 19**. The PA spectrum was dominated by absorption of the myocardium except at regions with high DiI. Areas of DiI diffusion for 2.4, 12, and 60 μg/ml were calculated at 1.30, 1.75, and 3.30 mm^2,

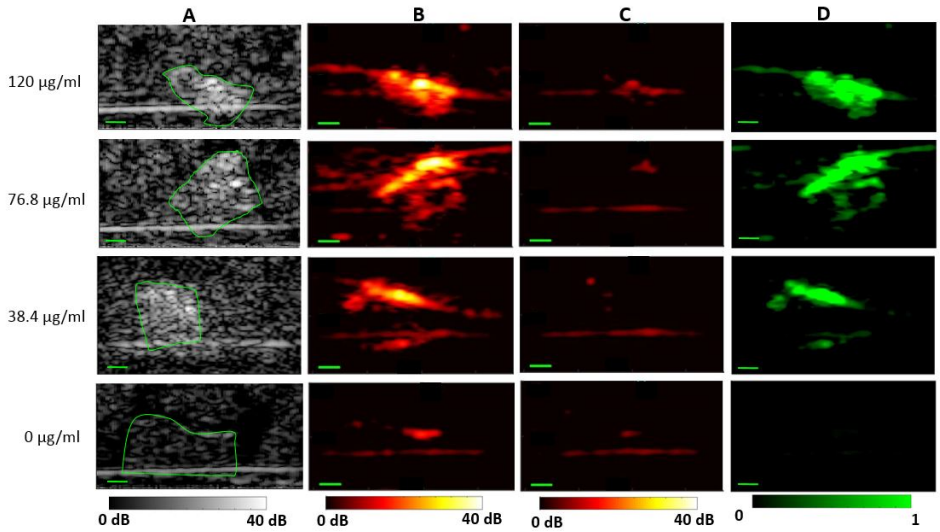

Figure 16: **Ultrasound and photoacoustic imaging of porcine myocardial samples stained with DiI.** Each row represents a sample stained with a different concentration of DiI (0 μg/ml, 38.4 μg/ml, 76.8 μg/ml, and 120 μg/ml). Column A) Cross sectional PE ultrasound images of samples embedded in Agarose^{TM}. Samples are outlined in green. Column B) Corresponding PA signal at 550 nm (near peak of DiI absorption). Column C) PA signal at 660 nm (low DiI absorption). Column D) Relative concentration of DiI after spectral decomposition. Green scale bar represents 2 mm.

respectively. Therefore, an increase in DiI concentration led to an increased in diffusion area. These results demonstrated that PA imaging can track transport of DiI, a drug surrogate.

In addition to diffusion area, we also calculated the diffusion distance from the center of LADCA, which depended on the concentration (**Figure 20**). DiI diffused an average of 0.95 ± 0.37 mm, ranging from 0.6 mm to 1.5 mm (**Figure 20C**). These results suggest that PA imaging can track transport several millimeters from the coronary into the myocardium.

Ultrasound and Photoacoustic Imaging of a DiI-coated stent: A cardiovascular stent was fabricated to test if PA imaging could detect DiI coated on a stent placed inside a blood vessel. Images of the DiI-coated cardiovascular stent are presented in **Figure 21**. PA imaging was able to differentiate the coated vs. uncoated region in water and in the brachiocephalic trunk (**Figure 21D** and **21F**, respectively). These results demonstrated

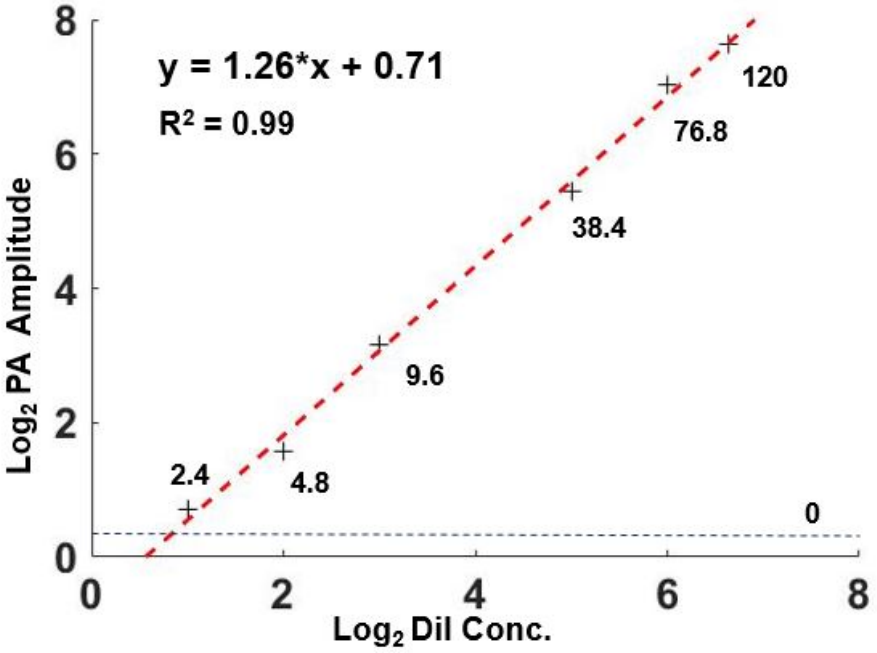

Figure 17: **PA Calibration Curve for DiI.** The pixel values over the ROI were averaged and plotted against the prepared concentration of DiI for each sample. The equation for the best fit line (dashed red) and R2 value are also indicated. All concentration values are in μg/ml. Based on the PA signal without DiI (blue dashed line), the sensitivity of PA for detecting the dye in the samples was approximately 2 μg/ml.

that PA imaging was able to detect DiI on a stent placed inside a large blood vessel.

4.4 Discussion

Our results demonstrated that PAIS is a nondestructive method that tracks drug delivery in the porcine vasculature while providing excellent contrast, depth, and resolution. PAIS was able to quantify the distribution of a drug surrogate at concentrations from 2.4 μg/ml to 120 μg/ml. Perfusion of DiI into the coronary artery increased the PA signal in the surrounding tissue greater than 1.5 millimeter away from the targeted vessel. PAIS was also able to differentiate the brachiocephalic trunk from the coated and uncoated regions of

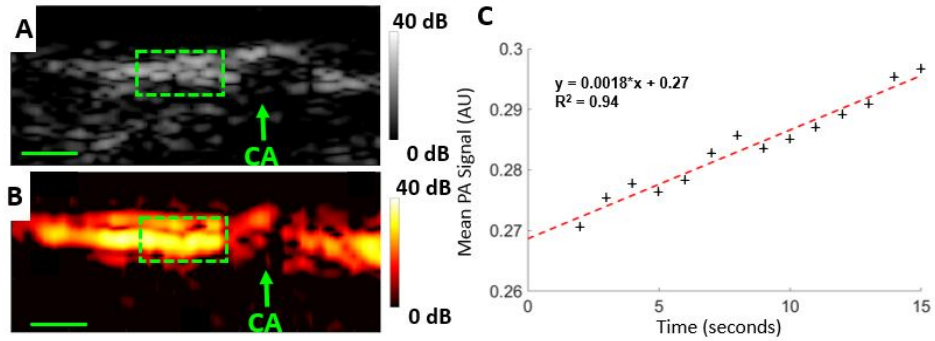

Figure 18: **Increase in PA Signal near LADCA during DiI Perfusion.** (A) Cross sectional PE image of an ex vivo porcine heart. (B) Co-registered PA image at 550 nm during infusion of 2.4 μg/ml DiI. Vessel pressure was maintained at 70 mm Hg. C) Average PA signal over time inside dashed green box during infusion of DiI. The PA signal increase is observed in myocardial tissue adjacent to the coronary (CA) vessel. The scale bar denotes 2 mm.

a stent. Our results suggest that PAIS may be a valuable tool for tracking drug delivery to a specific vessel and provide feedback on drugs loaded onto a vascular implant or DES. In this regard, PAIS may help improve the design of a vascular implants, increase drug retention and delivery to the coronaries arteries from DES, and reduce in-stent restenosis.

Our approach has not only demonstrated that PAIS may be a useful tool for assessing drug delivery in vitro but could also be used in preclinical animal models of vascular disease. For example, a porcine thoracic window to the coronary artery could provide time course information about in vivo drug delivery [140]. Specifically, DES polymer degradation and therapeutic drug transport could be monitored over time in the same animal thus minimizing the number of animals used in preclinical studies. For TEVGs, PAIS could easily track in vivo degradation and cellular infiltration using a sheep carotid model due to proximity of the vessel to the skin or the rat abdominal aorta model. Our results further suggest that the PA signal from the vascular graft and surrounding tissues could be used to estimate drug concentrations thus providing real time feedback for improving vascular design.

To visualize drug delivery, this study implemented a drug surrogate with a peak absorp-

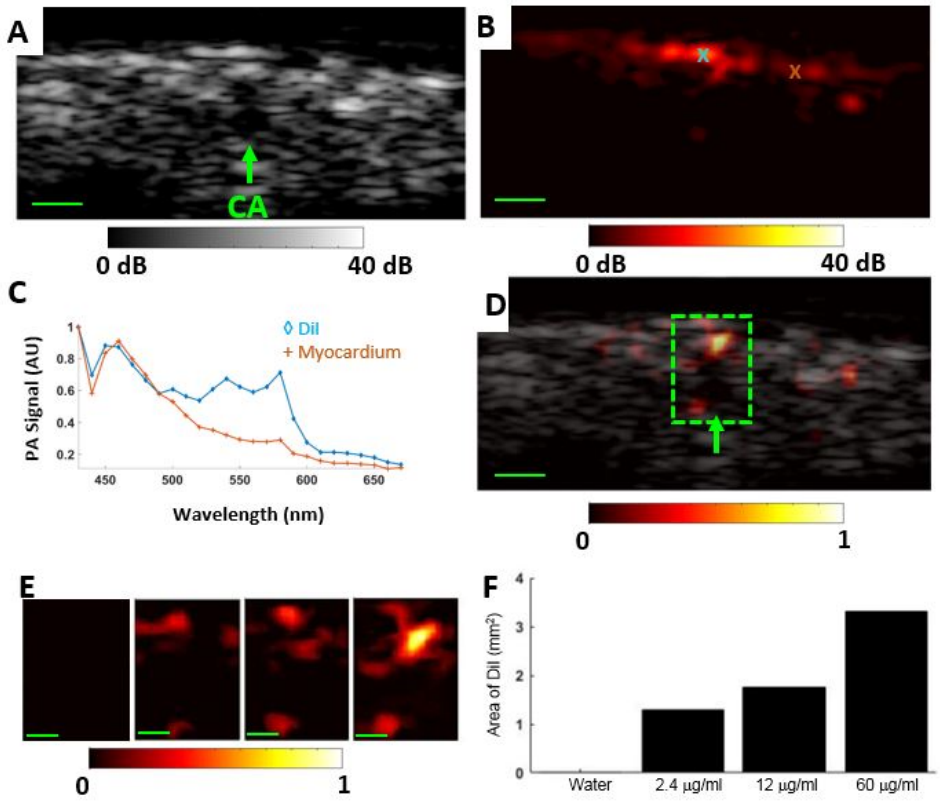

Figure 19: **Estimation of DiI diffusion in the heart near the LADCA.** (A) Cross sectional PE ultrasound image over LADCA. (B) Co-registered PA image at 550 nm with a dynamic range of 40 dB. The PA spectra over regions of interest marked with "X" are displayed in (C). Brown and blue regions are similar to the known absorption spectra of the myocardium and DiI, respectively. (D) Co-registered PE (gray) and unmixed PA signal for 60 μg/ml DiI concentration (following flush). Green box identifies the ROI for cumulative diffusion analysis. E) PA images over ROI (green box) for DiI concentration of 0 μg/ml (100% water), 2.4 μg/ml, 12 μg/ml, and 60 μg/ml. f) Diffusion area for each concentration based on PA signal over background. Scale bar is 2 mm.

tion near 550 nm. At this wavelength, penetration depth in cardiac tissue is about $\sim$5 mm due to overlap in intrinsic background absorption (e.g., hemoglobin). However, if the drug surrogate is exchanged for a near infrared (NIR) absorber, PAIS should be able to track drug delivery even deeper (>10 mm) into tissue with less interference from background absorption

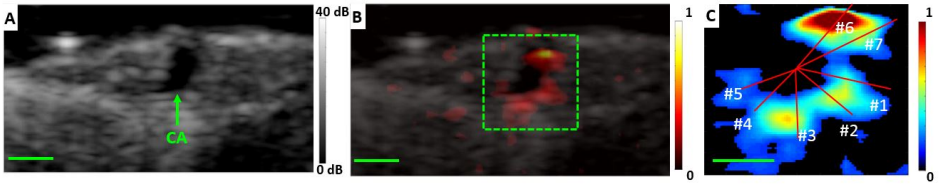

Figure 20: **Diffusion distance from LADCA.** (A) Cross sectional ultrasound image of the LADCA in the porcine heart. (B) Overlay of PE ultrasound (gray) and PA (hot) images Scale bar = 2 mm. (C) Calculation of diffusion distance from LADCA based on signal above threshold noise inside dashed box in (B). Diffusion distance for this example ranged from 0.6 to 1.5 mm. Scale bar = 1 mm.

[140]. In this case, it may be possible to use fewer wavelengths for spectral decomposition, thereby simplifying the imaging procedure and scan time. Looking more into TEVGs, currently there is no fluorescently labeled TGFβ-2 available, but in vivo degradation could be tracked by the incorporation of a dye into the fiber. For DES, most restenosis drugs absorb in the ultraviolet range which limits penetration depth [141, 142]. Therefore, it could be desirable to conjugate a small-molecule dye onto the drug to track delivery using PAIS. For example, the 42' hydroxyl group on rapamycin has shown great promise for conjugation of an optically-absorbing dye. One group has successfully attached 7-bromo-4-nitrobenzofurazan, a visible spectrum dye, onto rapamycin [143]. Conjugating rapamycin with a visible or NIR absorber would facilitate PAIS for quantifying drug delivery to the coronary artery.

In order to track drug delivery, there are many confounding factors that affect the PA signal in the heart: dye concentration, laser fluence, sample geometry, dye distribution, background absorption, and photobleaching. To reduce effects of pulse-to-pulse variations of the laser, we averaged the signal at each location over several pulses. Photobleaching of the dye was also kept to a minimum by only exposing the samples to light while recording data (typically less than 10 pulses at each location). To reduce effects of the geometry on the PA signal during the calibration experiment, each sample was cut to a similar size and shape and placed in the agarose gel at the same depth. The ROIs were chosen inside the sample to reduce boundary effects of the PA signal. Finally, dye variations inside each sample were

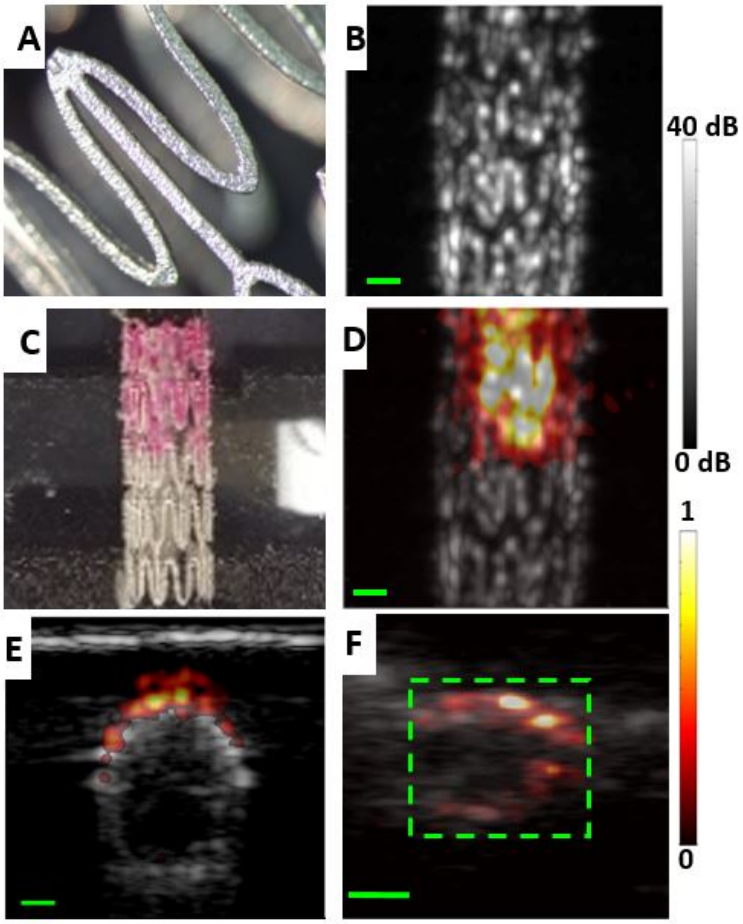

Figure 21: **Pulse Echo and Photoacoustic Imaging of DiI-Coated Cardiovascular Stent.** (A) Zoomed-in photograph of sinusoidal pattern of stent; (B) Top view PE ultrasound image of stent at 7.1 MHz. (C) Top view photograph of stent with DiI/PCL + PDMS coating on top half. (D)-(E) Co-registered PE ultrasound (gray) and PA (hot) at 550nm image (D = long view, E = cross view) of stent in water with coating on top half. (F) Co-registered ultrasound and unmixed PA signal of stent implanted in the brachiocephalic trunk. Scale bar 2 mm. Green box highlights the stent in the blood vessel.

reduced by soaking the samples for 24 hours in the dye. A similar protocol was employed by Keyes et al. prior to PA imaging in porcine LADCA samples [119]. In that study, it was assumed that 24 hours was sufficient for saturation of the dye in the tissue.

There were two other primary limitations in this study. First, the spatial resolution of

$\sim$300 μm was limited by the 5 MHz bandwidth of the ultrasound transducer. A higher frequency ultrasound probe (e.g., >50 MHz) could be incorporated into our system to improve the resolution to less than 50μm, which would be sufficient to track diffusion through layers of the coronary wall [144]. Another limitation was the inability to directly apply our setup to image the heart in vivo. Although transthoracic PA imaging is possible, penetration would be limited to about 2 cm. In this case, intravascular ultrasound/PA (PA-IVUS) would be the most practical solution for in vivo cardiac imaging of a DES. Currently, PA-IVUS has been used to track the position of a stent and detect vulnerable plaque in animal models [145, 146, 147, 148]. Such probes are being developed and tested by other groups with the ultimate goal of clinical translation [146, 149, 150, 151, 152].

4.5 Conclusion

This study demonstrated that PA imaging offers excellent spatial resolution, penetration, and contrast for tracking transport of a drug surrogate in the porcine vasculature. PAIS also improves the specificity for estimating drug concentrations by separating the signal from intrinsic background absorbers in the cardiac tissue. In the future, in vivo PA imaging of drug retention and delivery may not only be possible in the coronaries but throughout the native vasculature. This technique could improve TEVG and stent design by tracking drug delivery and degradation noninvasively throughout multiple time points while minimizing the number of animals needed per group.

5.0 Conclusion

5.1 Overview

Throughout this work, we have investigated multiple vascular grafts to gain a better understanding of how compliance and TGFβ2 affect vascular graft design, while demonstrating a new method to evaluate graft drug delivery and degradation. In the TEVGs, we were able to measure the graft's in vivo vessel diameter, compliance, and maximum velocity using doppler ultrasound. Immunohistochemistry results from the TEVGs were quantified to determine the cell type (marcophage, SMC, and endothelial). Extracellular components, collagen and elastin, were also measured to calculate deposition. In a stent, photoacoustic imaging was used to determine drug surrogate diffusion into a porcine coronary over time.

In aim 1, compliance-matched and hypocompliant TEVGs were implanted into Sprague Dawley rats for 28 day and imaged to evaluate the effect of compliance on the TEVG. Next in aim 2, these implants were loaded with varying amounts of TGFβ2 (0, 10, and 100 ng/mg) and implanted in rats for an acute 5 day study to promote faster/increased cellular infiltration. Lastly, in aim 3 we evaluated an alternative method to track in vivo construct degradation, cellular infiltration, and drug release using photoacoustic imaging.

5.2 Summary of Results

5.2.1 Chapter 2: In-vivo assessment of a tissue engineered vascular graft computationally optimized for target vessel compliance

In chapter two, TEVG compliance was manipulated by computationally tuning its layered composition or by manipulating a crosslinking agent (genipin). In particular, these three acelluluar TEVGs were compared: a compliance-matched graft (CM_{gel} - high gelatin content), a hypocompliant PCL graft ($HYPO_{pcl}$ - high polycaprolactone content), and a hypocompliant genipin graft ($HYPO_{gen}$ - equivalent composition as CM_{gel} but hypocompliant via increased genipin crosslinking). All constructs were implanted interpositionally into

the abdominal aorta of 21 sprague Dawley rats (n=7, males=11, females=10) for 28 days, imaged in vivo using ultrasound, explanted, and assessed for remodeling using immunofluorescence and two photon excitation fluorescence imaging.

Compliance-matched grafts maintained their compliance compared to the hypocompliant grafts through 4 weeks ($p<0.05$). Construct degradation and cellular infiltration was increased in the CM_{gel} and $HYPO_{gen}$ TEVGs. Contractile smooth muscle cell markers in the proximal anastomosis of the graft were increased in the CM_{gel} group compared to the $HYPO_{pcl}$ ($p=0.007$) and $HYPO_{gen}$ grafts ($p=0.04$). Both hypocompliant grafts also had an increased pro-inflammatory response (increased ratio of CD163 to CD86 in the mid-axial location) compared to the CM_{gel} group. Our results suggest that compliance matching using a computational optimization approach leads to an improved acute (28 day) remodeling of TEVGs.

5.2.2 Chapter 3: Modulating TGFβ2 Elution Alters the Acute Remodeling of a Compliance-Matched Tissue Engineered Vascular Graft

In chapter 3, TGFβ2 is incorporated into the CM_{gel} and $HYPO_{pcl}$ TEVGs to promote cellular infiltration. TGFβ2 is a cytokine that plays a vital role in vascular remodeling and cell cycle regulation, SMCs. In this work, electrospun compliance-matched and hypocompliant TGFβ2 eluting TEVGs were implanted into Sprague Dawley rats for 5 days to observe SMC infiltration and ECM production. TEVGs were fabricated using a combined computational and experimental approach to be either compliance-matched or twice as stiff as rat aorta (hypocompliant). TGFβ2 concentrations of 0, 10, 100 ng/mg were added to both graft types (n=3 in each group) and imaged in vivo using ultrasound. Histological markers (SMC, macrophage, collagen, and elastin) were evaluated following explantation at 5 days.

In vivo ultrasound showed that the compliance-matched TEVGs became stiffer as TGFβ2 increased (100 ng/mg TEVGS compared to rat aorta, $p<0.01$) while all hypocompliant grafts remained stiffer than control rat aorta. In vivo velocity and diameter were also not significantly different than control vessels. For histology, the compliance-matched 10 ng/mg group had an elevated SMC signal (myosin heavy chain) compared to the 0 and 100 ng/mg grafts

(p=0.0009 & 0.0006). Compliance-matched TEVGs containing 100 ng/mg TGFβ2 had an increase in collagen production ($p<0.01$), an increase in general immune response ($p<0.05$), and a decrease in SMC infiltration to the 0 and 10 ng/mg groups. All hypocompliant groups were found to be similar, suggesting a lower rate of TGFβ2 release in these TEVGs. Our results suggest that TGFβ2 can modulates in vivo SMC phenotype over an acute time point, which is consistent with our prior in vitro work.

5.2.3 Chapter 4: Tracking delivery of a drug surrogate in the porcine coronary artery using photoacoustic imaging and spectroscopy

In chapter 4, we demonstrate real-time photoacoustic imaging and spectroscopy (PAIS) using a wavelength-tunable visible laser and clinical ultrasound scanner to track cardiac drug delivery. The photoacoustic signal was initially calibrated using porcine myocardial samples soaked with a known concentration of a drug surrogate (DiI). Next, an in situ coronary artery was perfused with DiI for 20 minutes and imaged to monitor dye transport in the tissue. Finally, a partially DiI-coated stent was inserted into the porcine brachiocephalic trunk for imaging. The photoacoustic signal was proportional to the DiI concentration between 2.4 and 120 μg/ml, and the dye was detected over 1.5 mm from the targeted coronary vessel. Photoacoustic imaging was also able to differentiate the DiI-coated portion of the stent from the uncoated region. These results suggest that PAIS can track drug delivery to cardiac tissue and detect drugs loaded onto a stent with sub-mm precision. Future work using PAIS may help improve TEVG and DES design and reduce the probability of restenosis.

5.3 Future Work and Limitations

This dissertation's work is an initial step towards evaluating drug delivery and compliance's affect on vascular graft design. This work has helped establish a framework for future studies in vivo and ex vivo work in the soft tissue biomechanics laboratory. This section of the dissertation will be devoted towards the future direction of this work and the limitations.

A primary component of this dissertation is the compliance of the vascular graft. As stated throughout this work, a hypocompliant TEVG may disrupt the hemodynmaical environment leading to intimal hyperplasia and ultimately causing loss of patency in the vessel. The work in aim 1 was an initial attempt to isolate the effects of compliance by comparing two hypocompliant controls (composition and crosslinking concentration) to a rat aorta compliance-matched TEVG. The effects of compliance in this study could only be set apart when both hypocompliant grafts were similar and the compliance-matched graft was different. This study took a basic approach to evaluating compliance through composition and crosslinking agent, while there are many other methods that could be used. For example, another method to vary compliance could be through the modification of the construct's thickness, increased crosslinking duration, or the choice of TEVG material. These aforementioned methods could be used in conjunction with this work to further isolate the effects of compliance. This dissertation helped to demonstrate the underlying hypothesis, but longer time points may demonstrate such outcomes as a lower patency and increased intimal hyperplasia in the hypocompliant grafts and increased neovessel formation in the compliant matched grafts.

In aim 2, the elution of TGFβ2 from the CM_{gel} and $HYPO_{pcl}$ was evaluated in vivo using a rat animal model for 5 days. While the results from this study were encouraging with results matching prior in vitro work, the limited time points and sample size may have limited the overall impact of the work. Specifically, the sample size of n=3 should be expanded to n=7 to increase the power between each group. The duration of the study should also be increased to include time points at one and three months. The longer time points will allow help clarify the potential benefit of the growth factor. For example, at one and three months there will be increased ECM deposition and cellular infiltration. We would expect there to be an increase in collagen and neovessel formation in the low TGFβ2 concentration group. On the other hand, prolonged or exaggerated TGFβ2 release could be detrimental to the construct as demonstrated in vascular injuries and cancer. Finding a balance between TGFβ2 release and TEVG remodeling will be vital to the success of the implant.

Another future direction with this TGFβ2 work would be to modify the release and

concentration. TGFβ2 could be incorporated into a microparticle and the release could be modified as shown in the work by Jhunjhunwala et al. using TGFβ1 [102]. The current working hypothesis for TGFβ2 release would be to have a low release early to promote cellular infiltration and a high short release later on to promote collagen development. Another simple method to increase TGFβ2 release would be to modify the crosslinking method. Currently, each construct is soak in genipin for 24 hours which, could cause any unbound or loose TGFβ2 to be eluted into the solution. This problem could be fixed by modifying the cross linking method to switch to ultraviolet light, vapor, chemical, or plasma treatment [108].

For both aims 1 and 2, the rat was the primary focus for evaluating the remodeling of a TEVG, but there are some limitations. While the rat offers a high throughput model to test new ideas and larger groups, it lacks the hemodynamic, clotting, length implantation, and immune reaction seen in humans. Moving towards a larger animal can help to overcome some of these challenges and move the TEVG closer towards a clinic trial. For TEVGs especially, the sheep carotid model is one of the best choices due to hemodynamics, clotting, and the extended length (>5 cm) [30]. We have taken the next step and implanted our HYPO$_{pcl}$ into a sheep carotid for 1 day. This study was cut short due to a surgical error that damaged the vagus nerve of the sheep which disrupted the food digestion process and caused the animal to be sacrificed. An image of the implanted construct is show in (**Figure 22**. The graft was still patent at one day and this was confirmed by ultrasound. Initial histology demonstrated no sign of platelet buildup or formation of a thrombus. In future, we hope that this preliminary testing can be used as a stepping stone for future sheep testing.

In aim 3 of this dissertation work, we demonstrated that PA imaging has the potential to track drug delivery and construct degradation. This method specifically evaluated the diffusion of DiI into the porcine coronary tissue and myocardium. While the results of this study are more of a proof of concept, this work demonstrates how important PA imaging could be in future work and the translatability of this method. PA imaging offers the ability to track cellular migration, construction degradation, and drug elution in a TEVG or vascular implant. For example, this method could be incorporated by adding a unique fluorophore to the construct, drug, or cells and tracking their intensity. The TEVG will start with an initial

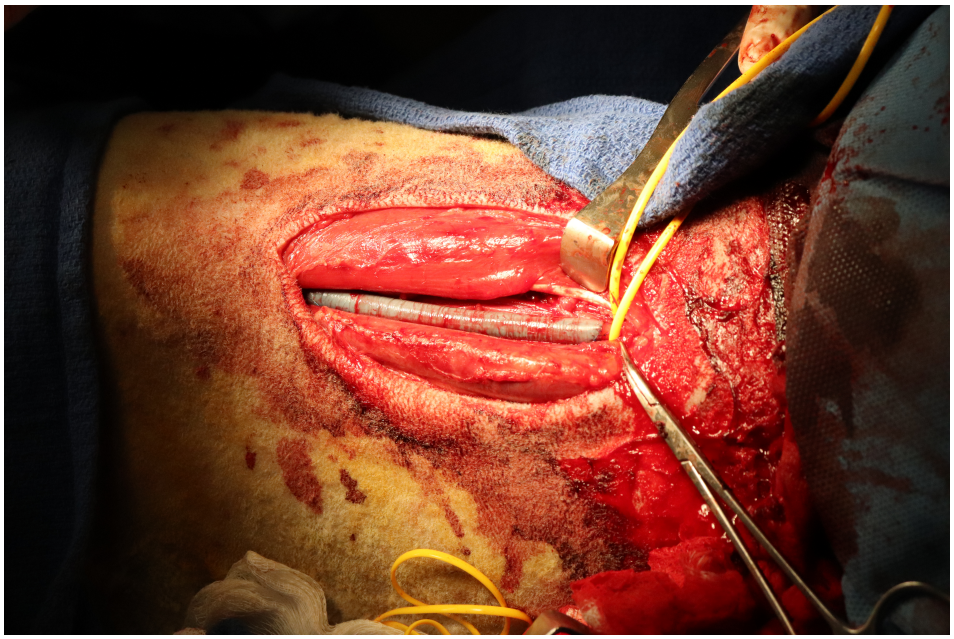

Figure 22: The $HYPO_{pcl}$ TEVG (blue) implanted into the sheep carotid. The graft was 9 cm in length and had a wall thickness of 400 μm.

absorbance and over time the user will PA image the construct and compare the results to the original values. A decrease in the absorbance intensity could signal a release of drug, the construct degraded, or cellular death depending on the tagged component. The ideal fluorophore would be in the near infrared region to help reduce intrinsic absorber in the tissue. The absorbance intensity from the fluorophore will demonstrate how much degradation or drug delivery has occurred from a loss of signal. The ideal fluorophore would be in the near infrared region to help reduce intrinsic absorber in the tissue.

PA imaging also has the ability to be used in other animals models besides the porcine. The ideal animal model for imaging a TEVG/vascular implant would be a large vessel near the surface. The rat animal model used in aims 1 and 2 would not visable with the current PA imaging setup in aim 3 as the resolution of the system is too large, 300 μm. The ultrasound probe would need to be increase from 7.1 Mhz to 60 Mhz in order to view the TEVG which was on average a 100 μm. The 7.1 Mhz setup in aim 3 could be used for imaging the sheep carotid discussed in the this section, but it would be recommended that

the probe be increased to around 30 Mhz. It is recommended that future work should use a higher Mhz probe to increase the resolution and make this method more viable.

5.4 Conclusions

Previous work has demonstrated that a stiff or hypocompliant TEVG negatively affect vascular remodel and patency, but has been unable to tune compliance to a specific value. In this work, we demonstrate that our computational/experimental approach can fine tune the compliance of a vascular graft by composition and takes it a step further by modifying compliance by crosslinking as well. We confirm that matching a TEVG to the native vasculature will positively impact graft remodeling. Specifically, a compliance-matched construct promotes an increase in SMC, positive macrophage remodeling, and increased collagen content in the TEVG.

To promote earlier SMC infiltration into the TEVG and collagen deposition, we infused the compliance-matched and hypocompliant constructs with varying concentration of TGFβ2. This growth factor has previously shown that it can modulate SMC phenotype depending on the concentration. Specifically, at low TGFβ2 concentration this factor will promote cellular migration and proliferation, while at higher concentrations it arrests cellular growth that promotes collagen development. This TGFβ2 response was confirmed in our compliance-matched scaffolds. One surprising result from the inclusion of TGFβ2 in the compliance-matched scaffolds was that as concentration increased the scaffold became stiffer. While the compliance-matched scaffolds demonstrated the majority of significant results, all TGFβ2 concentrations in the hypocompliant constructs had no differences between any groups in the study. This lack of differences seen in the hypocompliant constructs demonstrated the importance of scaffold degradation in the release of TGFβ2. For example, the compliance-matched construct in aim one had over 70% degradation by 4 weeks compared to about 30% seen in the hypocompliant grafts. Digging deeper into previous work by Ardila et al., she showed that the compliance-matched scaffold should have over a 40x higher release than the hypocompliant construct. This lack of release of TGFβ2 in the

hypocompliant scaffolds accounts for the lack of differences in the results.

Moving forward, this dissertation has also developed a method to evaluate drug delivery and track construct degradation noninvasively using photoacoustic imaging and spectroscopy. By including a known absorbing agent into the scaffold or drug, the user would be able to identify drug release or scaffold degradation. This method would be most feasible in a larger animal due to limited spatial resolution of the ultrasound technology. We hope that this work has inspired the reader and promotes more research in the field of photoacoustic imaging and TEVG.

6.0 Appendix

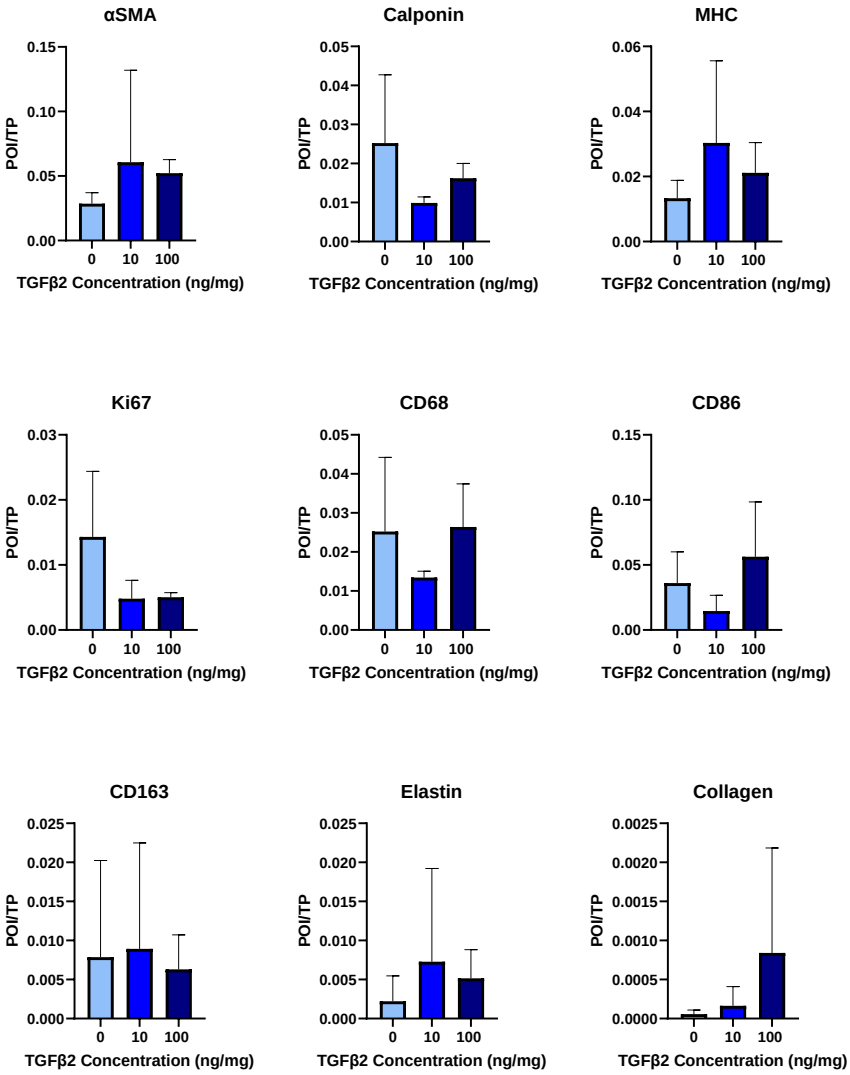

Figure S1: Hypocompliant cross sectional immunohistochemistry quantification of αSMA, Calponin, MHC, Ki67, CD68 (pan macrophage), CD86 (M1), CD163 (M2), elastin, and collagen signal

.

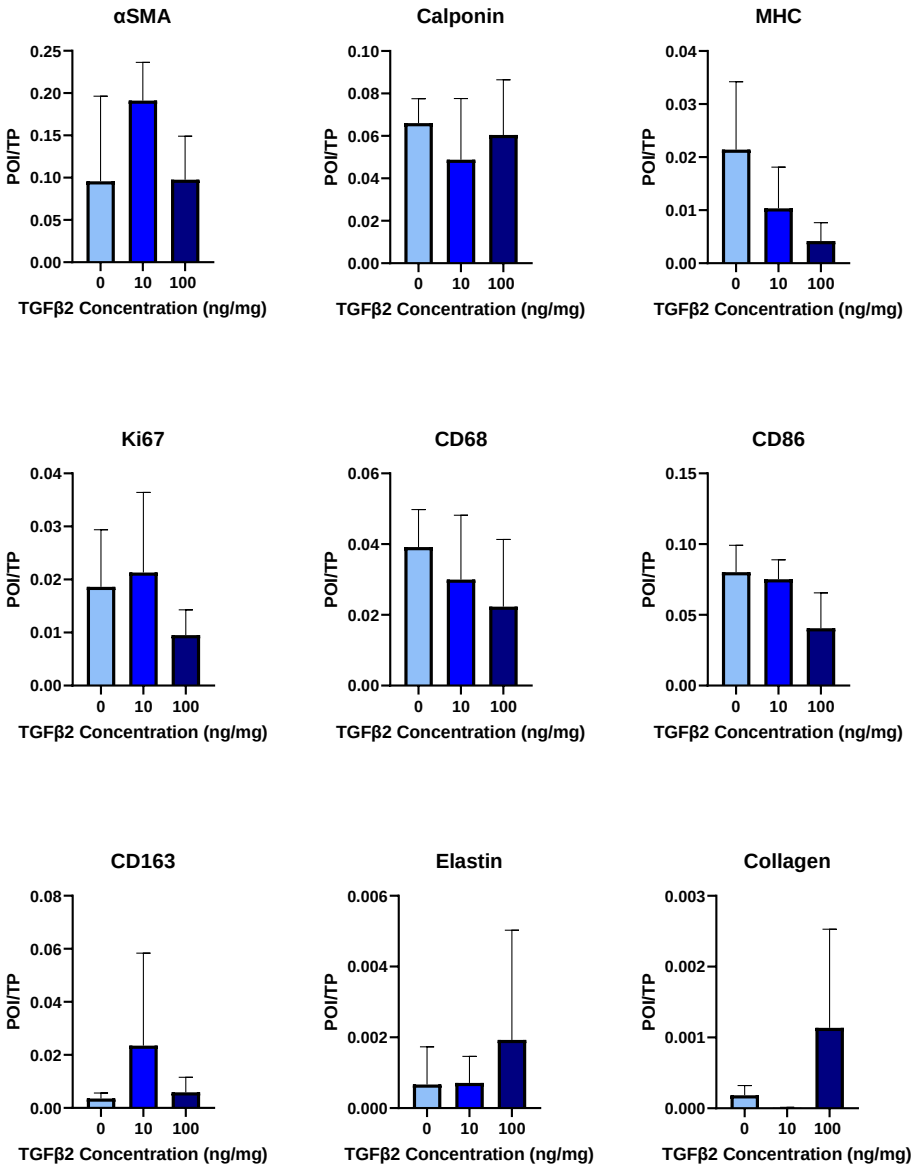

Figure S2: Hypocompliant longitudinal immunohistochemistry quantification of αSMA, Calponin, MHC, Ki67, CD68 (pan macrophage), CD86 (M1), CD163 (M2), elastin, and collagen signal

.

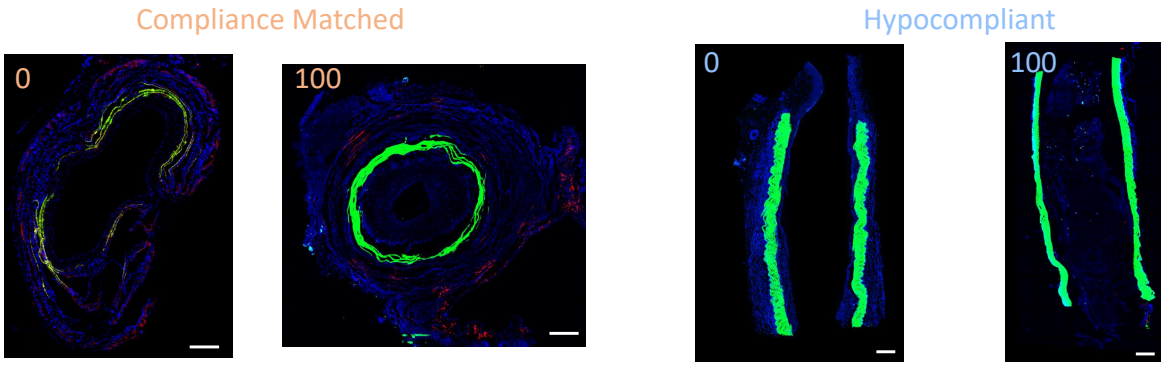

Figure S3: Hypocompliant cross sectional immunohistochemistry quantification of αSMA, Calponin, MHC, Ki67, CD68 (pan macrophage), CD86 (M1), CD163 (M2), elastin, and collagen signal

.

Bibliography

[1] C. D. Fryar, T. C. Chen, and X. Li, "Prevalence of uncontrolled risk factors for cardiovascular disease: United States, 1999-2010," *NCHS Data Brief*, pp. 1–8, Aug 2012.

[2] E. J. Benjamin, P. Muntner, A. Alonso, M. S. Bittencourt, C. W. Callaway, and A. P. Carson, "Heart Disease and Stroke Statistics-2019 Update: A Report From the American Heart Association," *Circulation*, vol. 139, pp. e56–e528, 03 2019.

[3] J. Shu and G. Santulli, "Update on peripheral artery disease: Epidemiology and evidence-based facts," *Atherosclerosis*, vol. 275, pp. 379–381, 08 2018.

[4] P. Song, D. Rudan, Y. Zhu, and F. J. I. Fowkes, "Global, regional, and national prevalence and risk factors for peripheral artery disease in 2015: an updated systematic review and analysis," *Lancet Glob Health*, vol. 7, pp. e1020–e1030, 08 2019.

[5] S. S. Virani, A. Alonso, E. J. Benjamin, M. S. Bittencourt, C. W. Callaway, and A. P. Carson, "Heart Disease and Stroke Statistics-2020 Update: A Report From the American Heart Association," *Circulation*, vol. 141, pp. e139–e596, 03 2020.

[6] S. Windecker and B. Meier, "Intervention in coronary artery disease," *Heart*, vol. 83, pp. 481–490, Apr 2000.

[7] K. M. Lekshmi, H. L. Che, C. S. Cho, and I. K. Park, "Drug- and Gene-eluting Stents for Preventing Coronary Restenosis," *Chonnam Med J*, vol. 53, pp. 14–27, Jan 2017.

[8] S. Borhani, S. Hassanajili, S. H. Ahmadi Tafti, and S. Rabbani, "Cardiovascular stents: overview, evolution, and next generation," *Prog Biomater*, vol. 7, pp. 175–205, Sep 2018.

[9] B. McNichols, J. R. Spratt, J. George, S. Rizzi, E. W. Manning, and K. Park, "Coronary Artery Bypass: Review of Surgical Techniques and Impact on Long-Term Revascularization Outcomes," *Cardiol Ther*, vol. 10, pp. 89–109, Jun 2021.

[10] H. Zhang, Z. W. Wang, H. B. Wu, X. P. Hu, Z. Zhou, and P. Xu, "Radial artery graft vs. saphenous vein graft for coronary artery bypass surgery : which conduit offers better efficacy?," *Herz*, vol. 39, pp. 458–465, Jun 2014.

[11] A. J. Lusis, "Atherosclerosis," *Nature*, vol. 407, pp. 233–241, Sep 2000.

[12] M. Rafieian-Kopaei, M. Setorki, M. Doudi, A. Baradaran, and H. Nasri, "Atherosclerosis: process, indicators, risk factors and new hopes," *Int J Prev Med*, vol. 5, pp. 927–946, Aug 2014.

[13] S. Pashneh-Tala, S. MacNeil, and F. Claeyssens, "The Tissue-Engineered Vascular Graft-Past, Present, and Future," *Tissue Eng Part B Rev*, vol. 22, pp. 68–100, Feb 2016.

[14] Y. Matsuzaki, K. John, T. Shoji, and T. Shinoka, "The Evolution of Tissue Engineered Vascular Graft Technologies: From Preclinical Trials to Advancing Patient Care," *Appl Sci (Basel)*, vol. 9, Apr 2019.

[15] P. W. Serruys, A. T. Ong, L. A. van Herwerden, J. E. Sousa, A. Jatene, J. J. Bonnier, J. P. Sch?nberger, N. Buller, R. Bonser, C. Disco, B. Backx, P. G. Hugenholtz, B. G. Firth, and F. Unger, "Five-year outcomes after coronary stenting versus bypass surgery for the treatment of multivessel disease: the final analysis of the Arterial Revascularization Therapies Study (ARTS) randomized trial," *J. Am. Coll. Cardiol.*, vol. 46, pp. 575–581, Aug 2005.

[16] A. S. Go, D. Mozaffarian, V. L. Roger, and E. J. Benjamin, "Heart disease and stroke statistics–2014 update: a report from the American Heart Association," *Circulation*, vol. 129, pp. e28–e292, Jan 2014.

[17] J. P. Vacanti and R. Langer, "Tissue engineering: the design and fabrication of living replacement devices for surgical reconstruction and transplantation," *Lancet*, vol. 354 Suppl 1, pp. I32–34, Jul 1999.

[18] P. A. Gunatillake and R. Adhikari, "Biodegradable synthetic polymers for tissue engineering," *Eur Cell Mater*, vol. 5, pp. 1–16, May 2003.

[19] M. Jafari, Z. Paknejad, M. R. Rad, S. R. Motamedian, M. J. Eghbal, N. Nadjmi, and A. Khojasteh, "Polymeric scaffolds in tissue engineering: a literature review," *J Biomed Mater Res B Appl Biomater*, vol. 105, pp. 431–459, 02 2017.

[20] S. de Valence, J. C. Tille, D. Mugnai, W. Mrowczynski, R. Gurny, M. Möller, and B. H. Walpoth, "Long term performance of polycaprolactone vascular grafts in a rat abdominal aorta replacement model," *Biomaterials*, vol. 33, pp. 38–47, Jan 2012.

[21] D. P. Speer, M. Chvapil, C. D. Eskelson, and J. Ulreich, "Biological effects of residual glutaraldehyde in glutaraldehyde-tanned collagen biomaterials," *J. Biomed. Mater. Res.*, vol. 14, pp. 753–764, Nov 1980.

[22] J. E. Gough, C. A. Scotchford, and S. Downes, "Cytotoxicity of glutaraldehyde crosslinked collagen/poly(vinyl alcohol) films is by the mechanism of apoptosis," *J. Biomed. Mater. Res.*, vol. 61, pp. 121–130, Jul 2002.

[23] K. M. Kim, G. A. Herrera, and H. D. Battarbee, "Role of glutaraldehyde in calcification of porcine aortic valve fibroblasts," *Am. J. Pathol.*, vol. 154, pp. 843–852, Mar 1999.

[24] J. Chanda, K. Kondoh, K. Ijima, M. Matsukawa, and R. Kuribayashi, "In vitro and in vivo calcification of vascular bioprostheses," *Biomaterials*, vol. 19, no. 18, pp. 1651–6, 1998.

[25] G. Golomb, F. J. Schoen, M. S. Smith, J. Linden, M. Dixon, and R. J. Levy, "The role of glutaraldehyde-induced cross-links in calcification of bovine pericardium used in cardiac valve bioprostheses," *Am J Pathol*, vol. 127, no. 1, pp. 122–30, 1987.

[26] J. S. Yoo, Y. J. Kim, S. H. Kim, and S. H. Choi, "Study on genipin: a new alternative natural crosslinking agent for fixing heterograft tissue," *Korean J Thorac Cardiovasc Surg*, vol. 44, no. 3, pp. 197–207, 2011.

[27] D. C. Ardila, E. Tamimi, T. Doetschman, W. R. Wagner, and J. P. Vande Geest, "Modulating smooth muscle cell response by the release of TGFÎ2 from tubular scaffolds for vascular tissue engineering," *J Control Release*, vol. 299, pp. 44–52, 04 2019.

[28] E. A. Tamimi, D. C. Ardila, B. D. Ensley, R. S. Kellar, and J. Vande Geest, "Computationally optimizing the compliance of multilayered biomimetic tissue engineered vascular grafts," *Journal of Biomechanical Engineering*, vol. 141(2019), Feb 2019.

[29] D. C. Ardila, E. Tamimi, F. L. Danford, D. G. Haskett, R. S. Kellar, T. Doetschman, and J. P. Vande Geest, "TGFβ2 differentially modulates smooth muscle cell proliferation and migration in electrospun gelatin-fibrinogen constructs," *Biomaterials*, vol. 37, pp. 164–173, Jan 2015.

[30] D. D. Swartz and S. T. Andreadis, "Animal models for vascular tissue-engineering," *Curr Opin Biotechnol*, vol. 24, no. 5, pp. 916–25, 2013.

[31] M. J. Byrom, P. G. Bannon, G. H. White, and M. K. Ng, "Animal models for the assessment of novel vascular conduits," *J Vasc Surg*, vol. 52, pp. 176–195, Jul 2010.

[32] K. J. Furdella, S. Higuchi, A. Behrangzade, K. Kim, W. R. Wagner, and J. P. Vande Geest, "In-vivo assessment of a tissue engineered vascular graft computationally optimized for target vessel compliance," *Acta Biomater*, vol. 123, pp. 298–311, 03 2021.

[33] W. M. Abbott, J. Megerman, J. E. Hasson, G. Litalien, and D. F. Warnock, "Effect of compliance mismatch on vascular graft patency," *Journal of Vascular Surgery*, vol. 5, no. 2, pp. 376–382, 1987.

[34] S. F. Stewart and D. J. Lyman, "Effects of an artery/vascular graft compliance mismatch on protein transport: a numerical study," *Ann Biomed Eng*, vol. 32, pp. 991–1006, Jul 2004.

[35] W. Trubel, H. Schima, A. Moritz, F. Raderer, A. Windisch, R. Ullrich, U. Windberger, U. Losert, and P. Polterauer, "Compliance mismatch and formation of distal anastomotic intimal hyperplasia in externally stiffened and lumen-adapted venous grafts," *Eur J Vasc Endovasc Surg*, vol. 10, pp. 415–423, Nov 1995.

[36] M. Zhu, Y. Wu, W. Li, X. Dong, H. Chang, K. Wang, P. Wu, J. Zhang, G. Fan, L. Wang, J. Liu, H. Wang, and D. Kong, "Biodegradable and elastomeric vascular grafts enable vascular remodeling," *Biomaterials*, vol. 183, pp. 306–318, 11 2018.

[37] V. A. Kumar, J. M. Caves, C. A. Haller, E. Dai, L. Liu, S. Grainger, and E. L. Chaikof, "Acellular vascular grafts generated from collagen and elastin analogs," *Acta Biomater*, vol. 9, pp. 8067–8074, Sep 2013.

[38] N. L'Heureux, N. Dusserre, G. Konig, B. Victor, P. Keire, T. N. Wight, N. A. Chronos, A. E. Kyles, C. R. Gregory, G. Hoyt, R. C. Robbins, and T. N. McAllister, "Human tissue-engineered blood vessels for adult arterial revascularization," *Nat. Med.*, vol. 12, pp. 361–365, Mar 2006.

[39] P. Gupta, K. L. Lorentz, D. G. Haskett, E. M. Cunnane, A. K. Ramaswamy, J. S. Weinbaum, D. A. Vorp, and B. B. Mandal, "Bioresorbable silk grafts for small diame-

ter vascular tissue engineering applications: In vitro and in vivo functional analysis," *Acta Biomater*, vol. 105, pp. 146–158, Mar 2020.

[40] K. W. Lee, P. S. Gade, L. Dong, Z. Zhang, A. M. Aral, J. Gao, X. Ding, C. E. T. Stowell, M. U. Nisar, K. Kim, D. P. Reinhardt, M. G. Solari, V. S. Gorantla, A. M. Robertson, and Y. Wang, "A biodegradable synthetic graft for small arteries matches the performance of autologous vein in rat carotid arteries," *Biomaterials*, vol. 181, pp. 67–80, 10 2018.

[41] R. M. Nezarati, M. B. Eifert, D. K. Dempsey, and E. Cosgriff-Hernandez, "Electrospun vascular grafts with improved compliance matching to native vessels," *J. Biomed. Mater. Res. Part B Appl. Biomater.*, vol. 103, pp. 313–323, Feb 2015.

[42] X. Wang, P. Lin, Q. Yao, and C. Chen, "Development of small-diameter vascular grafts," *World J Surg*, vol. 31, pp. 682–689, Apr 2007.

[43] J. G. Nemeno-Guanzon, S. Lee, J. R. Berg, Y. H. Jo, J. E. Yeo, B. M. Nam, Y. G. Koh, and J. I. Lee, "Trends in tissue engineering for blood vessels," *J. Biomed. Biotechnol.*, vol. 2012, p. 956345, 2012.

[44] R. Y. Kannan, H. J. Salacinski, P. E. Butler, G. Hamilton, and A. M. Seifalian, "Current status of prosthetic bypass grafts: a review," *J. Biomed. Mater. Res. Part B Appl. Biomater.*, vol. 74, pp. 570–581, Jul 2005.

[45] E. Tamimi, D. C. Ardila, D. G. Haskett, T. Doetschman, M. J. Slepian, R. S. Kellar, and J. P. Vande Geest, "Biomechanical Comparison of Glutaraldehyde-Crosslinked Gelatin Fibrinogen Electrospun Scaffolds to Porcine Coronary Arteries," *J Biomech Eng*, vol. 138(1)(2016), p. 061003, Jan 2016.

[46] D. Haskett, E. Speicher, M. Fouts, D. Larson, M. Azhar, U. Utzinger, and J. Vande Geest, "The effects of angiotensin II on the coupled microstructural and biomechanical response of C57BL/6 mouse aorta," *J Biomech*, vol. 45, pp. 772–779, Mar 2012.

[47] D. Haskett, M. Azhar, U. Utzinger, and J. P. V. Geest, "Progressive alterations in microstructural organization and biomechanical response in the apoe mouse model of aneurysm," *Biomatter*, vol. 3, no. 3, p. e24648, 2013.

[48] D. Haskett, J. J. Doyle, C. Gard, H. Chen, C. Ball, M. A. Estabrook, A. C. Encinas, H. C. Dietz, U. Utzinger, J. P. Vande Geest, and M. Azhar, "Altered tissue behavior of

a non-aneurysmal descending thoracic aorta in the mouse model of Marfan syndrome," *Cell Tissue Res.*, vol. 347, pp. 267–277, Jan 2012.

[49] J. T. Keyes, D. G. Haskett, U. Utzinger, M. Azhar, and J. P. Vande Geest, "Adaptation of a planar microbiaxial optomechanical device for the tubular biaxial microstructural and macroscopic characterization of small vascular tissues," *Journal of Biomechanical Engineering*, vol. 133, no. 7, pp. 075001–075001, 2011.

[50] J. T. Keyes, D. R. Lockwood, U. Utzinger, L. G. Montilla, R. S. Witte, and J. P. Vande Geest, "Comparisons of planar and tubular biaxial tensile testing protocols of the same porcine coronary arteries," *Annals of Biomedical Engineering*, vol. 41, no. 7, pp. 1579–1591, 2013.

[51] J. T. Keyes, S. M. Borowicz, J. H. Rader, U. Utzinger, M. Azhar, and J. P. Vande Geest, "Design and demonstration of a microbiaxial optomechanical device for multiscale characterization of soft biological tissues with two-photon microscopy," *Microsc. Microanal.*, vol. 17, pp. 167–175, Apr 2011.

[52] S. Harrison, E. Tamimi, J. Uhlorn, T. Leach, and J. P. Vande Geest, "Computationally optimizing the compliance of a biopolymer based tissue engineered vascular graft," *Journal of Biomechanical Engineering*, vol. 138, no. 1, p. 0145051-0145055, 2016.

[53] N. R. Tai, H. J. Salacinski, A. Edwards, G. Hamilton, and A. M. Seifalian, "Compliance properties of conduits used in vascular reconstruction," *Br J Surg*, vol. 87, pp. 1516–1524, Nov 2000.

[54] J. Guan, M. S. Sacks, E. J. Beckman, and W. R. Wagner, "Biodegradable poly(ether ester urethane)urea elastomers based on poly(ether ester) triblock copolymers and putrescine: synthesis, characterization and cytocompatibility," *Biomaterials*, vol. 25, pp. 85–96, Jan 2004.

[55] M. Y. Park, S. E. Jung, J. Y. Byun, J. H. Kim, and G. E. Joo, "Effect of beam-flow angle on velocity measurements in modern doppler ultrasound systems," *American Journal of Roentgenology*, vol. 198, no. 5, pp. 1139–1143, 2012.

[56] S. R. Peyton, P. D. Kim, C. M. Ghajar, D. Seliktar, and A. J. Putnam, "The effects of matrix stiffness and RhoA on the phenotypic plasticity of smooth muscle cells in a 3-D biosynthetic hydrogel system," *Biomaterials*, vol. 29, pp. 2597–2607, Jun 2008.

[57] B. Yi, Y. Shen, H. Tang, X. Wang, B. Li, and Y. Zhang, "Stiffness of Aligned Fibers Regulates the Phenotypic Expression of Vascular Smooth Muscle Cells," *ACS Appl Mater Interfaces*, vol. 11, pp. 6867–6880, Feb 2019.

[58] P. F. Sanchez, E. M. Brey, and J. C. Briceno, "Endothelialization mechanisms in vascular grafts," *J Tissue Eng Regen Med*, vol. 12, pp. 2164–2178, 11 2018.

[59] S. K. Norouzi and A. Shamloo, "Bilayered heparinized vascular graft fabricated by combining electrospinning and freeze drying methods," *Mater Sci Eng C Mater Biol Appl*, vol. 94, pp. 1067–1076, Jan 2019.

[60] K. T. Shalumon, S. Deepthi, M. S. Anupama, S. V. Nair, R. Jayakumar, and K. P. Chennazhi, "Fabrication of poly (L-lactic acid)/gelatin composite tubular scaffolds for vascular tissue engineering," *Int. J. Biol. Macromol.*, vol. 72, pp. 1048–1055, Jan 2015.

[61] M. Zhu, Z. Wang, J. Zhang, L. Wang, X. Yang, J. Chen, G. Fan, S. Ji, C. Xing, K. Wang, Q. Zhao, Y. Zhu, D. Kong, and L. Wang, "Circumferentially aligned fibers guided functional neoartery regeneration in vivo," *Biomaterials*, vol. 61, pp. 85–94, 2015.

[62] Y. Pan, X. Zhou, Y. Wei, Q. Zhang, T. Wang, M. Zhu, W. Li, R. Huang, R. Liu, J. Chen, G. Fan, K. Wang, D. Kong, and Q. Zhao, "Small-diameter hybrid vascular grafts composed of polycaprolactone and polydioxanone fibers," *Sci Rep*, vol. 7, no. 1, p. 3615, 2017.

[63] J. Y. Wong, A. Velasco, P. Rajagopalan, and Q. Pham, "Directed movement of vascular smooth muscle cells on gradient-compliant hydrogels," *Langmuir*, vol. 19, no. 5, pp. 1908–1913, 2003.

[64] H. G. Sundararaghavan, G. A. Monteiro, N. A. Lapin, Y. J. Chabal, J. R. Miksan, and D. I. Shreiber, "Genipin-induced changes in collagen gels: correlation of mechanical properties to fluorescence," *J Biomed Mater Res A*, vol. 87, pp. 308–320, Nov 2008.

[65] G. Fessel, J. Cadby, S. Wunderli, R. van Weeren, and J. G. Snedeker, "Dose- and time-dependent effects of genipin crosslinking on cell viability and tissue mechanics - toward clinical application for tendon repair," *Acta Biomater*, vol. 10, pp. 1897–1906, May 2014.

[66] R. A. Allen, W. Wu, M. Yao, D. Dutta, X. Duan, T. N. Bachman, H. C. Champion, D. B. Stolz, A. M. Robertson, K. Kim, J. S. Isenberg, and Y. Wang, "Nerve regeneration and elastin formation within poly(glycerol sebacate)-based synthetic arterial grafts one-year post-implantation in a rat model," *Biomaterials*, vol. 35, no. 1, pp. 165–73, 2014.

[67] S. Timraz, R. Rezgui, S. M. Boularaoui, and J. C. M. Teo, "Stiffness of extracellular matrix components modulates the phenotype of human smooth muscle cells in vitro and allows for the control of properties of engineered tissues," *Procedia Engineering*, vol. 110, pp. 29–36, 2015.

[68] S. A. Xie, T. Zhang, J. Wang, F. Zhao, Y. P. Zhang, W. J. Yao, S. S. Hur, Y. T. Yeh, W. Pang, L. S. Zheng, Y. B. Fan, W. Kong, X. Wang, J. J. Chiu, and J. Zhou, "Matrix stiffness determines the phenotype of vascular smooth muscle cell in vitro and in vivo: Role of dna methyltransferase 1," *Biomaterials*, vol. 155, pp. 203–216, 2018.

[69] Y. Wang, J. Bao, X. Wu, Q. Wu, Y. Li, Y. Zhou, L. Li, and H. Bu, "Genipin crosslinking reduced the immunogenicity of xenogeneic decellularized porcine whole-liver matrices through regulation of immune cell proliferation and polarization," *Sci Rep*, vol. 6, p. 24779, Apr 2016.

[70] S. de Valence, J. C. Tille, D. Mugnai, W. Mrowczynski, R. Gurny, M. Moller, and B. H. Walpoth, "Long term performance of polycaprolactone vascular grafts in a rat abdominal aorta replacement model," *Biomaterials*, vol. 33, no. 1, pp. 38–47, 2012.

[71] M. D. Rekhter, "Collagen synthesis in atherosclerosis: too much and not enough," *Cardiovasc Res*, vol. 41, pp. 376–384, Feb 1999.

[72] E. Adiguzel, P. J. Ahmad, C. Franco, and M. P. Bendeck, "Collagens in the progression and complications of atherosclerosis," *Vasc Med*, vol. 14, pp. 73–89, Feb 2009.

[73] T. Yeung, P. C. Georges, L. A. Flanagan, B. Marg, M. Ortiz, M. Funaki, N. Zahir, W. Ming, V. Weaver, and P. A. Janmey, "Effects of substrate stiffness on cell morphology, cytoskeletal structure, and adhesion," *Cell Motil Cytoskeleton*, vol. 60, no. 1, pp. 24–34, 2005.

[74] C. M. Lo, H. B. Wang, M. Dembo, Y. L. Wang, and Y. L. Wang, "Cell movement is guided by the rigidity of the substrate," *Biophys. J.*, vol. 79, pp. 144–152, Jul 2000.

[75] Z. Wang, W. Zheng, Y. Wu, J. Wang, X. Zhang, K. Wang, Q. Zhao, D. Kong, T. Ke, and C. Li, "Differences in the performance of pcl-based vascular grafts as abdominal aorta substitutes in healthy and diabetic rats," *Biomater Sci*, vol. 4, no. 10, pp. 1485–92, 2016.

[76] B. Jiang, R. Suen, J. J. Wang, Z. J. Zhang, J. A. Wertheim, and G. A. Ameer, "Mechanocompatible polymer-extracellular-matrix composites for vascular tissue engineering," *Adv Healthc Mater*, vol. 5, no. 13, pp. 1594–605, 2016.

[77] W. Wu, R. A. Allen, and Y. Wang, "Fast-degrading elastomer enables rapid remodeling of a cell-free synthetic graft into a neoartery," *Nat Med*, vol. 18, no. 7, pp. 1148–53, 2012.

[78] Y. Yang, D. Lei, H. Zou, S. Huang, Q. Yang, S. Li, F. L. Qing, X. Ye, Z. You, and Q. Zhao, "Hybrid electrospun rapamycin-loaded small-diameter decellularized vascular grafts effectively inhibit intimal hyperplasia," *Acta Biomater*, vol. 97, pp. 321–332, 2019.

[79] A. Mahara, T. Sakuma, N. Mihashi, T. Moritan, and T. Yamaoka, "Accelerated endothelialization and suppressed thrombus formation of acellular vascular grafts by modifying with neointima-inducing peptide: A time-dependent analysis of graft patency in rat-abdominal transplantation model," *Colloids Surf B Biointerfaces*, vol. 181, pp. 806–813, 2019.

[80] A. Nieponice, L. Soletti, J. Guan, Y. Hong, B. Gharaibeh, T. M. Maul, J. Huard, W. R. Wagner, and D. A. Vorp, "In vivo assessment of a tissue-engineered vascular graft combining a biodegradable elastomeric scaffold and muscle-derived stem cells in a rat model," *Tissue Eng Part A*, vol. 16, no. 4, pp. 1215–23, 2010.

[81] L. Soletti, A. Nieponice, Y. Hong, S. H. Ye, J. J. Stankus, W. R. Wagner, and D. A. Vorp, "In vivo performance of a phospholipid-coated bioerodable elastomeric graft for small-diameter vascular applications," *J Biomed Mater Res A*, vol. 96, no. 2, pp. 436–48, 2011.

[82] E. Pektok, B. Nottelet, J. C. Tille, R. Gurny, A. Kalangos, M. Moeller, and B. H. Walpoth, "Degradation and healing characteristics of small-diameter poly(epsilon-caprolactone) vascular grafts in the rat systemic arterial circulation," *Circulation*, vol. 118, no. 24, pp. 2563–70, 2008.

[83] L. A. Ruiz-Taylor, T. L. Martin, F. G. Zaugg, K. Witte, P. Indermuhle, S. Nock, and P. Wagner, "Monolayers of derivatized poly(L-lysine)-grafted poly(ethylene glycol)

on metal oxides as a class of biomolecular interfaces," *Proc. Natl. Acad. Sci. U.S.A.*, vol. 98, pp. 852–857, Jan 2001.

[84] L. L. Huang-Lee, D. T. Cheung, and M. E. Nimni, "Biochemical changes and cytotoxicity associated with the degradation of polymeric glutaraldehyde derived crosslinks," *J. Biomed. Mater. Res.*, vol. 24, pp. 1185–1201, Sep 1990.

[85] J. E. Gough, C. A. Scotchford, and S. Downes, "Cytotoxicity of glutaraldehyde crosslinked collagen/poly(vinyl alcohol) films is by the mechanism of apoptosis," *J. Biomed. Mater. Res.*, vol. 61, pp. 121–130, Jul 2002.

[86] A. Fernandez-Colino, F. Wolf, S. Rutten, T. Schmitz-Rode, J. C. Rodriguez-Cabello, S. Jockenhoevel, and P. Mela, "Small caliber compliant vascular grafts based on elastin-like recombinamers for in situ tissue engineering," *Front Bioeng Biotechnol*, vol. 7, p. 340, 2019.

[87] K. J. Furdella, R. S. Witte, and J. P. Vande Geest, "Tracking delivery of a drug surrogate in the porcine heart using photoacoustic imaging and spectroscopy," *J Biomed Opt*, vol. 22, p. 41016, 04 2017.

[88] C. Boileau, D. C. Guo, N. Hanna, E. S. Regalado, D. Detaint, L. Gong, M. Varret, and S. K. Prakash, "TGFB2 mutations cause familial thoracic aortic aneurysms and dissections associated with mild systemic features of Marfan syndrome," *Nat Genet*, vol. 44, pp. 916–921, Jul 2012.

[89] N. W. Ramnath, L. J. Hawinkels, P. M. van Heijningen, L. te Riet, M. Paauwe, M. Vermeij, A. H. Danser, R. Kanaar, P. ten Dijke, and J. Essers, "Fibulin-4 deficiency increases TGF- signalling in aortic smooth muscle cells due to elevated TGF-2 levels," *Sci Rep*, vol. 5, p. 16872, Nov 2015.

[90] M. Azhar, K. Brown, C. Gard, H. Chen, S. Rajan, D. A. Elliott, M. V. Stevens, T. D. Camenisch, S. J. Conway, and T. Doetschman, "Transforming growth factor Beta2 is required for valve remodeling during heart development," *Dev Dyn*, vol. 240, pp. 2127–2141, Sep 2011.

[91] T. Doetschman, J. V. Barnett, R. B. Runyan, T. D. Camenisch, R. L. Heimark, H. L. Granzier, S. J. Conway, and M. Azhar, "Transforming growth factor beta signaling in adult cardiovascular diseases and repair," *Cell Tissue Res*, vol. 347, pp. 203–223, Jan 2012.

[92] A. C. Braverman, K. M. Harris, R. J. Kovacs, and B. J. Maron, "Eligibility and Disqualification Recommendations for Competitive Athletes With Cardiovascular Abnormalities: Task Force 7: Aortic Diseases, Including Marfan Syndrome: A Scientific Statement From the American Heart Association and American College of Cardiology," *J Am Coll Cardiol*, vol. 66, pp. 2398–2405, Dec 2015.

[93] I. Toma and T. A. McCaffrey, "Transforming growth factor- and atherosclerosis: interwoven atherogenic and atheroprotective aspects," *Cell Tissue Res*, vol. 347, pp. 155–175, Jan 2012.

[94] S. S. Rensen, P. A. Doevendans, and G. J. van Eys, "Regulation and characteristics of vascular smooth muscle cell phenotypic diversity," *Neth Heart J*, vol. 15, no. 3, pp. 100–108, 2007.

[95] J. A. Beamish, P. He, K. Kottke-Marchant, and R. E. Marchant, "Molecular regulation of contractile smooth muscle cell phenotype: implications for vascular tissue engineering," *Tissue Eng Part B Rev*, vol. 16, pp. 467–491, Oct 2010.

[96] S. Mii, J. A. Ware, and K. C. Kent, "Transforming growth factor-beta inhibits human vascular smooth muscle cell growth and migration," *Surgery*, vol. 114, pp. 464–470, Aug 1993.

[97] L. Engel and U. Ryan, "TGF-beta 1 reverses PDGF-stimulated migration of human aortic smooth muscle cells in vitro," *In Vitro Cell Dev Biol Anim*, vol. 33, pp. 443–451, Jun 1997.

[98] M. A. Moses, M. Klagsbrun, and Y. Shing, "The role of growth factors in vascular cell development and differentiation," *Int Rev Cytol*, vol. 161, pp. 1–48, 1995.

[99] E. L. Low, A. H. Baker, and A. C. Bradshaw, "TGF, smooth muscle cells and coronary artery disease: a review," *Cell Signal*, vol. 53, pp. 90–101, 01 2019.

[100] X. Guo and S. Y. Chen, "Transforming growth factor- and smooth muscle differentiation," *World J Biol Chem*, vol. 3, pp. 41–52, Mar 2012.

[101] K. Kubota, J. Okazaki, O. Louie, K. C. Kent, and B. Liu, "TGF-beta stimulates collagen (I) in vascular smooth muscle cells via a short element in the proximal collagen promoter," *J Surg Res*, vol. 109, pp. 43–50, Jan 2003.

[102] S. Jhunjhunwala, S. C. Balmert, G. Raimondi, E. Dons, E. E. Nichols, A. W. Thomson, and S. R. Little, "Controlled release formulations of IL-2, TGF-1 and rapamycin for the induction of regulatory T cells," *J Control Release*, vol. 159, pp. 78–84, Apr 2012.

[103] K. Ley, "M1 Means Kill; M2 Means Heal," *J Immunol*, vol. 199, pp. 2191–2193, 10 2017.

[104] F. O. Martinez and S. Gordon, "The M1 and M2 paradigm of macrophage activation: time for reassessment," *F1000Prime Rep*, vol. 6, p. 13, 2014.

[105] N. Hibino, D. Mejias, N. Pietris, E. Dean, T. Yi, C. Best, T. Shinoka, and C. Breuer, "The innate immune system contributes to tissue-engineered vascular graft performance," *FASEB J*, vol. 29, pp. 2431–2438, Jun 2015.

[106] C. J. Ferrante and S. J. Leibovich, "Regulation of Macrophage Polarization and Wound Healing," *Adv Wound Care (New Rochelle)*, vol. 1, pp. 10–16, Feb 2012.

[107] S. H. Wrzesinski, Y. Y. Wan, and R. A. Flavell, "Transforming growth factor-beta and the immune response: implications for anticancer therapy," *Clin Cancer Res*, vol. 13, pp. 5262–5270, Sep 2007.

[108] C. E. Campiglio, N. Contessi Negrini, S. Farè, and L. Draghi, "Cross-Linking Strategies for Electrospun Gelatin Scaffolds," *Materials (Basel)*, vol. 12, Aug 2019.

[109] B. C. Cooley, J. Nevado, J. Mellad, D. Yang, C. St Hilaire, A. Negro, F. Fang, G. Chen, H. San, A. D. Walts, R. L. Schwartzbeck, B. Taylor, J. D. Lanzer, A. Wragg, A. Elagha, L. E. Beltran, C. Berry, R. Feil, R. Virmani, E. Ladich, J. C. Kovacic, and M. Boehm, "TGF- signaling mediates endothelial-to-mesenchymal transition (EndMT) during vein graft remodeling," *Sci Transl Med*, vol. 6, p. 227ra34, 03 2014.

[110] M. J. Goumans and P. Ten Dijke, "TGF- Signaling in Control of Cardiovascular Function," *Cold Spring Harb Perspect Biol*, vol. 10, 02 2018.

[111] I. B. Robertson and D. B. Rifkin, "Regulation of the Bioavailability of TGF- and TGF--Related Proteins," *Cold Spring Harb Perspect Biol*, vol. 8, 06 2016.

[112] A. P. Hinck, S. J. Archer, and S. W. Qian, "Transforming Growth Factor 1: Three-Dimensional Structure in Solution and Comparison with the X-ray Structure of Transforming Growth Factor 2," *Biochemistry*, vol. 35, pp. 8517–8534, Jan 1996.

[113] J. P. Annes, D. B. Rifkin, and J. S. Munger, "The integrin alphaVbeta6 binds and activates latent TGFbeta3," *FEBS Lett*, vol. 511, pp. 65–68, Jan 2002.

[114] I. B. Robertson and D. B. Rifkin, "Unchaining the beast; insights from structural and evolutionary studies on TGF secretion, sequestration, and activation," *Cytokine Growth Factor Rev*, vol. 24, pp. 355–372, Aug 2013.

[115] L. Bell and J. A. Madri, "Effect of platelet factors on migration of cultured bovine aortic endothelial and smooth muscle cells," *Circ Res*, vol. 65, pp. 1057–1065, Oct 1989.

[116] T. Kanzaki, K. Tamura, K. Takahashi, Y. Saito, B. Akikusa, H. Oohashi, N. Kasayuki, M. Ueda, and N. Morisaki, "In vivo effect of TGF- beta 1. Enhanced intimal thickening by administration of TGF- beta 1 in rabbit arteries injured with a balloon catheter," *Arterioscler Thromb Vasc Biol*, vol. 15, pp. 1951–1957, Nov 1995.

[117] M. W. Majesky, V. Lindner, D. R. Twardzik, S. M. Schwartz, and M. A. Reidy, "Production of transforming growth factor beta 1 during repair of arterial injury," *J Clin Invest*, vol. 88, pp. 904–910, Sep 1991.

[118] S. Fujii, W. E. Hopkins, and B. E. Sobel, "Mechanisms contributing to increased synthesis of plasminogen activator inhibitor type 1 in endothelial cells by constituents of platelets and their implications for thrombolysis," *Circulation*, vol. 83, pp. 645–651, Feb 1991.

[119] J. T. Keyes, B. R. Simon, and J. P. Vande Geest, "Location-dependent coronary artery diffusive and convective mass transport properties of a lipophilic drug surrogate measured using nonlinear microscopy," *Pharm. Res.*, vol. 30, pp. 1147–1160, Apr 2013.

[120] J. Panyam and V. Labhasetwar, "Biodegradable nanoparticles for drug and gene delivery to cells and tissue," *Adv. Drug Deliv. Rev.*, vol. 55, pp. 329–347, Feb 2003.

[121] A. Zoumi, X. Lu, G. S. Kassab, and B. J. Tromberg, "Imaging coronary artery microstructure using second-harmonic and two-photon fluorescence microscopy," *Biophys. J.*, vol. 87, pp. 2778–2786, Oct 2004.

[122] D. Mozaffarian, E. J. Benjamin, A. S. Go, and D. K. Arnett, "Heart Disease and Stroke Statistics-2016 Update: A Report From the American Heart Association," *Circulation*, vol. 133, pp. 38–360, Jan 2016.

[123] J. Daemen, P. Wenaweser, K. Tsuchida, L. Abrecht, S. Vaina, C. Morger, N. Kukreja, P. J?ni, G. Sianos, G. Hellige, R. T. van Domburg, O. M. Hess, E. Boersma, B. Meier, S. Windecker, and P. W. Serruys, "Early and late coronary stent thrombosis of sirolimus-eluting and paclitaxel-eluting stents in routine clinical practice: data from a large two-institutional cohort study," *Lancet*, vol. 369, pp. 667–678, Feb 2007.

[124] C. W. Hwang, D. Wu, and E. R. Edelman, "Physiological transport forces govern drug distribution for stent-based delivery," *Circulation*, vol. 104, pp. 600–605, Jul 2001.

[125] A. C. Newby and A. B. Zaltsman, "Molecular mechanisms in intimal hyperplasia," *J. Pathol.*, vol. 190, pp. 300–309, Feb 2000.

[126] G. D. Dangas, B. E. Claessen, A. Caixeta, E. A. Sanidas, G. S. Mintz, and R. Mehran, "In-stent restenosis in the drug-eluting stent era," *J. Am. Coll. Cardiol.*, vol. 56, pp. 1897–1907, Nov 2010.

[127] J. W. Moses, M. B. Leon, J. J. Popma, P. J. Fitzgerald, D. R. Holmes, C. O'Shaughnessy, R. P. Caputo, D. J. Kereiakes, D. O. Williams, P. S. Teirstein, J. L. Jaeger, and R. E. Kuntz, "Sirolimus-eluting stents versus standard stents in patients with stenosis in a native coronary artery," *N. Engl. J. Med.*, vol. 349, pp. 1315–1323, Oct 2003.

[128] G. W. Stone, S. G. Ellis, L. Cannon, J. T. Mann, J. D. Greenberg, D. Spriggs, C. D. O'Shaughnessy, S. DeMaio, P. Hall, J. J. Popma, J. Koglin, and M. E. Russell, "Comparison of a polymer-based paclitaxel-eluting stent with a bare metal stent in patients with complex coronary artery disease: a randomized controlled trial," *JAMA*, vol. 294, pp. 1215–1223, Sep 2005.

[129] M. C. Morice, A. Colombo, B. Meier, P. Serruys, C. Tamburino, G. Guagliumi, E. Sousa, and H. P. Stoll, "Sirolimus- vs paclitaxel-eluting stents in de novo coronary artery lesions: the REALITY trial: a randomized controlled trial," *JAMA*, vol. 295, pp. 895–904, Feb 2006.

[130] J. T. Keyes, B. R. Simon, and J. P. Vande Geest, "A finite element study on variations in mass transport in stented porcine coronary arteries based on location in the coronary arterial tree," *J Biomech Eng*, vol. 135, pp. 61008–61011, Jun 2013.

[131] J. T. Keyes, D. R. Lockwood, B. R. Simon, and J. P. Vande Geest, "Deformationally dependent fluid transport properties of porcine coronary arteries based on location in the coronary vasculature," *J Mech Behav Biomed Mater*, vol. 17, pp. 296–306, Jan 2013.

[132] A. M. Malek, S. L. Alper, and S. Izumo, "Hemodynamic shear stress and its role in atherosclerosis," *JAMA*, vol. 282, pp. 2035–2042, Dec 1999.

[133] J. D. Talley, W. S. Weintraub, G. S. Roubin, J. S. Douglas, H. V. Anderson, E. L. Jones, D. C. Morris, H. A. Liberman, J. M. Craver, and R. A. Guyton, "Failed elective percutaneous transluminal coronary angioplasty requiring coronary artery bypass surgery. In-hospital and late clinical outcome at 5 years," *Circulation*, vol. 82, pp. 1203–1213, Oct 1990.

[134] G. S. Roubin, S. B. King, and J. S. Douglas, "Restenosis after percutaneous transluminal coronary angioplasty: the Emory University Hospital experience," *Am. J. Cardiol.*, vol. 60, pp. 39B–43B, Jul 1987.

[135] S. L. Chen, J. J. Zhang, F. Ye, Z. Z. Liu, Z. S. Zhu, S. Lin, N. L. Tian, W. Y. Fang, Y. D. Chen, X. W. Sun, M. Wei, S. J. Shan, J. Kan, J. Qian, S. Yang, Z. B. Yuan, T. W. Kwan, and D. Y. Hu, "Crush stenting with drug-eluting stents: relevance of coronary bifurcation lesion location on angiographic and clinical outcomes," *Clin Cardiol*, vol. 33, pp. E32–39, Dec 2010.

[136] S. Elezi, A. Dibra, J. Mehilli, J. Pache, R. Wessely, A. Sch?mig, and A. Kastrati, "Vessel size and outcome after coronary drug-eluting stent placement: results from a large cohort of patients treated with sirolimus- or paclitaxel-eluting stents," *J. Am. Coll. Cardiol.*, vol. 48, pp. 1304–1309, Oct 2006.

[137] L. Montilla, R. Olafsson, and R. Witte, "Real-time pulse echo and photoacoustic imaging using an ultrasound array and in-line reflective illumination," vol. 7564, 2010.

[138] L. G. Montilla, R. Olafsson, D. R. Bauer, and R. S. Witte, "Real-time photoacoustic and ultrasound imaging: a simple solution for clinical ultrasound systems with linear arrays," *Phys Med Biol*, vol. 58, pp. 1–12, Jan 2013.

[139] L. V. Wang and H.-I. Wu, *Biomedical optics: principles and imaging*. Wiley, 2007.

[140] J. R. Rajian, P. L. Carson, and X. Wang, "Quantitative photoacoustic measurement of tissue optical absorption spectrum aided by an optical contrast agent," *Opt Express*, vol. 17, pp. 4879–4889, Mar 2009.

[141] F. Streit, U. Christians, H. M. Schiebel, K. L. Napoli, L. Ernst, A. Linck, B. D. Kahan, and K. F. Sewing, "Sensitive and specific quantification of sirolimus (rapamycin) and its metabolites in blood of kidney graft recipients by HPLC/electrospray-mass spectrometry," *Clin. Chem.*, vol. 42, pp. 1417–1425, Sep 1996.

[142] T. A. Willey, E. J. Bekos, R. C. Gaver, G. F. Duncan, L. K. Tay, J. H. Beijnen, and R. H. Farmen, "High-performance liquid chromatographic procedure for the quantitative determination of paclitaxel (Taxol) in human plasma," *J. Chromatogr.*, vol. 621, pp. 231–238, Nov 1993.

[143] D. S. Miller, G. Fricker, and J. Drewe, "p-Glycoprotein-mediated transport of a fluorescent rapamycin derivative in renal proximal tubule," *J. Pharmacol. Exp. Ther.*, vol. 282, pp. 440–444, Jul 1997.

[144] V. Daeichin, M. Wu, N. De Jong, A. F. van der Steen, and G. van Soest, "Frequency Analysis of the Photoacoustic Signal Generated by Coronary Atherosclerotic Plaque," *Ultrasound Med Biol*, vol. 42, pp. 2017–2025, 08 2016.

[145] J. L. Su, B. Wang, and S. Y. Emelianov, "Photoacoustic imaging of coronary artery stents," *Opt Express*, vol. 17, pp. 19894–19901, Oct 2009.

[146] A. B. Karpiouk, B. Wang, J. Amirian, R. W. Smalling, and S. Y. Emelianov, "Feasibility of in vivo intravascular photoacoustic imaging using integrated ultrasound and photoacoustic imaging catheter," *J Biomed Opt*, vol. 17, pp. 96008–96001, Sep 2012.

[147] X. Bai, X. Gong, W. Hau, R. Lin, J. Zheng, C. Liu, C. Zeng, X. Zou, H. Zheng, and L. Song, "Intravascular optical-resolution photoacoustic tomography with a 1.1 mm diameter catheter," *PLoS ONE*, vol. 9, no. 3, p. e92463, 2014.

[148] Y. Li, X. Gong, C. Liu, R. Lin, W. Hau, X. Bai, and L. Song, "High-speed intravascular spectroscopic photoacoustic imaging at 1000 A-lines per second with a 0.9-mm diameter catheter," *J Biomed Opt*, vol. 20, p. 065006, Jun 2015.

[149] B. Wang, A. Karpiouk, D. Yeager, J. Amirian, S. Litovsky, R. Smalling, and S. Emelianov, "In vivo intravascular ultrasound-guided photoacoustic imaging of lipid

in plaques using an animal model of atherosclerosis," *Ultrasound Med Biol*, vol. 38, pp. 2098–2103, Dec 2012.

[150] X. Li, W. Wei, Q. Zhou, K. K. Shung, and Z. Chen, "Intravascular photoacoustic imaging at 35 and 80 MHz," *J Biomed Opt*, vol. 17, p. 106005, Oct 2012.

[151] Y. Cao, J. Hui, A. Kole, P. Wang, Q. Yu, W. Chen, M. Sturek, and J. X. Cheng, "High-sensitivity intravascular photoacoustic imaging of lipid-laden plaque with a collinear catheter design," *Sci Rep*, vol. 6, p. 25236, 04 2016.

[152] K. Jansen, M. Wu, A. F. van der Steen, and G. van Soest, "Photoacoustic imaging of human coronary atherosclerosis in two spectral bands," *Photoacoustics*, vol. 2, pp. 12–20, Mar 2014.